Characterization of the wake of large depth-ratio cylinders at low Reynolds numbers

BY

Arash Zargar

A THESIS SUBMITTED IN PARTIAL FULFILMENT OF THE REQUIREMENTS FOR THE DEGREE OF

MASTER OF SCIENCE

DEPARTMENT OF **MECHANICAL ENGINEERING**

UNIVERSITY OF ALBERTA

ABSTRACT

This dissertation characterizes the wake dynamics of long depth-ratio wall-mounted rectangular cylinders at a range of Reynolds numbers between $250-1000$ at different incidence (yaw) angles, $0°-45°$ with respect to the free stream flow. The effect of large depth-ratio on flow characteristics and vortex evolution is first explored for steady and unsteady wakes of wall-mounted cylinders at zero incident angle using Large Eddy Simulations (LES). Following this fundamental wake characterization at zero incident-angle, the unsteady wake evolution by large incident (yaw) angles are investigated at similar Reynolds numbers.

The fundamental characterization of the wake was completed through a detailed comparison of the wake features for square (small-depth ratio of 0.83) and long-rectangular (large-depth ratio of 4.15) wall-mounted cylinders at two Reynolds numbers. The wake models for the latter were developed and compared with the existing models for square cylinders. LES results showed that the simulated wake at Reynolds number of 250 is steady for both cylinders, whereas there was transition to an unsteady wake at Reynolds number of 1000. The latter wake was dominated by hairpin-like structures formed on top of the cylinder and vortex loops formed by the unsteady transition of horseshoe vortices. The long lasting effect in the wake, however, belonged to an arc-type structure in the near wake region, the frequency signature of which remained apparent farther downstream. A new skeleton model is developed and introduced for the wake of a long depth-ratio cylinder that identifies three distinct flow features. In development of this model, the Strouhal number of $St_{hp} = 0.38$ and 0.64 were attributed to the hairpin-like vortices on the cylinder upper and side faces, respectively. The dominant frequency corresponding to the Strouhal number of 0.26 was due to the horseshoe vortex loops. The peak frequency corresponding to $St_H = 0.175$ was ascribed by the arc-type structure in the wake, which persisted farther downstream the wake.

Study of the wake was then extended to characterize the unsteady wake of the large depth-ratio wall-mounted rectangular cylinder at large incident (yaw) angles even at Reynolds number of 250. LES simulations are carried out for 10 different incidence angles between $i = 0°$ and $i = 45°$ at 5° increments to understand the implications of incident angle on altering the wake topology.

Numerical results showed that increasing the incidence angle changes the wake from symmetric to asymmetric, which then translates to unsteady features. For the incidence angles of $i \leq 35°$, the separated flow from the rear and leeward leading edges reattach to the cylinder at distinct points. The onset of wake unsteadiness occurs at $35° < i \leq 40°$. The weakly unsteady flow characteristics are captured in the wake of the cylinder at $i = 40°$ with small amplitude fluctuations identified in the velocity and pressure fields. Increasing the incidence angle to $45°$ coincided with a stronger wake unsteadiness that incorporated low and high frequency features. The main difference in the flow due to changing incidence angle is the formation of helical structures that dominate the wake region at $i = 40°$ and $45°$. Three distinct frequencies were observed in the wake of the cylinder at $i = 45°$. The Strouhal number of $St = 0.13$ was attributed to the regular vortex shedding process in the wake region. The low-frequency fluctuations corresponding to $St_H = 0.0146$ were due to the alterations to the shape and size of unsteadily evolving helical structures that spin out of the vortex tubes. There also existed a high-frequency fluctuation at $St = 0.46$, which was connected to the onset of unsteadiness, or the unsteady wake transition mechanism. It was further determined that the high-frequency and low-frequency fluctuations were connected in such a manner that the former initiated the onset of unsteady wake, through the formation of helical structures, while the latter suppressed the unsteady wake features. Moreover, the low-frequency suppression mechanism appeared to start in the wake and propagate to the shear layers on the cylinder.

PREFACE

The results from Chapter 3 are currently under review for publication in the Journal of Fluid Mechanics with the following citation:

Zargar, A., Tarokh, A., Hemmati, A. (2020). The wake of a wall-mounted rectangular cylinder with a large-depth-ratio at low Reynolds numbers. *Journal of Fluid Mechanics*, under-review.

The results from Chapter 4 are under-review for publication in the Journal of Physical Review Fluids with the following citation:

Zargar, A., Gungor, A., Tarokh, A., Hemmati, A. (2020). Low frequency dynamics in the wake of a long wall-mounted rectangular cylinder at high incident angles. *Physical Review Fluids*, under-review.

All the simulations, data analysis and interpretation of results in this thesis were performed by Arash Zargar under the supervision of Dr. Arman Hemmati. The simulations are completed using the resources of Compute Canada. The co-authors in aforementioned papers provided assistance in the initial planning of the simulations, support in discussions and editorial input by reviewing the manuscripts prior to submission. The results provided and discussion included in this thesis are based on the work of Arash Zargar, who led the authorship of both manuscripts.

ACKNOWLEDGEMENTS

To my Parents, for their love, support, and encouragement

Contents

List of Tables

List of Figures

LIST OF ABBREVIATIONS, SYMBOLS, AND

NOMENCLATURE

Latin Symbols

h	cylinder height
D	diameter
L	characteristic length scale
w_p	cylinder projected width
A	area
Re	Reynolds number based on height
Re_{w_p}	Reynolds number based on projected length
Re_{cr}	critical Reynolds number
St	Strouhal number
f	frequency
t	time
t^*	convective time
u	Cartesian $x-$wise velocity component
v	Cartesian $y-$wise velocity component
w	Cartesian $z-$wise velocity component
U_0	free-stream velocity
U	velocity scale
AR	aspect ratio
DR	depth ratio
C_p	coefficient of pressure
C_l	coefficient of lift
C_d	coefficient of drag
F_i	force in i direction

p	pressure
S_{ij}	strain tensor
L_{ij}	Leonard stress

Greek Symbols

δ	boundary layer thickness
η	Kolmogorov length scale
ρ	density
μ	dynamic viscosity
ν	kinematic viscosity
σ_{ij}	stress tensor
ΔV_{ijk}	local volume grid size
Δ	spatial filter width
$\hat{\tau}_{ij}^{SGS}$	subgrid stress(SGS) tensor

Other Symbols

$\overline{\square}$	mean (time-averaged)
$\hat{\square}$	filtered (volume-averaged)
Δ	difference
$\approx$	approximately
$O[\ ]$	order of

Abbreviations

2D	Two Dimensional
3D	Three Dimensional
CFD	Computational Fluid Dynamics
DNS	Direct Numerical Simulation
LES	Large Eddy Simulation

DES   Detached Eddy Simulation

RANS   Reynolds Averaged Navier Stokes

CFL   Courant-Friedrichs-Levy Number

DRA   Drag Reducing Agent

SIMPLE   Semi-Implicit Method for Pressure Linked Equations

PISO   Pressure Implicit with Splitting of Operators

GS   Grid scale

SGS   Subgrid scale

Chapter 1

INTRODUCTION

This dissertation focuses on investigating the flow around a large depth-ratio rectangular cylinder at a range of incident angles and Reynolds numbers. Since the pioneering work of Taneda (1952), there has been numerous studies attempted to characterize (Behera and Saha, 2019), scale (Sarode et al., 1981) and model (da Silva et al., 2020) coherent structures in the wake of wall-mounted rectangular and square cylinders. The implications of critical parameters, such as boundary layer thickness (Hosseini et al., 2013; El Hassan et al., 2015), Reynolds number (Zhang et al., 2017; Hwang and Yang, 2004), incident (yaw) angles (Castro and Robins, 1977; Sakamoto, 1985; Becker et al., 2002), aspect ratio (Saha, 2013; Rostamy et al., 2013; Sumner et al., 2017) and crossectional shape (Uffinger et al., 2013; Kindree et al., 2018) of a short depth-ratio cylinder constitutes a broad range of topics extensively examined in literature. However, the effect of large depth-ratio and how such geometrical variations alter the wake topology, and its corresponding dependence on the aforementioned critical parameters, remains unexplored. Here, depth-ratio and aspect-ratio are defined as

$$DR = l/h \qquad \text{and} \qquad AR = h/w, \tag{1.1}$$

where DR is the depth-ration, AR is the aspect ration, l is the cylinder streamwise length, w is the cylinder width, and h is the cylinder height. Schematics of a short and long cylinder are shown in Figure 1.1.
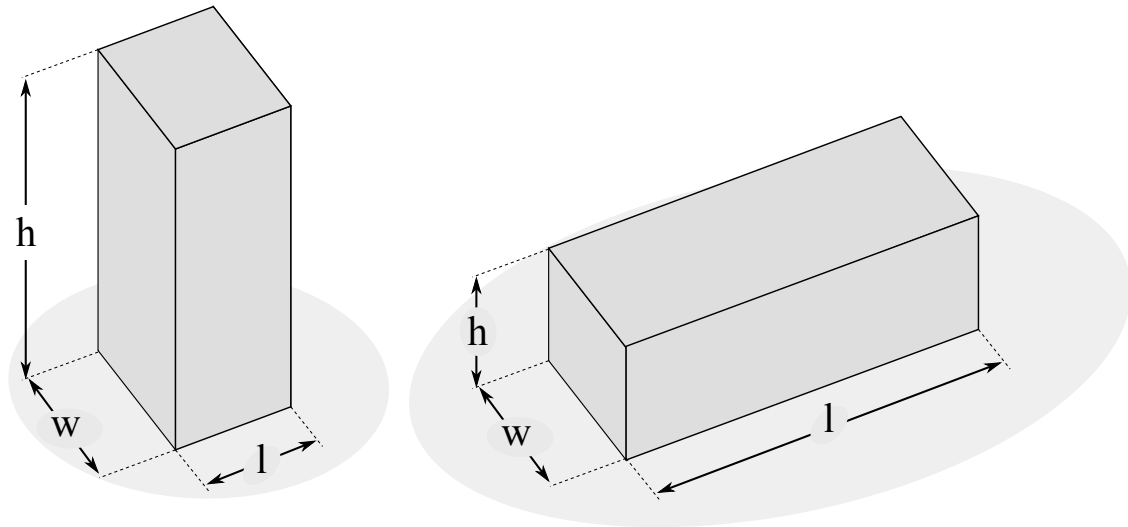
Figure 1.1: Schematics of small depth-ratio (left) and large depth-ratio (right) cylinders.

This study further extends to the effect of incident (yaw) angle on coherent structures and their interactions in the wake, which is expected to differ from small depth-ratio cylinders due to the severity of wake asymmetry.

1.1 Overview

The wake of bluff bodies is dominated by large- and small-scale structures that depend on the shape of the body, its orientation, and the flow and fluid situation. Contrary to the aerodynamic bodies at low angles of attack, bluff bodies are known to have an extended flow region with velocity deficit behind them, referred to as the *wake*. The aerodynamic drag and yaw moment acting on bluff bodies are mostly dominated by pressure differential forces. The pressure of the stagnation front face region is mostly affected by freestream characteristics, and thus it is difficult to manipulate, for example by changing the geometry. However, pressure in the wake region, and thus surface pressure variations on the rear face of the body, is directly induced and influenced by vortical structures formed in the wake. Thus, pressure variations in this region can be altered by manipulating the wake flow structures. Furthermore, wake structure alteration can change the heat

and mass transfer and mixing processes in the wake region, which are highly critical in industrial applications. Hence, the identification, characterization, and modification of the wake structures behind a wall-mounted rectangular cylinder have been the focus of researchers for decades.

Circular and rectangular cylinders, flat plates at high angles of attack, and generic shapes, such as Ahmed bodies, constitute a class of bluff bodies commonly examined in the study of unsteady wakes. The most critical and common of flow characteristics associated with bluff body wakes is the formation and separation of boundary layers on the surfaces of the body, leading to the formation of free shear layers and the separated wake region (Zdravkovich, 1997). Wake of a wall-mounted cylinder is characterized by the interactions of horseshoe, tip, base, Kàrmàn-type, and arc-type vortices. These structures can be affected by boundary layer flow on the ground, upwash flow near the junction, downwash flow close to the cylinder free end, and separated shear-layer from the side faces. Furthermore, depending on the state of the flow, structures may be laminar, transitional or turbulent. The transition may have different origins such as wake, free shear layers, and boundary layer. Therefore, the state of each structure can vary by different parameters such as Reynolds number, surface roughness, freestream turbulence, boundary layer, blockage ratio, aspect ratio, and free-end effects (Zdravkovich, 1997). Hence, wall-mounted cylinders have highly complex wake structures enriched with unique characteristics.

Several studies on wall-mounted cylinders have established that changing the Reynolds number, defined as $Re = U_0 c/\nu$, does not alter the main features of the wake topology (Saha et al., 2000; Perry et al., 1982; Krajnovic and Davidson, 2005a). To this effect, Saha et al. (2000) numerically showed that results of his simulation at $Re = 100$ has a negligible change on the wake of a 2D cylinder in comparison with experimental results of Lyn et al. (1995) at $Re = 21400$ and Cantwell and Coles (1983) at $Re = 140000$. Furthermore, Perry et al. (1982) and Krajnovic and Davidson (2005a) made similar observations for the case of 2D circular cylinders and an Ahmed body, respectively. Thus, it can be concluded that investigating the flow around sharp-edge bluff bodies at low Reynolds numbers, e.g., $Re = 40 - 250$ for Rastan et al. (2017), can enhance our qualitative knowledge on characteristics of the wake features at higher Reynolds number (e.g., $Re > 1000$) as

well. Hence, several previous studies on the wall-mounted cylinders at low Reynolds numbers have led to a better qualitative understanding of the flow around buildings, chimneys, and tube banks in heat exchangers (Saha, 2013; Rastan et al., 2017).

Coherent structures can be defined as temporary and recurring structures that carry the highest value of energy in the turbulent energy spectrum. The transient nature of these structures implies that they reform and transform into smaller turbulence structures through the *cascade process*. Finally due to viscous effects, the small scale structures diffuse with their energy dissipated as heat. The critical role of coherent structures in characterizing the wake, therefore, has motivated many studies on their visualization, leading to their spatial scaling to identify their dynamic significance in the wake (Kline, 1967; Hussain, 1986).

1.2 Tools

Numerically simulating the details of such complicated wakes is a challenging problem, and special considerations should be given to accurate modeling of the flow. Krajnovic and Davidson (2005a) utilized Large Eddy Simulations (LES), a sub-grid scale model based on eddy viscosity approximation (Durbin and Reif, 2011), to simulate the flowfield around a simplified car-like bluff body. They discussed that a structured hexahedral mesh can provide more accurate results than other mesh types, such as tetrahedral grids. This was also further supported by other researchers in the study of sharp-edge bluff body wakes using LES and Direct Numerical Simulations (DNS), e.g., Hemmati et al. (2018). To this end, ANSYS ICEM-CFD, which is one of the most powerful mesh generating tools, is employed in preparing the structured grids in this dissertation. The simulations are computed using Open-source Field Operation And Manipulation (OpenFOAM) 4.1 as the main platform and LES Dynamic Smagorinsky model. OpenFOAM is an open-source finite volume-based software package that was initially created by Henry Weller as "FOAM" at Imperial College London in 1989. It was later that it was redeveloped and released as "OpenFOAM" to the broader community in 2004 by Henry Weller, Chris Greenshields, and Mattijs Janssens (Open-

FOAM, 2004). The solvers and libraries are designed using C++ programming language to solve computational fluid dynamics (CFD) problems. The final version of OpenFOAM is designed to provide an open-source and wide range of libraries, pre- and post-processing tools, and solvers. Details on the formulations of LES Dynamic Smagorinsky model are provided in Chapter 3. The simulation results are then processed and manipulated using a combination of Paraview, Tecplot and MATLAB.

1.3   Motivation

Wall-mounted rectangular and circular cylinders have extensive industrial applications at low Reynolds number, ranging from the fast response measurement systems (Dousset and Pothérat, 2010) to micro heat-exchangers (Rastan et al., 2017) and bio-medical devices, particularly passive micro mixers (Zhang et al., 2019). Due to this broad industrial application, identifying the flow structures, optimizing the heat transfer, and modifying the flow around cylinders can be classified as one of the most compelling problems in fluid dynamics. To this end, the wake of long (large depth-ratio) cylinders have not been extensively studied in literature.

The knowledge gained from studying the wake of large depth-ratio cylinders enhances our fundamental understanding of vortex interactions and wake dynamics, which goes beyond the apparent industrial application of these bodies. Moreover, this knowledge will be essential in optimizing the design of industrial equipment and technologies that involve flow interactions with sharp-edge bodies. Thus, this thesis aims at addressing the aforementioned knowledge gaps using numerical simulations.

1.4   Research Objectives

The primary research objective of this thesis is to identify, characterize and model the dominant vortical structures in the wake of a large depth-ratio wall-mounted rectangular cylinder at low Reynolds numbers and large incident (yaw) angles. Particularly, the first objective involves un-

derstanding the wake topology and developing a wake model at zero incident-angle. The second objective is characterizing the wake dynamics due to increasing incident angles at similar Reynolds numbers.

The first objective focuses on understanding the effect of large depth-ratio using a detailed numerical analysis of the flow around a wall-mounted rectangular cylinder with depth-ratio of $DR = l/h = 4.15$. The newly developed model is then compared to that of a small depth-ratio rectangular cylinder ($DR = 0.83$) at $Re = 250$ and 1000. This provides insight into how the large depth-ratio of a wall-mounted cylinder alters the wake topology and evolution.

The second objective of the present research focuses on characterizing the effect of incident angle on the wake topology of a wall-mounted rectangular cylinder. The flow around the large depth-ratio ($DR = 4.15$) rectangular cylinder is examined numerically at 10 different incident (yaw) angles from 0° to 45° with 5° increment at $Re = 250$. The special case of a normal cylinder (90° incident angle) is also investigated for comparison purposes only.

1.5   Novelty

The present study focuses on addressing a knowledge gap on the effect of large depth-ratio on the wake topology of rectangular cylinders at low Reynolds number. Despite several studies on wall-mounted cylinders over the past century, the focus has always remained on small depth-ratio cylinders with different boundary layer thicknesses (Hosseini et al., 2013; El Hassan et al., 2015), Reynolds numbers (Zhang et al., 2017; Hwang and Yang, 2004), incident (yaw) angles (Castro and Robins, 1977; Sakamoto, 1985; Becker et al., 2002), aspect ratios (Saha, 2013; Rostamy et al., 2013; Sumner et al., 2017) and crossectional shapes (Uffinger et al., 2013; Kindree et al., 2018). The present study is the first of its kind to characterize and model the coherent structures in the wake of a long (large depth-ratio) wall-mounted cylinder. The wake structures and fluid characteristics explored here are unique to the wake of large depth-ratio cylinders due to the folding of separated flow from the cylinder leading edges on the side faces, which then interact with the

growing horseshoe structures. Another unique novelty of this research relates to identifying the formation and dynamics of helical structures in the wake of a large depth-ratio cylinder at large incident angles. Furthermore, this study identifies high- and low-frequency features of the wake related to the wake vortex shedding process and periodically formation and suppression of wake flow coherent structures, respectively. A comprehensive unsteady wake model is introduced for both zero and non-zero incident angles, which is the first of its kind for this class of bluff bodies. Based on the results of this research, it has been shown that the commonly used height or width of a rectangular cylinder cannot be considered as a proper characteristic length scale at high incidence angles. Therefore, the cylinder projected width is proposed as the characteristic length scale. These constitutes novel findings of this thesis that advance the frontiers of flow dynamics in the wake of sharp-edge bluff-bodies.

1.6   Structure of the thesis

This thesis begins with a review of fundamental topics in wake dynamics and flow modeling in Chapter 2. Particularly, this section includes a review of literature on coherent wake structures, computational fluid dynamics simulations, and turbulence modeling. Further detail on the state of literature on the wake of rectangular cylinders are provided in initial sections of Chapters 3 and 4. More specifically, these sections provide a comprehensive literature review on different parameters altering the wake of wall-mounted cylinders, such as Reynolds number, boundary layer thickness, incident angle, aspect ratio, and cross-sectional shape of the cylinder.

The research methodology in this thesis is presented individually per chapter. Particularly in Chapter 3, details on the numerical setup, including quality of the grid, effect of domain size, and validity of numerical solvers are presented for the zero-incident angle cylinder. This chapter also provides a detailed description and model for the wake of large depth-ratio wall-mounted rectangular cylinders at Reynolds numbers of $Re = 250$ and 1000. This is followed by establishing the implications of the incident angle on the wake dynamics in Chapter 4 along with a new wake

model. Finally, the conclusions of the present research and potential topics of research for future studies are introduced in Chapter 5.

Chapter 2

BACKGROUND

In this chapter, a brief overview of fundamental and key topics in fluid dynamics, wake dynamics, computational fluid dynamics simulations, and turbulence modeling is presented to set the state of literature for this thesis.

By definition, a "simple" fluid can be defined as a material that the positions of its elements change considerably due to application of a suitable force of any magnitude, according to Batchelor (2000). The proposed definition for "Dynamics" by Collins dictionary is "the scientific study of motion, energy, and forces." Therefore, Fluid Dynamics can be defined by the study of motion, energy, and forces acted on or exerted by the so-called fluid material. Aerodynamics is a subdiscipline of fluid dynamics that focuses on the motion of air and determines the forces and moments exerted by it on a submerged or semi-submerged body in the air. In the field of continuum mechanics, stress(σ) can be defined as internal forces that neighboring particles exert on each other, divided by the area on which these forces act,

$$\sigma_{ij} = F_i A_j^{-1}, \tag{2.1}$$

where σ_{ij}, F_i, and A_j represent the stress tensor, force vector, and planar area, respectively. Viscosity, therefore, is a fluid property that can be defined as the tangential stress divided by the gradient

of velocity (Batchelor, 2000):

$$\mu = \sigma_{ij} \nabla_i^{-1} u_j^{-1}. \tag{2.2}$$

To this effect, the compressibility of a fluid is defined as its relative volume change due to the change in pressure (Babu, 2015). All fluids are compressible to some extent. However, the incompressibility assumption may be valid for some fluids, e.g., water, under the natural atmospheric pressure conditions.

Aerodynamics experts proposed different types of classifications for the exact definition of a fluid state. The most practical classifications are done based on viscosity, compressibility, steadiness, and randomness of fluid flow. To this end, *Reynolds number* is defined as the primary non-dimensional controlling parameter of the fluid state (White and Corfield, 1991):

$$Re = \rho u c / \mu = u c / \nu, \tag{2.3}$$

where u is the velocity scale, c is the characteristic length scale, ρ is the fluid density, and μ and ν are the fluid dynamic and kinematic viscosity, respectively. In fact, Reynolds number identifies the ratio of inertial to viscous forces, which translates to which of the two fundamental flow characteristics dominate in the wake.

Based on the definitions and classifications discussed thus far, viscosity is one of the important properties in fluids. In fact, fluid flow is categorized based on the important of viscosity: Inviscid versus viscous fluids. For the former, tangential stress components are zero, and the stress tensor has the same components as an arbitrary fluid at rest (Batchelor, 2000). Contrarily, a viscous fluid is a fluid that exhibits internal friction due to velocity gradients between neighboring molecules (Batchelor, 2000). Density is another important fluid property that characterizes the fluid flow. An incompressible flow is defined as a flow in which the density of fluid remains constant. For compressible flow, however, the density is variable. It is established that for air flowing with a velocity less than 30% of the speed of sound, the assumption of incompressible flow can be applied (Anderson, 1991).

The transient nature of the flow is also important, specially in terms of wake dynamics. If flow properties vary over time, the flow is referred to as unsteady. However, if the properties are independent of time and change only with spatial variations, the flow is referred to as a steady flow (Kuethe et al., 1998). For unsteady flows, it is common to project the main parameters that characterize the flow, e.g., force coefficients, velocity and pressure, from time domain to a frequency domain to identify the periodicity, and thus, coherence of various flow features. Peak frequency or *dominant frequency* is defined as the frequency that carries the largest energy content in the wake, within the frequency domain (Telgarsky, 2013). The non-dimensional number that characterizes the importance of such frequencies in the flow is the Stroulaul number (White and Corfield, 1991)

$$St = fc/u, \tag{2.4}$$

where f is the dominant frequency, c is the characteristic length scale, and u is the velocity scale.

One of the most commonly studied, and yet not fully understood, unsteady flow behavior is turbulence. By definition, a laminar flow is a smooth and regular flow (Davidson, 2004), such as very slow-moving or very viscous fluid flow. However, there is not a complete and comprehensive definition for turbulent flows. Indeed, turbulence can best be recognized by its characteristics, which according to Davidson (2020) includes the following:

Irregularity: turbulent flows are irregular in nature, which is defined by their random and chaotic characteristics. However, they are still governed by the Navier-Stokes equations.

Diffusivity: the momentum transfer between different flow layers increases in turbulent flow, meaning that the diffusivity of turbulent flow is higher than laminar flow.

Large Reynolds numbers: increasing the Reynolds number intensifies the level of flow fluctuations and perturbations in laminar flows, which trigger transition to turbulent flow.

Three-Dimensionality: turbulent flow is by virtue three dimensional based on laws governing the vortex dynamics. Thus, there exist different flow scales (or eddies) in a turbulent flow.

Dissipativity: turbulence kinetic energy transfers from large scales to smaller scales by a process

referred to as the '"Energy Cascade". The kinetic energy associated with the smallest scales are dissipated as heat due to the effect of viscous forces. This implies that a turbulent flow is dissipative.

Continuum: the smallest scales of a turbulent flow are significantly larger than the fluid molecules. Therefore, the condition for continuity remains important for turbulent flow. Thus, turbulence is a flow property and not a fluid property.

The equations of motion that govern fluid behavior are the continuity, momentum, and energy equations. These can be modified based on the state of the flow. In the present study, the flow is viscous, incompressible, unsteady, and turbulent, based on which the governing equations are (Durbin and Reif, 2011):

$$\frac{\partial u_i}{\partial x_i} = 0, \tag{2.5}$$

$$\rho \frac{\partial u_i}{\partial t} + \rho \frac{\partial u_i u_j}{\partial x_j} = -\frac{\partial p}{\partial x_i} + \mu \frac{\partial^2 u_j}{\partial x_i x_j} + \rho f_i, \tag{2.6}$$

Here, u_i is the velocity and p is pressure.

To reduce the number and complexity of variables, usually integral and differential flow parameteres are normalized using flow characteristic length and velocity. In the present research, the integral parameters of lift (L) and drag (D) forces are normalized using bulk velocity (U_0) and cylinder's height (h).

$$C_l = \frac{L}{0.5\rho U_0^2 h} \tag{2.7}$$

$$C_d = \frac{D}{0.5\rho U_0^2 h} \tag{2.8}$$
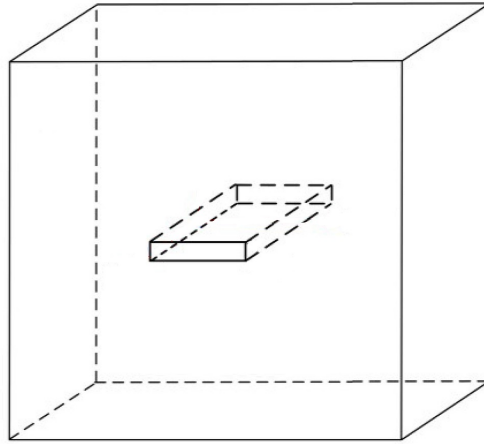
Figure 2.1: Schematics of 2D cylinders.

2.1 Wakes

The flow around bluff bodies constitute a classic and fundamental problem in fluid mechanics, which has encapsulated the focus of researchers for more than a century. By definition, the re-curring flow system formed behind a bluff body, such as a flat plate, sphere, cylinder and disk, is referred to as *the wake*. The organization of the wake is dictated by the transient nature of the vortex formation and interactions, hint the distinction between steady, quasi-steady and unsteady wakes, and the nature and scaling of vortex structures that give rise to laminar versus turbulent wakes. Therefore, identifying, visualizing, and characterizing these structures are the primary objective of many research studies. The subject of the present research is the study of flow around a wall-mounted large depth-ratio rectangular cylinder, and thus the characteristics and features of the wake formed behind it.

2.1.1 Wake of a 2D rectangular cylinder

As shown in Figure 2.1, a 2D cylinder is an object with infinite extent in spanwise direc-tion.Reynolds number, defined for cylinders based on their diameter, height or width, plays a dominant role in the formation and organization of the wake. The characteristic length scale for cylinders depend on their shape and orientation in the flow. Nakamura (1993) and Sohankar (2006)

provided a good overview of the turbulent length scales and the effect of Reynolds number on the wake of cylinders. One of the early works related to the effect of Reynolds number on the flow patterns around a 2D rectangular cylinder was that of Okajima (1982). Using flow visualization techniques, the velocity field at different locations were obtained, which provided more details on the Strouhal number related to fluctuations in the wake. Their results showed that there is a critical Reynolds number for the wake of rectangular cylinders of aspect ratio 2 and 3, beyond which the wake structures abruptly change. These variations attributed to the reattachment of the separated flow from the leading-edge on either upper or lower surfaces below the critical Reynolds number.

Yu et al. (2012) investigated the effect of aspect ratio on the flow around a 2D rectangular cylinder and determined that Large Eddy Simulations (LES) accurately predict different flow field characteristics, including reattachment points, integral quantities such as aerodynamics forces (lift and drag) and Strouhal numbers, and main features of the wake topology. Later on, Arslan et al. (2013) estimated the coefficients of force and moment acting on a semi-submerged rectangular prism to show that the characteristics of the flow around a rectangular cylinder are strongly related to the submergence ratio. Here, it is defined as the fraction of the submerged portion of the cylinder to its height. Moreover, Bruno et al. (2012), Bruno et al. (2010), and Bruno et al. (2014) completed a series of studies to benchmark the flow characteristics for the wake of a two-dimensional prism with a chord to depth ratio equal to 5. These studies established that there is a good agreement between experimental measurements and numerical calculations for base pressure, aerodynamic drag and Strouhal numbers. However, experimental and numerical calculations disagreed greatly in cases with respect to the mean flow features on the cylinder sides, lift force, and the pressure field. These were attributed to the sensitivity of these parameters to simulations setup and turbulence modeling.

More recently, Cimarelli et al. (2018) performed a detailed Direct Numerical Simulation (DNS) of the flow around a two-dimensional rectangular prism at $Re = 3000$. They provided details on the wake and classified the vortices around the rectangular cylinder into three different types, which are highlighted in Figure 2.2. Cimarelli et al. (2018) also identified two distinct Strouhal
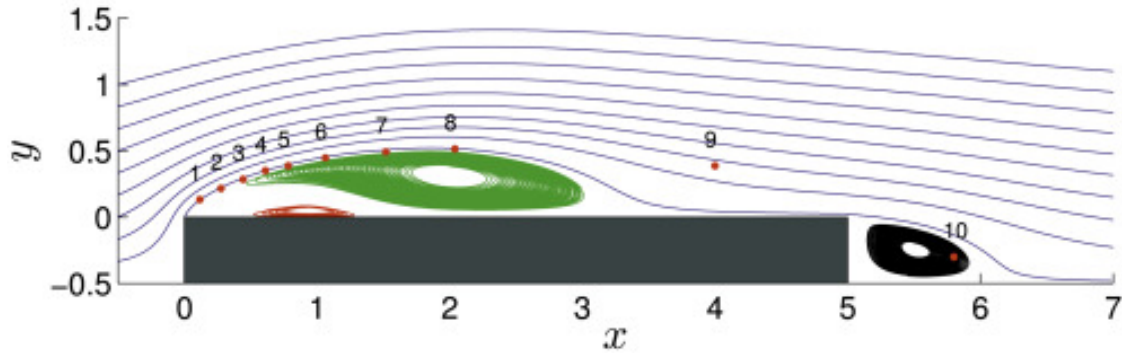
Figure 2.2: Proposed classification of different 2D rectangular cylinder's flow regions by Cimarelli et al. (2018) (Reprinted with permission from Cimarelli et al. (2018), Copyright 2018, Elsevier)

numbers that were dominant in the wake. The higher Strouhal number by order of magnitude, that is $St = O(10^0)$, was associated with the regular vortex shedding at the leading edge of the body. The lower order $St = O(10^{-1})$ was observed in the wake region and it was attributed to the alternating enlargement and shrinkage of the recirculation region on the cylinder top and bottom surfaces. At higher Reynolds numbers of $7.8 \times 10^3 - 1.9 \times 10^4$, Guissart et al. (2019) observed that increasing Re enhances the time-averaged lift coefficient by facilitating the suction effect on the upper side of the 2D rectangular cylinder at zero incident angle, while suppressing the suction of the lower side. These effects are attributed to changes associated with the vortex strength and the location of vortex cores on the upper and lower surfaces of the cylinder. More details on the wake of cylinders, their dynamics and models are presented in Chapter 3 for zero-incident angle, and Chapter 4 for non-zero incident angles.

2.1.2 Wake of a wall-mounted rectangular cylinder

Characterizing the wake of a wall-mounted rectangular cylinder has been the subject of various studies in fluid dynamics. Okuda and Taniike (1993) conducted one of the early studies on this subject. They attempted to find the source of the strong suction regions on the side and upper surfaces of a wall-mounted square prism at $Re = 1.6 \times 10^4$. Using flow visualization, three distinct structures were reported: inverted conical vortices on the side surfaces, standing conical vortices on the side surfaces, and a pair of conical vortices on the top surface. They captured inverted conical

vortex at the incidence angle of $i = 0°$ in a boundary layer with a thickness of $\delta/h = 0.52$, where δ and h are the boundary layer thickness and the height of prism respectively. Okuda and Taniike (1993) further determined that this structure vanishes at $\delta/h = 0.09$. Conversely and regardless of the boundary thickness, the other two structures are consistently observed at the incident angle of $i = 10°$ and $15°$.

Aspect ratio, incident angle, wall boundary layer thickness, and Reynolds number are important parameters that alter the characteristics of the wake of a wall-mounted cylinder. Thus, these topics have been the focus of research on unsteady wake dynamics. For example, Wang and Zhou (2009), Saha (2013), Rostamy et al. (2013), and Sumner et al. (2017) carried out studies to describe the influence of aspect ratio on the wake characteristics of a rectangular cylinder. Based on their results, changing aspect ratio can vary the type of wake flow structures, length of recirculation region, mean force coefficients, Strouhal number, and most importantly the maximum magnitude of upwash and downwash flow near the tip and wall regions, respectively.

The effect of incident angle was investigated by Castro and Robins (1977), Sakamoto (1985), Becker et al. (2002), McClean and Sumner (2014), and Unnikrishnan et al. (2017) at a range of Reynolds numbers and flow conditions. Based on their results, there is a critical incidence angle at which the mean drag coefficients and the size of the wake are minimum. This coincides with a maximized mean lift coefficient and Strouhal number. Moreover, the wake behaves in a highly asymmetric manner. Since the upwash flow near the wall region is inherently related to the boundary layer, Hosseini et al. (2013), El Hassan et al. (2015), and Sakamoto and Arie (1983) showed that changing the boundary layer characteristics can alter the type of wake structures. It can also influence the behavior of the horseshoe vortex in the wake. Furthermore, Kindree et al. (2018) showed that changing the state of boundary layer from laminar to turbulent can change the dominant frequency of the wake fluctuating motions and unsteady features.

The importance of Reynolds number on the wake development and evolution was established by the studies of Wei et al. (2001), Hwang and Yang (2004), and Rastan et al. (2017) for a wall-mounted rectangular cylinder. They reported that increasing Reynolds number changes the num-

ber of streamwise vortical structures in the wake. Zhang et al. (2017) used DNS at six different Reynolds numbers to show that changing the Reynolds number can also change the type of transitional wake flow structures as well. They divided the types of vortex shedding in the cylinder wake region into three different classes, namely "Core shedding,", "Reverse Core shedding", and "Hairpin shedding".

This section provided an overview of the main features of the wake, and flow parameters that are established to alter them. However, a more detail review of literature on the wake of wall-mounted cylinders is provided in Chapter 3 for zero incident angle, and Chapter 4 for non-zero incident angles.

2.1.3   Frequency Signatures

Unsteady flow features and coherent structures are often characterized by the frequency signature in the wake. For example, Wang and Zhou (2009) captured a single dominant frequency in the wake of a wall-mounted square (short depth-ratio) cylinder at $Re = 9300$. Their observation confirmed that there exists a single coherent structure in the wake of the cylinder. There are numerous other examples in the wake of bluff bodies, in which dominant frequencies are associated with distinct flow features and mechanisms (Sumner et al., 2004; Hemmati et al., 2016b).

Low- and high-frequency fluctuations are repeatedly observed in wakes (Jiang et al., 2015), which are associated with von-Kármán-type vortex shedding and shear-layer instabilities, respectively. However, observing very low-frequency fluctuations ($St \lll 0.1$), which lead to the formation of three-dimensional features in the wake are rare in literature (Zeiger et al., 2004). These very low-frequency fluctuations were first associated with the three-dimensional effects by Ayoub and Karamcheti (1982), who identified a flow regime connected to the cylinder tip that can be unstable and intermittent under some circumstances. A similar type of very low frequency was also reported by Jiang et al. (2015) in numerically studying flow around an inclined prolate spheroid. Kindree et al. (2018) also captured these very low-frequency fluctuations in the wake of a wall-mounted square (short depth-ratio) cylinder with an aspect ratio of $AR = 4$ at $5000 \leq Re \leq 19700$.

They mentioned that there is a connection between the low-frequency fluctuations and the state of the boundary layer. These studies, which are a handful of examples from a broader literature, imply that frequency signatures are critical tools to identify, characterize and track coherent structures and mechanisms in the wake of wall-mounted long cylinders. Further details on the literature regarding the Strouhal numbers observed in the wake of wall-mounted cylinders are provided in Chapters 3 and 4.

2.2   Computational Fluid Dynamics (CFD)

Computational Fluid Dynamics is based on numerically solving the Navier-Stokes equations under various settings and flow conditions, assumptions, boundary behaviors and initial characteristics (Versteeg and Malalasekera, 2007). This technique, which was initially established in early 1930s has received extraordinary attention over the past two decades with the development of faster and more stable computational tools. The extent and accuracy of CFD simulations vary depending on the flow Reynolds number, boundary conditions, physical scales, and non-linear behaviors, to name a few. To this end, accurate numerical simulation of the flow characteristics in the wake of a wall-mounted cylinder is a challenging problem due to the complex interactions of different wake structures. A detailed review of the solvers and CFD simulation setup employed in this thesis are presented in Chapters 3 and 4.

2.3   Turbulence Modeling

Accurate modeling and simulation of turbulence is an important part of CFD studies, especially when dealing with large Reynolds numbers and complex wakes. Recently, Guissart et al. (2019) conducted numerical and experimental studies on the wake of 2D rectangular cylinders at different angles of attack to show that more conventional turbulence models, such as Unsteady Reynolds-Averaged-Navier-Stokes (RANS) models and Delayed-Detached-Eddy-Simulations (DDES), cannot provide accurate estimates of the wake. For detached flow regimes, DDES provided better

results, while for attached flow regimes, Unsteady RANS provided more accurate results. Further-more, the stall angle cannot be precisely predicted using Unsteady RANS. Since flow structures around surface-mounted cylinders are strongly three-dimensional and more complicated than those for 2D cylinders (Zhang et al., 2017), selecting an appropriate method for simulating the turbulent wake is a critical factor in setting up the simulations in the current study. Shah and Ferziger (1997), Krajnovic and Davidson (1999), Uffinger et al. (2013), and Saeedi and Wang (2016) utilized LES to simulate the flow around a wall-mounted cylinder at a range of Reynolds numbers and flow conditions. They all confirmed, in comparison to experiments and other validated results, that LES succeeds in accurately capturing the main features of the mean and turbulent flow. Therefore, all the simulations in the present research are computed using LES formulations.

Large Eddy Simulations are based on volume-averaged Navier-Stokes equations, contrary to RANS models that are based on time-averaged equations (Davidson, 2020). LES formulation consist of spatial filtering of flow variables, mainly velocity and pressure, base on the smallest grid size. To this effect, structures with grid size scales (GS) are resolved, and those with subgrid scales (SGS) are modeled (Davidson, 2020). The complete formulation of LES is presented in Section 4.3.1. The simplest and one of the most reliable subgrid scale models is the Smagorinsky model. In this model, the required width of the filter is taken as the local grid size. The formulation of this model is as follows (Davidson, 2020):

$$\hat{\tau}_{ij}^{SGS} - \frac{1}{3}\delta_{ij}\hat{\tau}_{kk}^{SGS} = -\nu_{SGS}(\frac{\partial \hat{u}_i}{\partial x_j} + \frac{\partial \hat{u}_j}{\partial x_i}) = -2\nu_{SGS}\hat{S}_{ij}, \tag{2.9}$$

$$\nu_{SGS} = (C_S\Delta)^2|\hat{S}|, \tag{2.10}$$

$$\Delta = (\delta V_{ijk})^{\frac{1}{3}}. \tag{2.11}$$

Here, $\hat{\tau}_{ij}^{SGS}$ is the subgrid (SGS) stress tensor, $\hat{u}$ is the resolved velocity, Δ is the spatial filter width, and δV_{ijk} is the local volume grid size.

19

Smagorinsky model considers the value of C_S to be constant. However, further evaluation of the model has revealed that C_S depends on the flow conditions and it varies between 0.065 to 0.25 (Davidson, 2020). To capture the flow field more accurately, Dynamic Smagorinsky model is utilized, based on which C_S is calculated using the resolved flow quantities. Detailed formulation of Dynamic Smagorinsky model is presented in Section 4.3.1.

Chapter 3

EFFECT OF LARGE DEPTH-RATIO

3.1 Introduction

This chapter focuses on the wake of a square and a long rectangular wall-mounted cylinder at Reynolds numbers of 250 and 1000 at zero incident angle. Large Eddy Simulations (LES) are used to study the effect of a large-depth-ratio (length-to-height) on both steady and unsteady wake of cylinders. The results in this chapter aligns with the first objective of this thesis, which aims at characterizing and modeling the unique wake feature of a large depth-ratio rectangular cylinder at zero incident angle. For better understanding of the wake dynamics, the wake is compared with that of a short (small depth-ratio) cylinder at similar Reynolds numbers, and a model is developed and compared with that of a square cylinder.

The main objective of this chapter is to establish the effect of large depth-ratio on the cylinder wake, and particularly examine the change in unsteady wake transition for wall mounted cylinders with a large depth-ratio. The implications of a large depth-ratio can be significant since it allows for shear layer reattachment following its initial separation from the sharp-leading edge of the body. Moreover, the long cylinder allows examining the dynamics of the horseshoe vortex interaction on unsteadiness and three-dimensionality of the wake. The structure of this chapter follows a detailed description of the methodology and numerical setup in Section 3.3. The main results

and discussions are included in Section 3.4, which is followed by the summary of conclusions in Section 3.5.

3.2 Background

The flow structures around wall-mounted rectangular cylinders have been extensively studied in literature, partly due to their broad engineering applications and partly because of their complex dynamics. Particularly at low Reynolds numbers, understanding the wake of a wall-mounted long cylinder has major implications in improving the design of electronic chips for better cooling, biomedical devices and small heat exchangers (Rastan et al., 2017). Here, Reynolds number is defined as $Re = hU_\infty/\nu$, where h is the cylinder height, U_∞ is freestream velocity, and ν is the fluid viscosity. In these applications, a detailed understanding of the flow field around the cylinders can help enhance the performance of various devices, such as fast response accurate measuring equipment such as hotwires. Recent developments have revealed that existing experimental and numerical studies do not provide thorough description of the flow field in the detached flow regions of the cylinder (Cimarelli et al., 2018), although flow structures around short-depth (vertically oriented) cylinders are highly organized (Wang and Zhou, 2009).

Wake models have been developed for the flow around wall-mounted circular cylinders, which date back to the work of Taneda (1952). Since then, there has been several modifications and upgrades to these models based on the cylinder characteristics and flow field conditions, a summary of which is provided by Sumner (2013). Wang et al. (2004) proposed a comprehensive model for the wake of a wall-mounted rectangular cylinder, which is shown in Figure 3.1. In this model Wang et al. (2004) classified the wake vortices of a wall-mounted cylinder into four different structures. Tip and base vortices are created due to the downwash and upwash flow. The spanwise vortices are Kàrmàn type structures in the middle height of the body, and the horseshoe vortex is formed in front of the body and continue to the wake region (see Figure 3.1a). Later on Wang and Zhou (2009) modified this model base on their detailed experimental study of the near wake region immediately
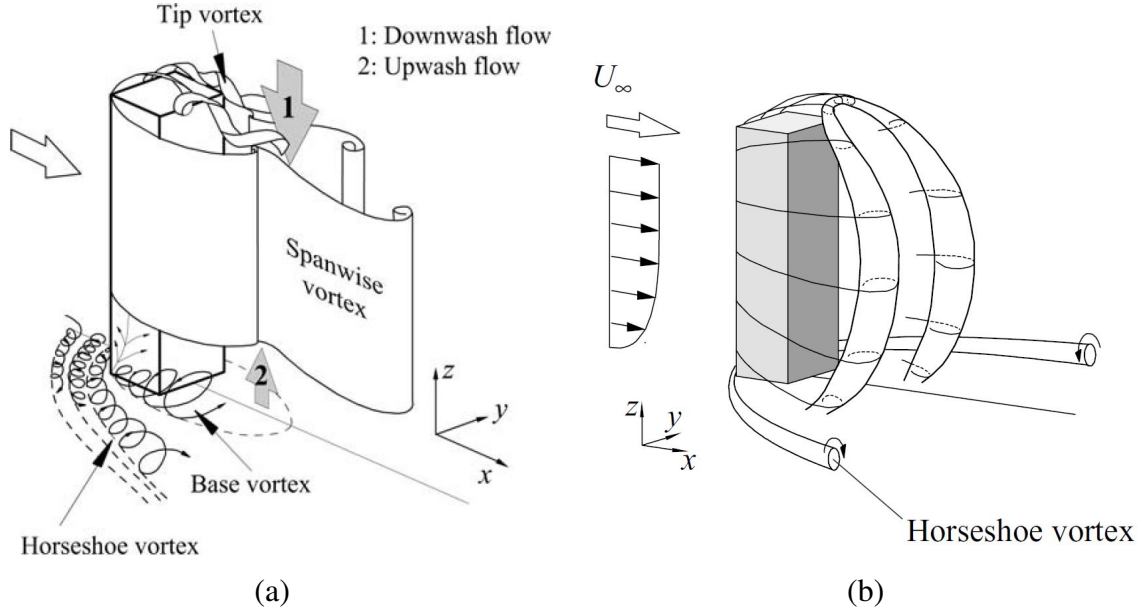
Figure 3.1: The wake models for wall-mounted square cylinders: (a) the original model developed by Wang et al. (2006)(Reprinted with permission from Wang et al. (2006), Copyright 2006, AIP Physics of Fluids); and (b) the modified model by Wang and Zhou (2009)(Reprinted with permission from Wang and Zhou (2009), Copyright 2009, Cambridge University Press)

behind the cylinder (see Figure 3.1b). This study revealed the presence of a single arc-like structure within the near wake region. They argued that spanwise, tip and base vortices are inherently connected and form an arch-type structure regardless of the aspect ratio of the cylinder. They also reported that both asymmetric and symmetric vortex shedding is observed simultaneously, but the probability of an asymmetrically arranged vortices is higher at the middle height of the object. The symmetric vortex shedding process in wall-mounted cylinders contributes to lowering the Strouhal number and aerodynamic forces (lift and drag) in comparison to two-dimensional cylinders.

Uffinger et al. (2013) investigated the effect of cross-sectional shape of a wall-mounted geometry (i.e.square cylinder, cylinder with elliptical after body, and cylinder with wedge in front) on its wake using both numerical and experimental methods at $Re = 1.28 \times 10^4$. They determined that cross-sectional shape of the cylinder affects the strength of the interaction between the flows over the top of the body and the Kàrmàn type vortices along the sides of the body. In another numerical study, Rastan et al. (2017) observed that there is one major difference between the wake of circular and square cylinders. Contrary to a circular finite wall-mounted cylinder, there is only one

23

dominant frequency along the span of a square finite wall-mounted cylinder. It is also notable that the vortex lines behind a square wall-mounted cylinder connect at the free end of the body. This suggests that there is only one coherent structure in the wake region behind the body (Rastan et al., 2017). However, Sattari et al. (2012) reported the presence of two different shedding regimes in the wake of a rectangular cylinder with a height-to-width ratio (aspect ratio) of 4 at $Re = 1.2 \times 10^4$. In addition to the normal antisymmetric Kàrmàn type vortex shedding, Sattari et al. (2012) identified the presence of symmetric vortex shedding with low amplitude wake fluctuations that exhibits $\pm 30°$ variation in the $180°$ phase shift of Kàrmàn type vortices. They also identified that symmetric vortex shedding can be identified in less than 20% of the time. The origin of this alternative shedding regime is attributed to the modification of Kàrmàn vortices with tip vortices. Thus, the probability of symmetric vortex shedding formation is higher near the tip region. It is also notable that the alternation between these two regimes changes the amplitude of the fluctuations, not the value of the dominant frequency.

Using Proper Orthogonal Decomposition (POD), Kawai et al. (2012) recognized that there are different wake structures with distinct frequencies formed around a wall-mounted square cylinder with aspect ratio of $AR = 2.7$, a small depth ratio and a thin boundary layer ($\delta/h = 0.3$, where δ is the boundary layer thickness) at Reynolds number of $Re = 9400$ and 15600. Similarly, Porteous et al. (2017) identified four shedding regimes in the wake of a wall-mounted square cylinder (small depth ratio) based on the number of peak frequencies observed in the wake flow fluctuations. Performing a detailed acoustic and hot-wire measurement in the wake with the parameter space that included $0.29 \leq AR \leq 22.9$, $\delta/\text{w}=1.3$ and $Re = 1.4 \times 10^4$, Porteous et al. (2017) reported the presence of no peak for Regime 0 ($AR < 2$), one dominant peak for Regime 1 ($2 < AR < 10$), two distinct peaks for Regime 2 ($10 < AR < 18$), and three peaks for Regime 3 ($18 < AR$). Moreover, Porteous et al. (2017) visualized the vertical vortex filaments in the near wake, based on which they determined that the filaments are connected near the free end for Regime 1. However, this horizontal connector was not captured for other regimes. Most recently, da Silva et al. (2020) identified multiple mean wake structures, instead of a single arc-type structure, formed around a

wall-mounted square cylinder (small depth ratio) with $AR = 3$ at $Re = 500$. It was suggested that these structures have different origins, contrary to the models discussed by Wang and Zhou (2009). Particularly, da Silva et al. (2020) showed that the structures on the upper surface of the cylinder appear to fade, while wake tip vortices are formed because of three-dimensional deflection of the separated flow from the side leading edges of the cylinder. Moreover, there is a spanwise vortex structure named "B_t" that is formed by the folding of the separated shear layer from the free end leading edge of the cylinder. This newly identified structure has a different origin from the so-called legs of the arc-type structures. da Silva et al. (2020) identified that the differences observed compared to the wake model of Wang and Zhou (2009) may be attributed to the transitional nature of the latter wake compared to the mean wake considered in the former study. These studies, although limited to small depth-ratios, have revealed that depending on the cylinder aspect ratio and Reynolds number, there are multiple structures formed in the wake with distinct characteristics.

The strong three-dimensionality of the wake of finite wall-mounted rectangular cylinders is due to the formation of a boundary layer near the wall-mounted end combined with the presence of downwash flow at the free end. This wake dynamics account for more complicated wake of finite wall-mounted cylinders compared to the flow structures around two-dimensional cylinders (Zhang et al., 2017). Since the strong flow-induced force fluctuations may cause severe vibrations, acoustic noises and structural damages around bluff bodies, investigation of the flow instabilities caused by cross-flow has been the focus of various research studies (Park and Yang, 2016; Zhang et al., 2017). For example, Yakhot et al. (2006) revealed that unsteady interactions of horseshoe vortex and the arc type vortex in the wake is the source of wake unsteadiness.

Using Direct Numerical Simulations (DNS), Saha (2013) illustrated that the strength of tip downwash flow, drag coefficient, Strouhal number, and wake flow unsteadiness of a short-depth (vertically oriented) cylinder increases with increasing aspect ratio. Later experimental studies of Sumner et al. (2017) examined the effect of aspect ratio at $Re = 4.2 \times 10^4$ and boundary layer thickness of $\delta/w = 1.5$. They identified how the wake dynamics changes when the cylinder aspect ratio approaches a critical value, which dictates the change in wake behavior of cylinders.

The flow incident angle with the cylinder is another parameter that can significantly change the wake dynamics. Castro and Robins (1977) compared the effect of $45°$ incidence angle on a cube placed in a uniform atmospheric boundary layer. Based on their research, the $45°$ incidence angle strengthen the effect of downwash flow on the near-wake region. It was also observed that the intensity of the downwash flow is higher when using a uniform inlet flow. Sakamoto (1985) found that the force coefficients and Strouhal number of fluctuations are highly dependent on the incidence angle of wall-mounted rectangular cylinder at $Re = 4.4 \times 10^3 - 1.17 \times 10^4$. They identified that there is a critical incidence angle at which the drag coefficient is minimum, while the Strouhal number obtained from lift fluctuations is maximum. McClean and Sumner (2014) investigated the effect of incidence angle on the lift coefficient, drag coefficient and the Strouhal number of fluctuations in the wake of finite square cylinders with different aspect ratios at $Re = 7.3 \times 10^4$. They reported that the critical incidence angle is higher for the finite cylinder compared to the infinite cylinder. The drag coefficient, Strouhal number, and their variations with respect to the incidence angle decreases for the finite cylinder. However, the magnitude of the lift coefficient is approximately equal for both cases.

The boundary layer thickness is another parameter that should be considered in studying the wake of wall-mounted cylinders. The horseshoe structures, and their corresponding interaction with other vortices in the wake, are dominated by the boundary layer dynamics. Based on the number of streamwise vortices in the wake, the wake structures can be classified into the dipole and quadrupole type structures. The latter appears when tip and base vortices exist simultaneously, while the former occurs when tip vortices are the only streamwise vortex structures in the wake. Hosseini et al. (2013) experimentally investigated the effect of boundary layer thickness on the wake of a rectangular cylinder with aspect ratio of 8 at $Re = 1.2 \times 10^4$. Their results showed that thickness of the boundary layer has a profound effect on the wake structures, and it can change them from quadrupole to dipole type even for a large aspect ratio cylinder. In their experimental studies, El Hassan et al. (2015) showed that the thickness of the incoming boundary layer can change the influence of horseshoe vortices in the wake behind a square cylinder. Using the

time-space cross-correlation map, they confirmed that the horseshoe vortex in the flow with larger boundary layer thickness affects the wake behind the cylinder, while this effect is weaker for the flow with smaller boundary layer thickness.

Wei et al. (2001) visualized the effect of increasing Reynolds number on the horseshoe vortex structure in front of a wall-mounted cylinder. They showed that increasing Reynolds number can make the horseshoe vortices oscillatory. Furthermore, these oscillations have a significant impact on the upstream velocity fluctuations. Zhang et al. (2017) conducted DNS simulations at six different Reynolds numbers and found that changing the Reynolds number can also change the types of flow structures behind the wall-mounted square cylinder. They identified a new type of transitional flow structure, namely "Six-Vortices" in addition to dipole and quadrupole structures. Using DNS, Rastan et al. (2017) classified the wake regimes of a short-depth (vertically oriented) cylinder with $AR = 7$ into five different regimes: steady flow ($Re < 75$), transition to unsteady flow ($75 < Re < 85$), laminar flow ($85 < Re < 150$), transition to turbulent flow ($150 < Re < 200$) and turbulent flow ($Re > 200$). They determined that the wake is characterized by dipole structures at $Re < 85$, whereas quadrupole structures dominate the wake at $Re > 150$. At $85 < Re < 150$ the wake is dominated by other structures that transition the wake into what is called Hexapole state. The presence of extra vortices in Hexapole wakes is attributed to the bending of streamlines at the lower part of the cylinder. These studies provided a detailed description of the wake of small depth ratio cylinders, while the effect of large depth ratios is unknown.

Arslan et al. (2013) and Yu et al. (2012) reported that flow-field characteristics of a two-dimensional cylinder can be accurately captured using Large Eddy Simulations (LES) at $Re = 1.21 \times 10^4$ and 10^5, respectively. Bruno et al. (2014) used both numerical and experimental studies at $Re = 2 \times 10^4 - 6 \times 10^4$ to examine the flow field characteristics around a two-dimensional cylinder with a chord to depth ratio of 5. They identified that different experimental measurements and numerical calculations of base pressure, drag and Strouhal number of wake unsteadiness are in good agreement. However, there exists a significant discrepancy between the numerically obtained mean flow features on the cylinder sides, lift force, mean pressure distribution and fluc-

tuating pressure compared to experiments. These variations were attributed to the sensitivity of these parameters to the computational and experimental setup and turbulence modeling techniques (Bruno et al., 2014). Guissart et al. (2019) used a combination of numerical and experimental studies to show that neither Unsteady Reynolds Averaged Navier-Stokes (UANS) nor Delayed Detached Eddy Simulations (DDES) can provide accurate estimation of the flow field around two-dimensional rectangular cylinder at different angles of attack and Re. For detached flow regimes, DDES provides better results, and for attached flow regimes, URANS provide more accurate results. It is also mentioned that the stall angle cannot be predicted using URANS. Nevertheless, LES remains a reliable method for capturing both steady and unsteady flow features in the wake of cylinders.

The unsteady wake features of a wall-mounted cylinder have been investigated with respect to the implications of the cylinder aspect ratio and incidence angle of the body, boundary layer thickness on the wall and the flow Reynolds number. However, there has not been any attempts to examine the implications of cylinder depth ratio (length-to-height ratio) on the wake development and evolution. Most importantly, the large depth ratio (long wall-mounted cylinder) enables the evaluation of horseshoe vortex dynamics implications on the orthogonal flow behavior in the wake and their related unsteadiness.

In this chapter, the effect of large depth-ratio on both steady and unsteady wake of wall-mounted cylinders are examined by comparing the wake of square and long rectangular (depth ratio of 4.16) cylinders at $Re = 250$ and 1000. The main objective of this chapter is to characterize the effect of large-depth-ratio on the cylinder wake, and evaluate how the wake topology is altered by changes to unsteady wake transition for wall mounted cylinders that exhibit a large depth-ratio.

3.3   Methodology

This chapter considers the flow around short-depth (square) and long-depth (rectangular) wall-mounted cylinders with a rectangular cross-sectional shape. The cylinder dominant height (h) is
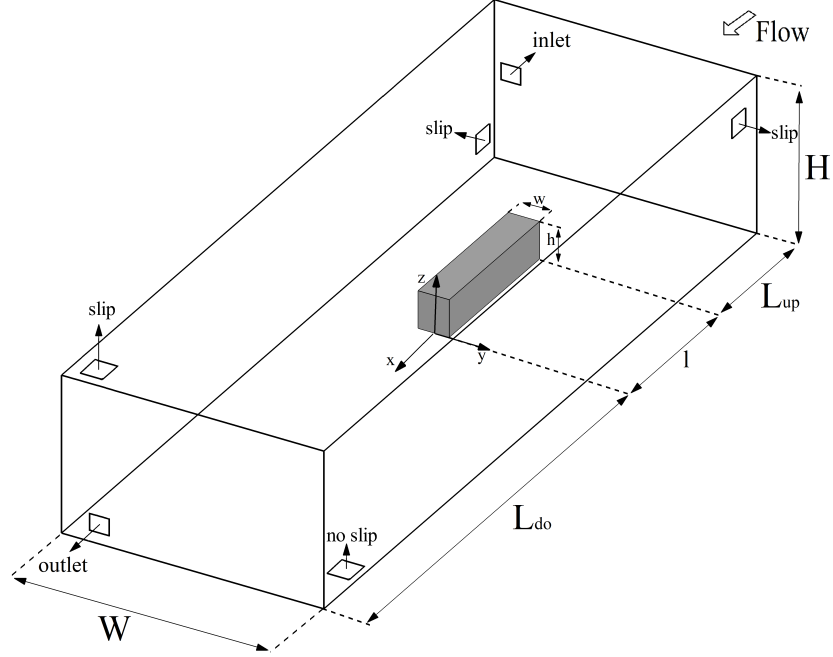
Figure 3.2: Schematic of the computational domain. (Not to scale)

used to normalize all dimensions and length-scales. For the long rectangular cylinder, the width is $w = 0.83h$ and the length (depth) is $l = 4.15h$, which implies a depth-ratio of $DR = 4.15$. The square cylinder has a width and length of $w = l = 0.83h$, which makes its depth ratio unity. The uniform inlet velocity corresponds to a Reynolds number of 250 and 1000 based on the cylinder height (h). The boundary layer formed on the ground has a thickness of $\approx 0.5h$ at the cylinder frontal face. The schematics of the cylinder is shown in Figure 3.2, in which the cylinder cross-sectional area is in the $yz-$plane and it extends in the streamwise ($x-$) direction. Details on the numerical setup, turbulence modeling and simulation verification are provided in this section.

3.3.1 Numerical Setup

Using Large Eddy Simulations (LES), we estimate the flow field around wall-mounted sqaure (short-depth) and long rectangular (long-depth) cylinders. The LES formulations are based on the spatial filtered incompressible Navier-Stokes and continuity equations, where the smaller flow scales (relative to the smallest grid-size) are modeled and larger-scales are solved directly. The

29

filtered continuity (Eq. 3.1) and momentum (Eq. 3.2) equations are solved using OpenFOAM:

$$\frac{\partial \hat{u}_i}{\partial x_i} = 0, \tag{3.1}$$

$$\frac{\partial \hat{u}_i}{\partial t} + \frac{\partial \hat{u}_i \hat{u}_j}{\partial x_j} = -\frac{1}{\rho} \frac{\partial \hat{p}}{\partial x_i} + \nu \frac{\partial^2 \hat{u}_j}{\partial x_i x_j} + \frac{\partial \hat{\tau}_{ij}^{SGS}}{\partial x_j}, \tag{3.2}$$

Here, $\hat{u}_i$ and $\hat{p}$ are the filtered resolved velocity and pressure, respectively, and $\hat{\tau}_{ij}^{SGS}$ is the sub-grid stress (SGS stress) tensor (Durbin and Reif, 2011):

$$\hat{\tau}_{ij}^{SGS} = \widehat{u_i u_j} - \hat{u}_i \hat{u}_j. \tag{3.3}$$

Dynamic Smagorinsky method is utilized to model the sub-grid scale flow features. Based on the Smagorinsky method, the SGS stress tensor is calculated using the eddy viscosity approach (Durbin and Reif, 2011):

$$\hat{\tau}_{ij}^{SGS} = -2\nu_{SGS}\widehat{S}_{ij} \tag{3.4}$$

$$\widehat{S}_{ij} = \frac{1}{2}(\frac{\partial \hat{u}_j}{\partial x_i} + \frac{\partial \hat{u}_i}{\partial x_j}) \tag{3.5}$$

$$\nu_{SGS} = (c_s \Delta)^2 \sqrt{2|\widehat{S}|^2} \tag{3.6}$$

$$|\widehat{S}| = \widehat{S}_{ij}\widehat{S}_{ji} \tag{3.7}$$

Here, $\widehat{S}_{ij}$ is the rate of strain tensor and the hat sign shows the filtered value of it. Δ is equal to

30

the cube root of the cells volume. The value of the Smagorinsky constant c_s is calculated in every timestep in the Dynamic Smagorinsky method using the following equations:

$$c_s{}^2 = -\frac{L_{ij}m_{ij}}{m_{kl}m_{kl}} \tag{3.8}$$

$$m_{ij} = 2^{\frac{2}{3}}\Delta^2\widehat{|\widehat{S}_{ij}|\widehat{S}_{ij}} - 2^{\frac{2}{3}}\tilde{\Delta}^2|\widetilde{\widehat{S}}_{ij}|\widetilde{\widehat{S}}_{ij} \tag{3.9}$$

$$L_{ij} = \widehat{\tilde{u}_i\tilde{u}_j} - \tilde{\hat{u}}_i\tilde{\hat{u}}_j \tag{3.10}$$

Here L_{ij} is the Leonard stress and the tilde sign represents the second filter applied to the flow data. Furthermore, numerical instabilities are avoided by bounding the constant c_s to positive values only, that is $c_s = max(c_s, 0)$.

The streamwise $(x-)$, spanwise $(y-)$, and normal $(z-)$ dimensions of the computational domain, shown in Figure 3.2, are $L = 35h$, $H = 6h$, and $W = 12h$, respectively. The front face of the body is located $L_u = 10h$ from the inlet and $L_d = 20h$ from the outlet. A non-homogeneous grid made of 4.4×10^6 and 3.7×10^6 hexahedral elements are used for the rectangular and square cylinders at $Re = 250$, respectively. The number of elements for the long rectangular cylinder at $Re = 1000$ increases to 10.3×10^6 hexahedral elements. The spatial grid distribution for the long rectangular cylinder at $Re = 1000$ is shown in Figure 3.3. The grids are designed so that the maximum value of y^+ is below 0.55 at the walls, which enables capturing flow fluctuations associated with separated flow. The timesteps are set for each case such that the maximum CFL number remained below 0.8. The spatial and temporal discretization of the governing equations are second-order accurate. The residual momentum root-mean-square of 10^{-6} was set as the criteria for convergence for each timestep. The PIMPLE algorithm, which is a combination of Pressure Implicit with Splitting of Operator (PISO) and Semi-Implicit Method for Pressure-Linked Equa-
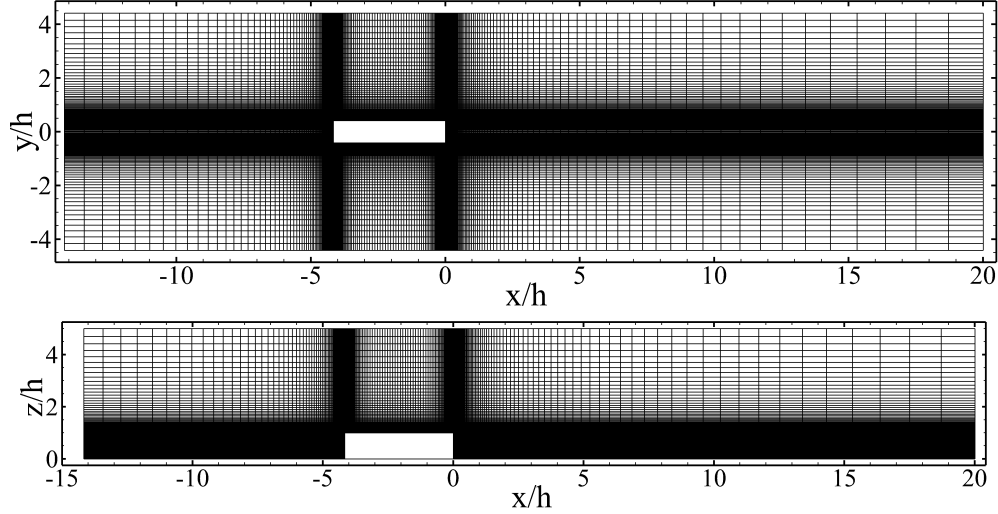
Figure 3.3: The spatial grid distribution for the long-rectangular cylinder at $Re = 1000$. Top view at $z/h = 0.5$ (top) and side view at $y/h = 0$ (bottom).

tions (SIMPLE) methods, is used for coupling the pressure and velocity fields. The computational domain for each case is divided into 16 separate regions for parallel computations. The simulations are completed using Intel Platinum 8160F Skylake 2.1GHz cores at 15000 core hours on average.

The constant uniform velocity is applied as the inlet boundary condition. Sides and upper walls of the domain are set to slip boundary condition. The outlet boundary is set as the Neumann boundary condition ($\partial \phi / \partial n = 0$, where ϕ is any flow variable). The no-slip boundary condition is applied to the ground and body faces.

3.3.2   Verification

The domain size is known to affect numerical results, and so does the spatial grid quality (Hemmati et al., 2018). To address the former, we designed our computational domain such that its size exceeds those of Shah and Ferziger (1997), Krajnovic and Davidson (1999) and Yakhot et al. (2006) for a single cube, and Krajnovic and Davidson (2005a,b) for an Ahmed body. The numerical setup of previous studies are compared with those of the current study in Table 3.1. Furthermore, we completed a sensitivity study on the computational domain size using three different domains for the LES simulation of the long rectangular cylinder: Domain 1, Domain 2 and Domain 3.

32

Table 3.1: Numerical setup comparison between current and previous studies.

	Method	Body Shape	Re	Domain Size($\times h$)	y^+_{max}
Current Study - Domain 1	LES	Rect. Cylinder	2.5×10^2	$35 \times 9 \times 5$	0.55
Current Study - Domain 2	LES	Rect. Cylinder	2.5×10^2	$35 \times 12 \times 6$	0.55
Current Study - Domain 3	LES	Rect. Cylinder	2.5×10^2	$40 \times 16 \times 6$	0.55
Current Study - Grid 1	LES	Rect. Cylinder	2.5×10^2	$35 \times 9 \times 5$	1.3
Current Study - Grid 2	LES	Rect. Cylinder	2.5×10^2	$35 \times 9 \times 5$	0.9
Current Study - Grid 3	LES	Rect. Cylinder	2.5×10^2	$35 \times 9 \times 5$	0.55
Shah and Ferziger (1997)	LES	Cube	4.0×10^4	$10 \times 7 \times 2$	−
Krajnovic and Davidson (1999)	LES	Cube (2D)	4.0×10^4	$10 \times 7 \times -$	1.1
Yakhot et al. (2006)	DNS	Cube	5.6×10^3	$14 \times 6.4 \times 3$	$0.76 - 6.46$
Krajnovic and Davidson (2005a)	LES	Ahmed body	2.0×10^5	$31.9 \times 6.5 \times 4.9$	0.33
Uffinger et al. (2013)	LES	Square Cylinder	1.3×10^4	$40 \times 11 \times 11$	−
Saeedi and Wang (2016)	LES	Square Cylinder	1.2×10^4	$28 \times 13.4 \times 9$	0.59
Zhang et al. (2017)	DNS	Square Cylinder	$\leq 10^3$	$24 \times 16 \times 10$	−
Rastan et al. (2017)	DNS	Square Cylinder	$\leq 2.5 \times 10^2$	$24 \times 16 \times 13$	−

Table 3.2: Numerical Results for different Grids and Domains

	Number of Grid points (M)	$\overline{C_d}$	$\overline{C_l}$
Grid 1	2.2	1.0035	0.3959
Grid 2	2.8	1.1008	0.2887
Grid 3	3.8	1.1035	0.2910
Domain 1	3.8	1.1035	0.2910
Domain 2	4.1	1.0573	0.2516
Domain 3	4.4	1.0515	0.2389

The results for the three cases are compared in Figure 3.4 and Table 3.2. These results show that the maximum difference between the two consecutive cases is less than 5%, which suggests that Domain 2 is adequate to accurately capture the flow features.

The effect of the grid resolution on the simulation results are investigated using the setup of Domain 1 with three different grids that employ incremental refinements: Grid 1 ($190 \times 133 \times 86$ elements), Grid 2 ($210 \times 142 \times 93$ elements) and Grid 3 ($235 \times 163 \times 100$ elements). The results of these simulations are presented in Figure 3.4, which make apparent that the maximum variation between Grid 2 and Grid 3 is less that 1%. This indicates that the mesh for Grid 2 is sufficient to capture the main flow features.

Another parameter that indicates the grid quality is the ratio of the grid size ($\Delta = (\Delta x \times \Delta y \times \Delta z)^{\frac{1}{3}}$) to Kolmogorov length scale (η). To this effect, the flow dissipation rate (ε') is calculated using the gradient of fluctuating velocity throughout the domain (Saeedi et al., 2014; Yakhot et al., 2006). According to Moin and Mahesh (1998), the accurate computation of the flow field char-
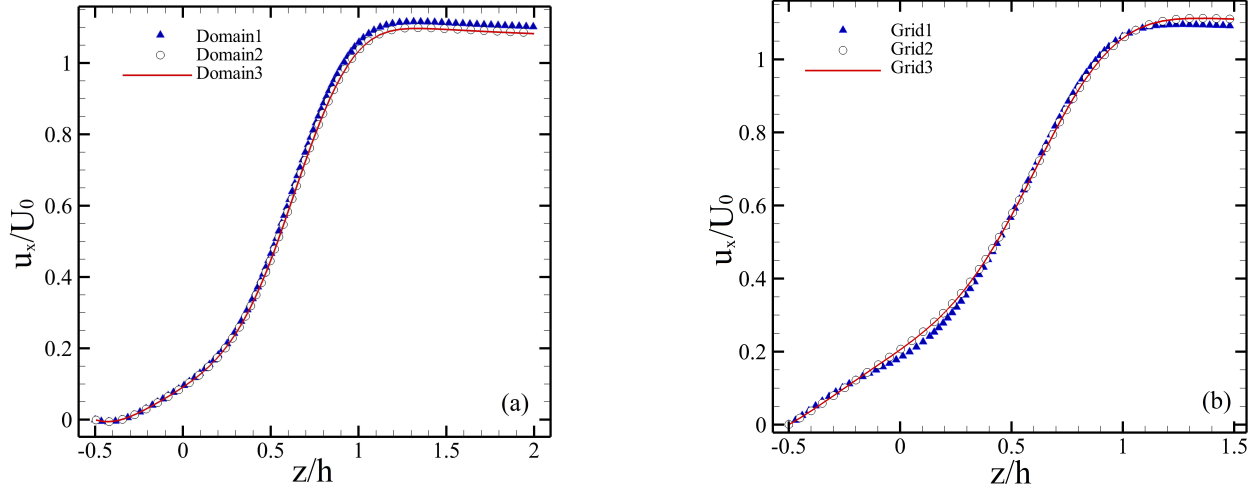
Figure 3.4: Comparing the profile of time-averaged streamwise velocity ($\bar{u}/U_0$) in the wake of the long rectangular cylinder using different (a) domain sizes (at $x/h = 2$ and $y/h = 0$), and (b) spatial grids (at $x/h = 3$ and $y/h = 0$).

acteristics requires that the smallest resolved length scale be of the same order of magnitude as the Kolmogorov length scale ($O(\eta)$). By simulating the flow in the wake of a wall-mounted cube, Yakhot et al. (2006) further reported that the criterion of $2 \leq \Delta/\eta \leq 5$ at the critical regions of the flow, i.e., horseshoe and tip vortices, is an appropriate measure for the grid refinement of DNS simulations. As shown in Figure 3.5a, the ratio of the grid size to Kolmogorov length scale for the case of $45°$ incidence angle at Reynolds number of $Re = 250$ in the mid-height plane is less than 2. For the case of $0°$ at Reynolds number of $Re = 1000$ in the mid-height plane is less than 40. However, in the near wake region the quality of the grids are high enough to capture the flow details. The mid-height plane for these two cases constitute the location of the largest velocity gradients in an unsteady wake amongst all simulations, which hints at the accuracy of the numerical results. The prepared grid is more refined close to the ground plane or top of the cylinder in comparison to mid height. Thus, the ratio of grids to Kolmogorov scale is lower in those regions (not shown here for brevity).

(a)$Re = 250, i = 45°$

(a)$Re = 1000, i = 0°$
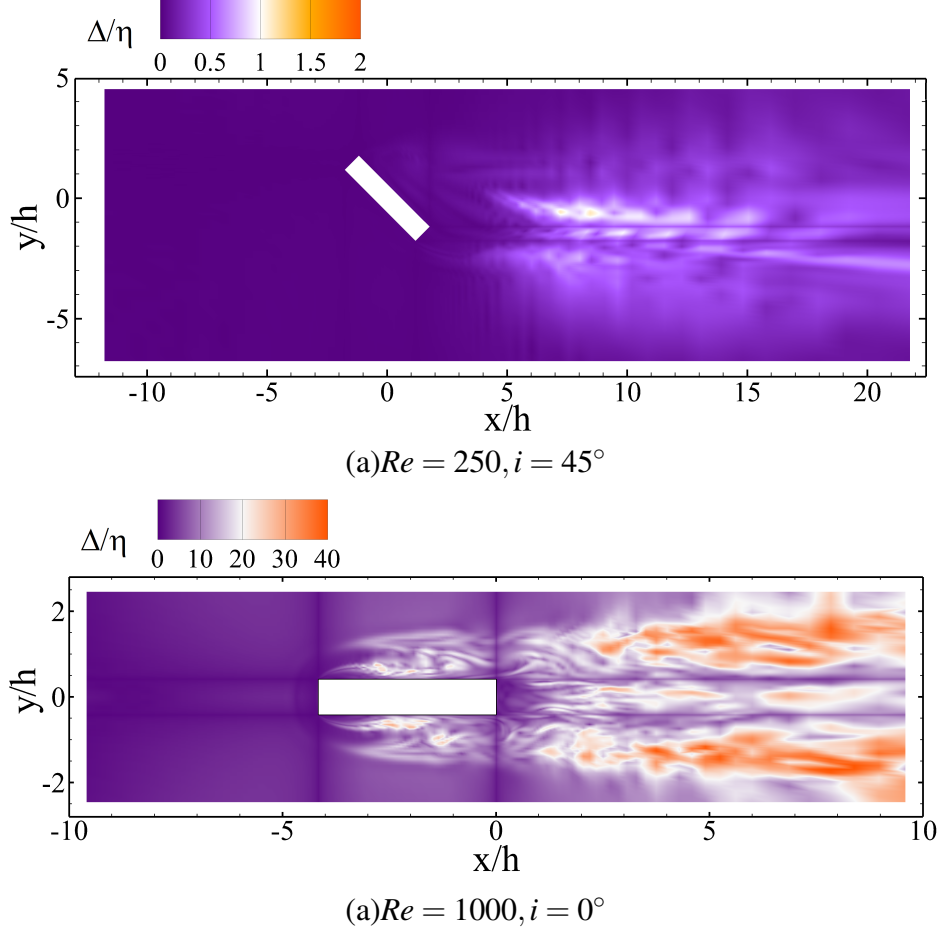
Figure 3.5: The ratio of spatial grid size to the Kolmogorov length scale in the mid-height plane

3.3.3   Validation of results

There are no comprehensive studies, to the best knowledge of the authors, on the wake of the cylinders considered here for comparison in terms of their shape, dimensions and Re. Thus, we considered the wake of a square cylinder of $AR = 2$ to validate the results of our simulations in comparison to the existing numerical studies. Particularly, we simulated the wake of a vertical oriented square cylinder of $AR = 2$ to compare the results with those of Saha (2013) at $Re = 250$. The calculated mean drag coefficient in the current study is $\overline{C_d} = 1.145$, which is within $\approx 6\%$ of the reported value of $\overline{C_d} = 1.08$ by Saha (2013). Furthermore, mean streamwise velocity profile at $x/d = 3$ and $z/d = 1.5$ and spanwise velocity profile at $x/d = 7$ and $z/d = 1$ are compared with those of Saha (2013) in Figures 3.6b and 3.6c, respectively. The profiles collapse well with
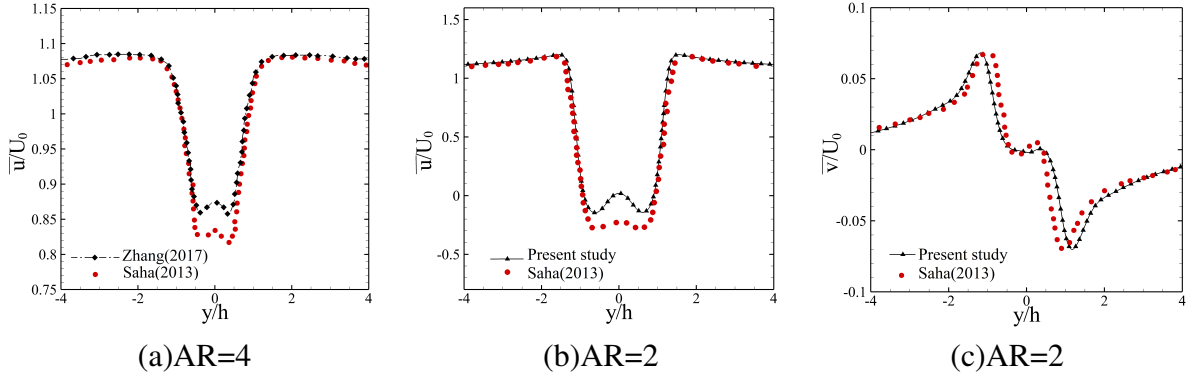
Figure 3.6: Time-averaged streamwise and spanwise velocity distributions at $Re = 250$ behind a rectangular cylinder at (a) $x/d = 7$ and $z/d = 3.5$ (b) $x/d = 3$ and $z/d = 1.5$ (c) $x/d = 7$ and $z/d = 1$
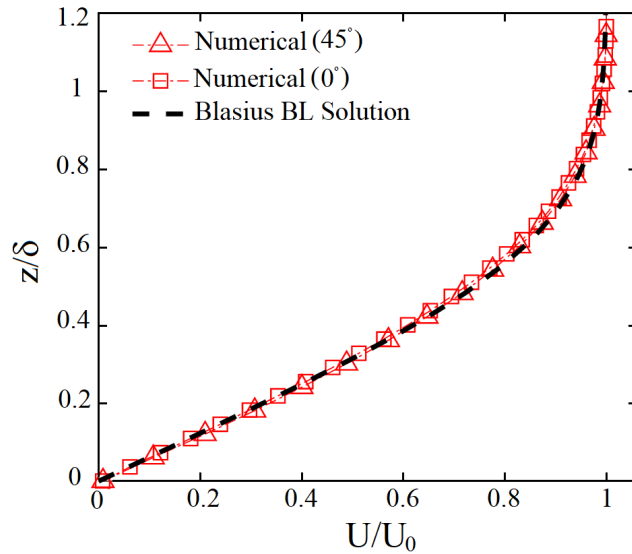
Figure 3.7: Boundary layer profiles prior to reaching the cylinder at $x/h = -4.15$ and $y/h = 6$ compared with the Blasius Boundary layer solution.

small discrepancies on the extent of the streamwise velocity deficit. As shown in Figure 3.6a, the direct numerical simulations of Zhang et al. (2017) for the flow around a square cylinder with $AR = 4$ also reported similar discrepancies compared to the results of Saha (2013) for a similar cylinder. These variations may be due to the differences in numerical tolerance, the solvers, and the boundary layer. As another validation, we compared the boundary layer profile in the present study with the laminar Blasius boundary layer profile in Figure 3.7. The good agreement between these profiles is another verification for the accuracy of the present numerical simulations.

Table 3.3: Time-average coefficients of lift ($\overline{C_l}$) and drag ($\overline{C_d}$) for both cylinders at $Re = 250$

Cases	$\overline{C_l}$	$\overline{C_d}$
Long (Rectangular) Cylinder	0.239	1.052
Short (Square) Cylinder	0.311	0.835

We further compare the coefficients of drag and lift for the square and long rectangular cylinders presented in Table 3.3 with the analytically predicted values of $\overline{C_d}$=1.07−1.2 for a square cross-section bluff body in White (1999). The $\overline{C_d}$ value for a flat-faced cylinder with a depth ratio of 1.0 (similar to the square cylinder here) is estimated to be 0.9 at $Re = 10^4$. The coefficient of drag depends strongly on Reynolds number, based on which it is reasonable to expect the value of $\overline{C_d}$ at $Re = 250$ to be lower than what was reported analytically. The small discrepancies with numerical results of Saha (2013) suggest that the simulation provide a sufficiently accurate prediction of the flow field.

3.4 Results

We begin by first considering the wake of the cylinders at Reynolds number of 250 and then at $Re = 1000$. The wake features are thoroughly examined and compared between the square (small-depth-ratio) and long rectangular (large-depth-ratio) cylinders to characterize the effect of a large-depth-ratio on the wake development. It is apparent that the wake of both cylinders are steady at $Re = 250$, while they appear to have transitioned to an unsteady wake at $Re = 1000$.

3.4.1 Steady Wake ($Re = 250$)

The flow around a wall-mounted rectangular cylinder with an aspect ratio of 2.00 and $DR = 0.50$ at $Re = 250$ has been characterized as weakly unsteady by Saha (2013). However, we observe that the simulated flow fields around both the square cylinder ($DR = 1.00$ and $AR = 1.20$) and long rectangular cylinder ($DR = 4.15$ and $AR = 1.20$) are steady at $Re = 250$. The velocity and pressure are examined at 45 different points within the near and far wake of both cylinders through time,

which showed no dominant frequencies or weakly unsteady characteristics. The flow steadiness can be attributed to the suppression of the Kàrmàn type vortices by downwash and upwash flow created close to the top and bottom of the cylinders, respectively. This indicates that decreasing the aspect ratio of a rectangular wall-mounted cylinder, for the case of the square cylinder, and increasing the depth ratio to such large values > 4, for the case of a long-rectangular cylinder, have similar implications on eliminating the wake unsteadiness at low Reynolds numbers. We tested a higher aspect-ratio square cylinder case for validation, which showed unsteadiness at $Re = 250$, similar to the observations of Saha (2013).

We now turn our attention to the flow field and main characteristics of the wake. The critical points on different faces of the long rectangular and square cylinder are shown in Figures 3.8 and 3.9, respectively. The nodal, saddle and focal points are identified as N, S, and F, respectively. Critical points are identified in the wake using streamlines on 2D planes both on and around the cylinders. The total number of nodal, focal, and saddle points for the long cylinder are 14, 4, and 18, respectively. This agrees with the predictions of Tobak and Peake (1982), Chapman and Yates (1991) and Délery (2013). According to Tobak and Peake (1982), Chapman and Yates (1991) and Délery (2013), there is a critical point theory for a wall mounted object, which also holds here:

$$\Sigma(N+F) - \Sigma(S) = 0. \tag{3.11}$$

There is, however, a different wake topology expected for the square cylinder, in which case the subtraction of the number of saddle points from (nodal+focal) points around a wall-mounted cube is equal to 2, according to Liakos and Malamataris (2014). Based on the visualization of the critical points around the square cylinder in Figure 3.9, the total number of nodal, focal, and saddle points around the square cylinder are 13, 6 and 17, respectively. Thus, the subtraction of (nodal+focal) and saddle point is equal to 2, which agrees with the Liakos and Malamataris (2014). It appears that two pairs of saddle points that are present on the side of the long rectangular cylinder (see Figure 3.8a) are merged in the case of the square cylinder. This leads to a decrease on the number of
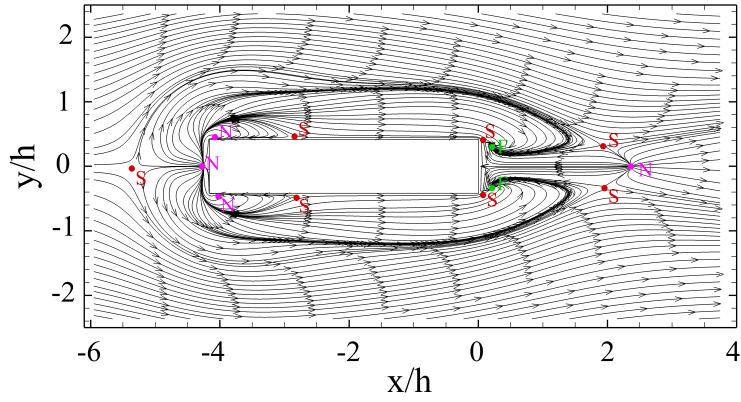
(a) ground
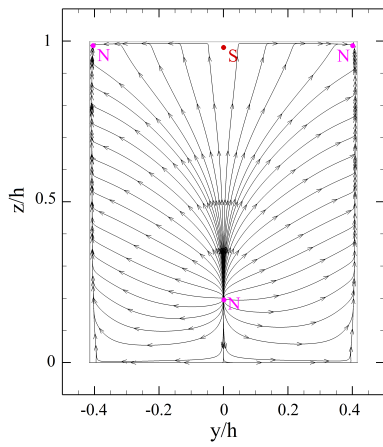
(b) rear face
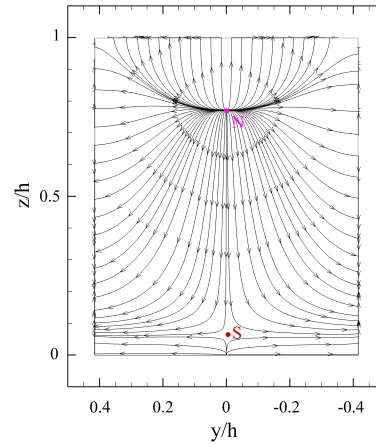
(c) front face

(d) side face

(e) upper face

Figure 3.8: Critical points on the faces of the long-rectangular cylinder at $Re = 250$.

(a) ground

(b) rear face

(c) front face

(d) side face

(e) upper face

Figure 3.9: Critical points on the faces of the square cylinder at $Re = 250$.

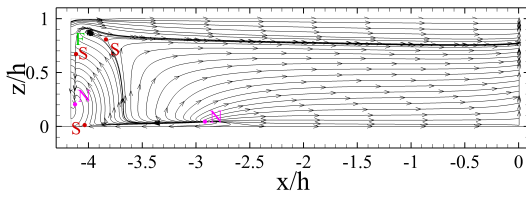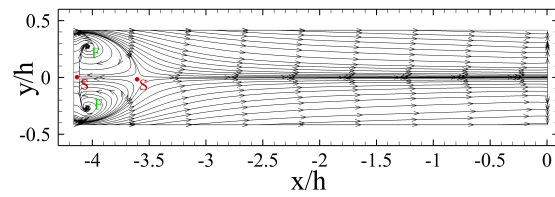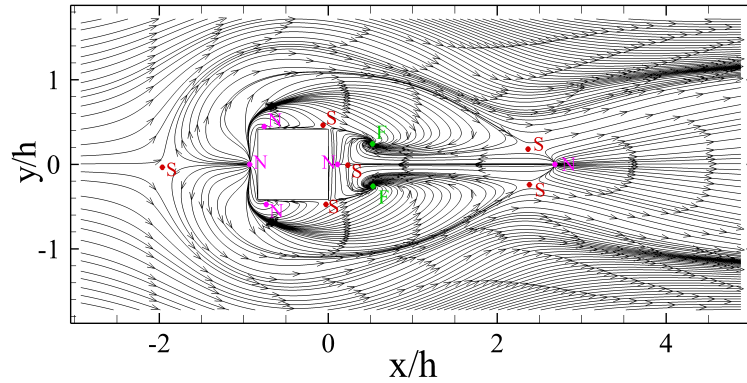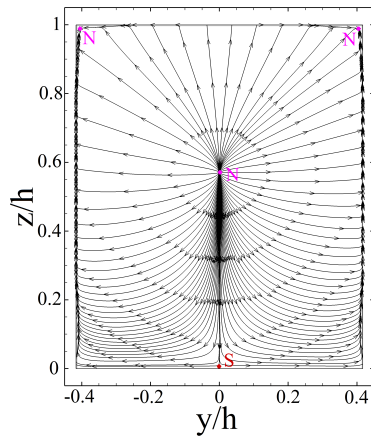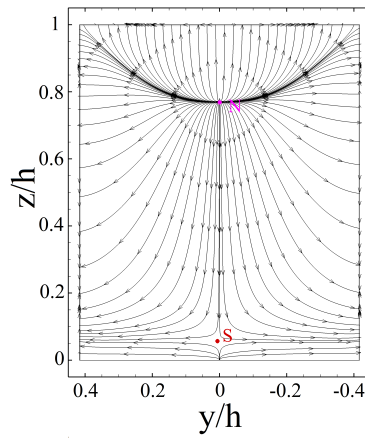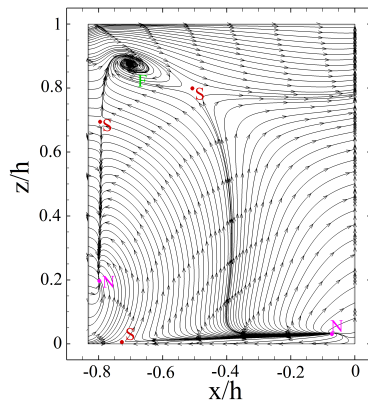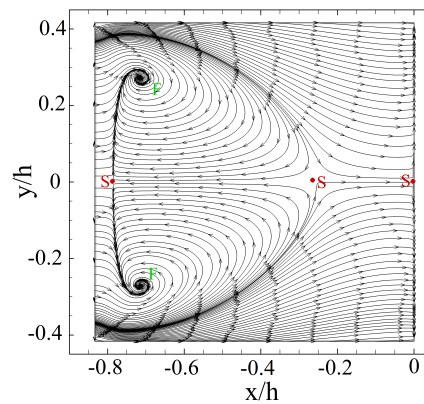the saddle points compared to nodal points in case of the square cylinder, which indicates that Eq. 3.11 can be different for a wall-mounted object based on the conditions of the study. Furthermore, there are some differences between the distribution of critical points on the wall-mounted cube in Liakos and Malamataris (2014) and the square cylinder wake in the current study. For example, they reported the presence of some saddle and nodal points on the edge between front and ground faces close to the side faces. These critical points, however, are not observed in the current study. These variations are expected due to the differences in geometries and thickness of the boundary layer. Moreover, comparing with Liakos and Malamataris (2014), the distribution of critical points on the long rectangular cylinder at $Re = 250$ is similar to the distribution of critical points on a cube at $Re \geq 1000$.

Looking at the results in Figures 3.8b and 3.9b, the nodal and saddle points on the rear face of the square cylinder (at $y/h = 0$) are formed farther from the ground compared to the long rectangular cylinder. This difference can be attributed to the more significant upwash flow in the wake of the square cylinder, which will be discussed later. It is also notable that there is not any saddle point on the upper rear face of the square cylinder. Alternatively, as shown in Figure 3.9e, there is a saddle point on the ending part of the upper face of the square cylinder, which indicates that there is a small region of reversed flow towards the trailing edge of the square cylinder upper face. Another significant difference of the distribution of critical points on faces of the square and long cylinder is that there exists an additional attachment nodal point and a saddle point behind the square cylinder in Figure 3.9a. The attachment nodal point is formed because of the interaction of the separated shear layer with the rear face of the cylinder. The saddle point is also the result of the interaction of the former nodal point and the last nodal point of the wake region.

The iso-surfaces of $Q-$criterion are shown in Figure 3.10 from two perspectives, representing the frontal and rear faces of the cylinder. The plots in Figures 3.10c and 3.10d identify that the separated shear layer from the leading edge of the square cylinder is connected to the wake structures, which agrees with the existing model (Wang and Zhou, 2009). For the long rectangular cylinder, however, the structures are separated between the leading and trailing edge of the cylinder in Fig-
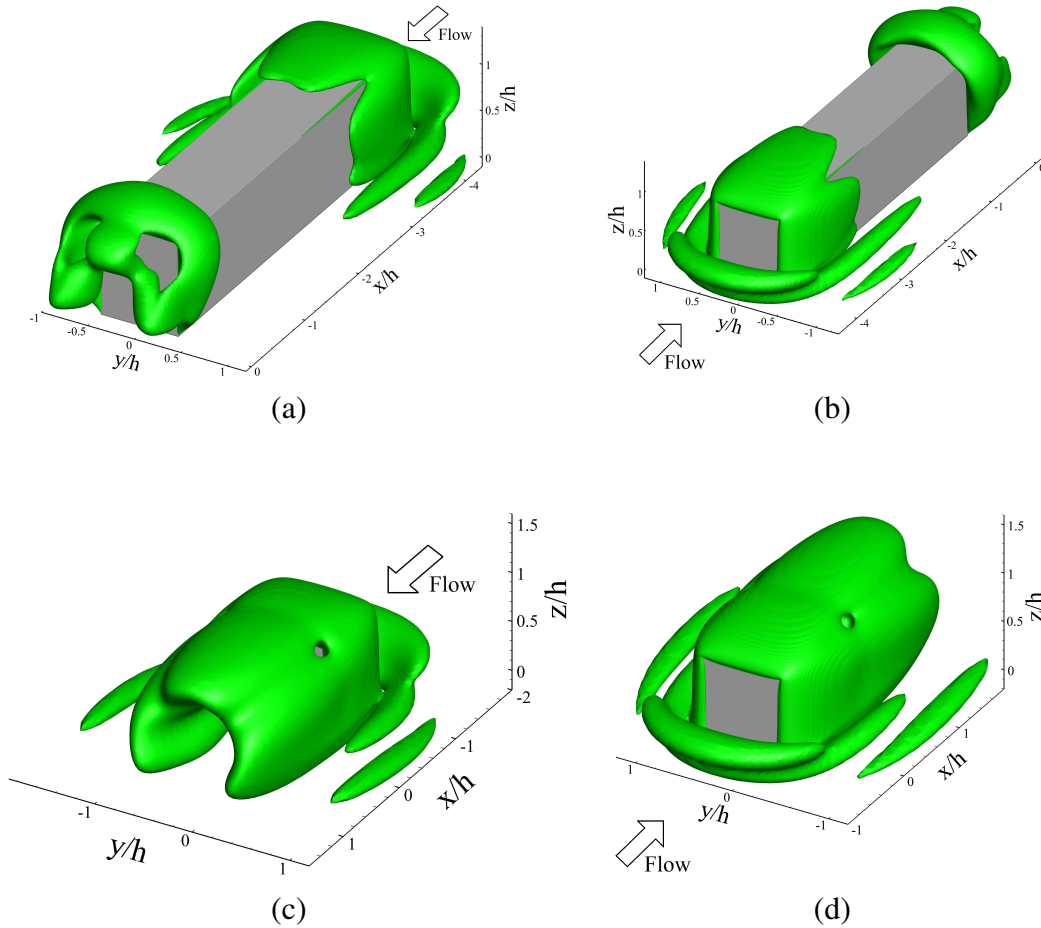
Figure 3.10: The isosurface of $Q = 30$ in the wake of the (a,b) long-rectangular cylinder, and (c,d) square cylinder at $Re = 250$.

ures 3.10a and 3.10b. Furthermore, the legs of the horseshoe vortex are extended into the wake and interact with the structure formed behind the square cylinder. This can directly impact the wake dynamics. Conversely, the wake structure of the long cylinder is located at a relatively long distance from the legs of the horseshoe vortex. The shorter depth of the square cylinder allows for interaction of the wake structures on the trailing edge of the cylinder, while the horseshoe vortex legs formed around the long rectangular cylinder diffuse before reaching the trailing edge of the cylinder. Thus, there is no interaction between horseshoe structure and the wake behind the body. This changes the wake model originally developed for short cylinders.

The effect of large depth-ratio on upwash flow is apparent in Figure 3.11, where there is evidence of a strong upwash flow for the square cylinder and not the long-rectangular cylinder. The

upwash effect in the wake of the long rectangular cylinder is very narrow and limited to the vicinity of the cylinder rear face (see Figures 3.11a−c). This difference in wake behavior is associated with the change in interaction between the horseshoe vortex and the tip structure at the trailing of the cylinder. However, this behavior is not observed for a large-depth-ratio cylinder. Moreover, this provides further evidence in comparison to the larger aspect ratio cylinders (i.e., $AR = 2$ in Saha (2013)) that the height of the boundary layer at the cylinder rear face plays an essential role in the wake flow characteristics. Another critical difference between the two cylinders is related to the downwash flow in the middle of the long-rectangular cylinder, where there is a stronger downwash effect in the outer regions. This observation is also supported by the streamline plots on 2D planes of Figure 3.12. This implies that the entrainment of the freestream flow due to the separated shear layer increases the strength of the upwash and downwash flow. However, its effect on the upwash flow is more apparent near the symmetry plane, whereas its effect on the downwash is more evident close to the junction of the side and rear faces.

As shown in Figures 3.12 and 3.13, the cross-flow in the wake is symmetric for both cylinders (the small cylinder is not shown for brevity). However, the presence of the boundary layer effects along the $z-$direction leads to a strongly antisymmetric wake in the normal ($z-$) direction. In the normal mid-plane of the cylinder (middle plane in the $z-$direction), there are focal points that correspond to laminar vortical structures in the wake (see Figure 3.13b). It can be seen from the contours superimposed on the isosurface of $Q-$criterion (Figures 3.12 and 3.13) that the rotational motion of the wake structure at a lower height (close to the ground) and higher part of the long-rectangular cylinder are restricted to the $z-$ and $y-$directions, respectively. The interconnection of these structures, which is apparent from the combination of 2D (streamline and contours) and 3D (iso-surface) visualizations, implies that their behavior is within a single structure that deforms and diffuses in the wake. The separation bubble close to the leading edge of the body is highlighted in Figure 3.12b, on the mid-plane of the cylinder, which does not extend into the outer wake. This implies that the reattachment on the cylinder upper face is stationary and it does not contribute to the tip structure typically formed on the cylinder rear, as per the model of Wang and Zhou

Long Rectangular Cylinder

Square Cylinder

(a) y/h=-0.35

(d) y/h=-0.35

(b) y/h=0

(e) y/h=0

(c) y/h=0.35

(f) y/h=0.35
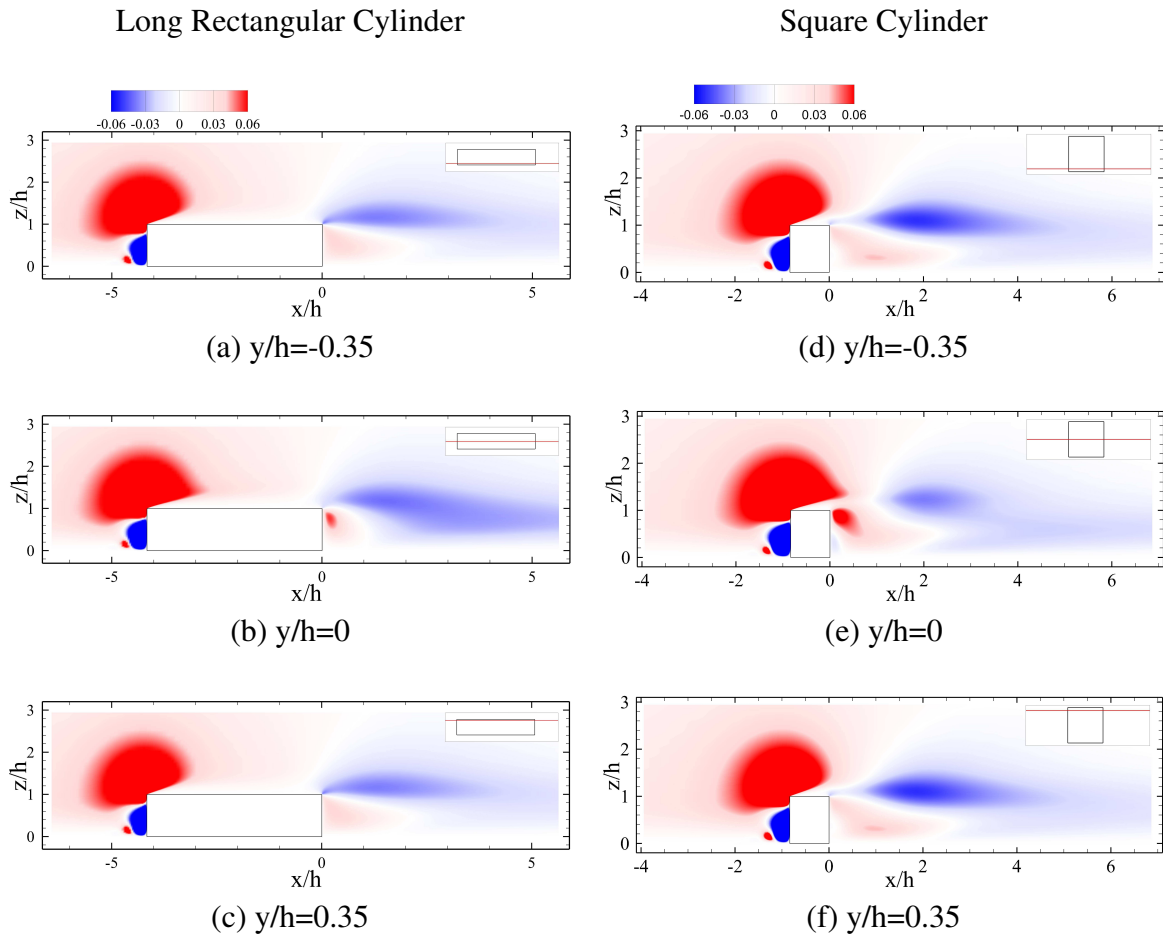
Figure 3.11: The contours of normal velocity component at different planes along (a−c) the long rectangular cylinder and (d−f) the square cylinder at $Re = 250$. The regions highlighted with red and blue colors in the wake of the cylinders show the upwash and downwash flow regions, respectively.

(a) y/h=-0.35

(b) y/h=0

(c) y/h=0.35
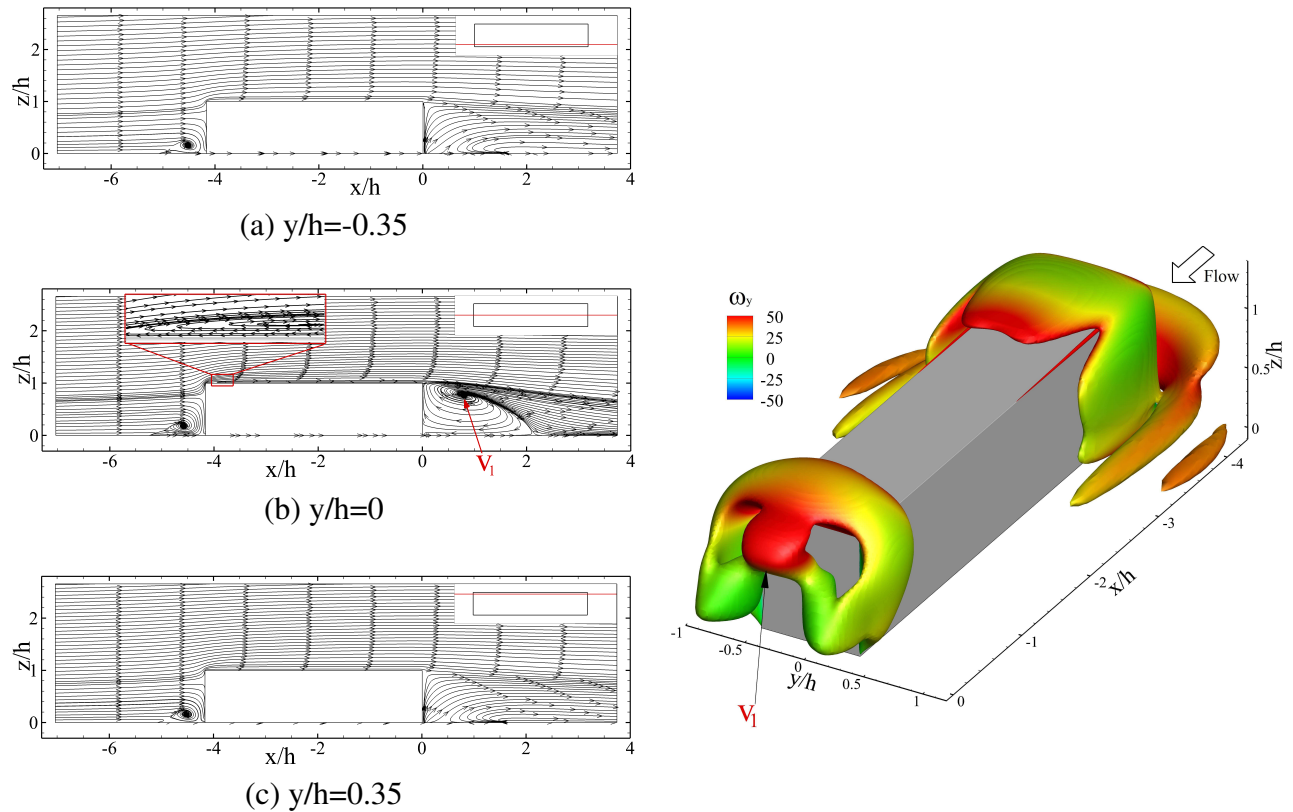
Figure 3.12: Isosurface of $Q = 30$ and side view of the wake structure of the long cylinder at $Re = 250$.

(2009). There also exists the same separation bubble on sides of the long-rectangular cylinder (Figure 3.13b) as it was also observed on the top face of the cylinder in Figure 3.12b. The side-bubbles also appears on the mid-plane for the cylinder, similar to the top-face bubble. Comparing such behaviors to the wake of the square cylinder in Figures 3.14 and 3.15, there is a similarity in the formation of bubbles on top and side faces of the cylinder. However, there appears to be a significantly larger laminar structure in the outer wake of the square cylinder, which leads to a large flow entrainment (downwash flow) compared to the long-rectangular cylinder. The center of the wake structure behind the square cylinder in Figure 3.14b is $0.5h$ farther away from the rear face of the cylinder compared to the long-rectangular cylinder in Figure 3.12b.

The streamline plots of Figure 3.15b identify a larger streamline curvature angle of $18.4°$ in the immediate wake of the square cylinder compared to the long rectangular cylinder, where curvature angle is $10.9°$ in Figure 3.13. The curvature angles are measured close to the mid-height plane at

(a) z/h=0.05

(b) z/h=0.5

(c) z/h=0.95
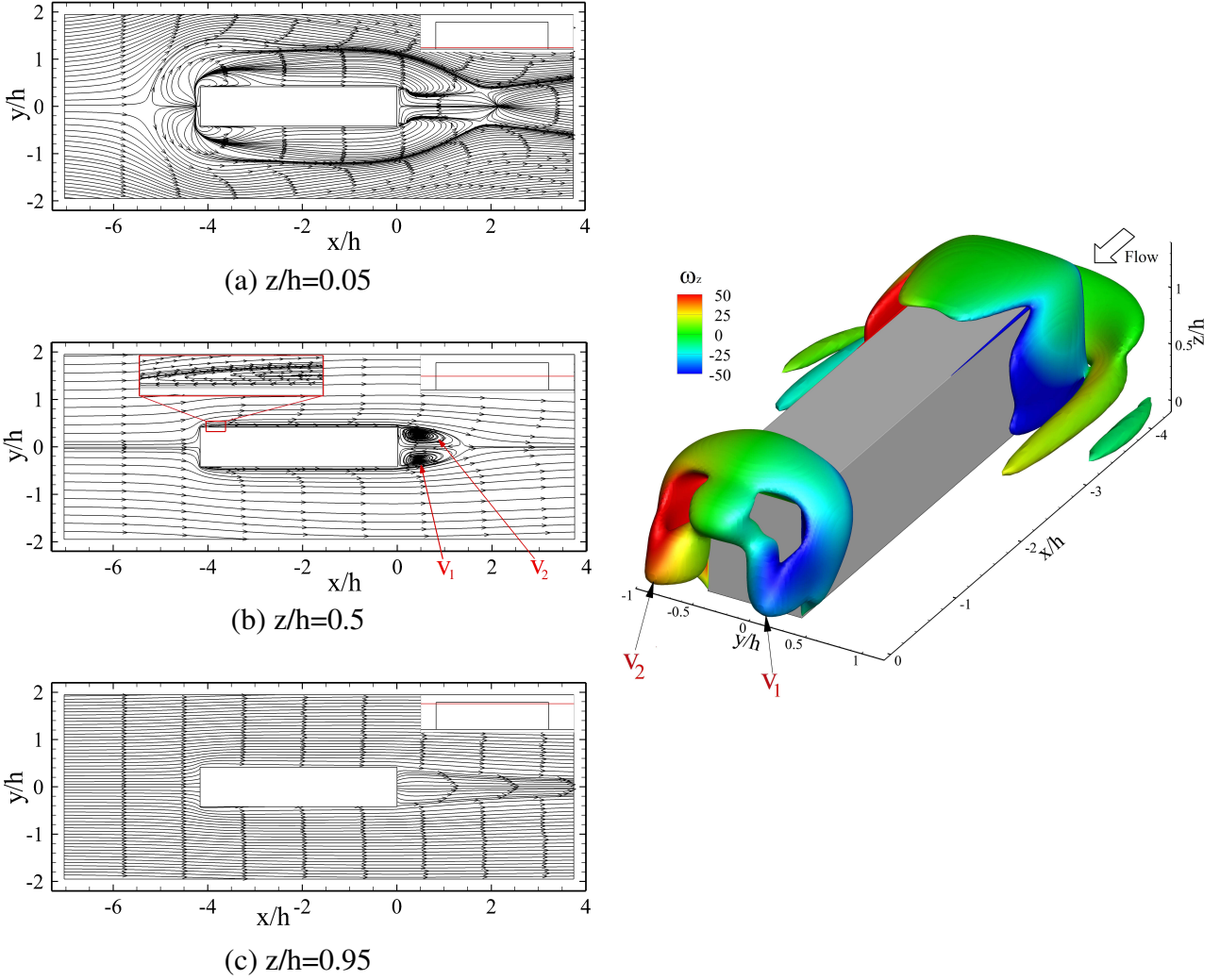
Figure 3.13: Isosurface of $Q = 30$ and top view of the wake structure for the long cylinder at $Re = 250$.

$y/h = 0.3$ using $\alpha = tan^{-1}(v(t)/u(t))$, where α is the streamline angle of curvature. The smaller α for the long rectangular cylinder implies that there is not a significant flow entrainment into the immediate wake (Hemmati et al., 2016a). This wake behavior appears very different for the square cylinder in Figure 3.15a. Here, there is a significantly larger streamline curvature, due to the shorter depth of the cylinder, which implies a stronger freestream flow entrainemnt in the wake region. This leads to the formation of two base vortices in the immediate wake, which are missing for the case of the long-rectangular cylinder. Moreover, streamline of the long-rectangular and square cylinders shows that the length and height of the wake region of the square cylinder

46

(a) y/h=-0.35

(b) y/h=0

(c) y/h=0.35
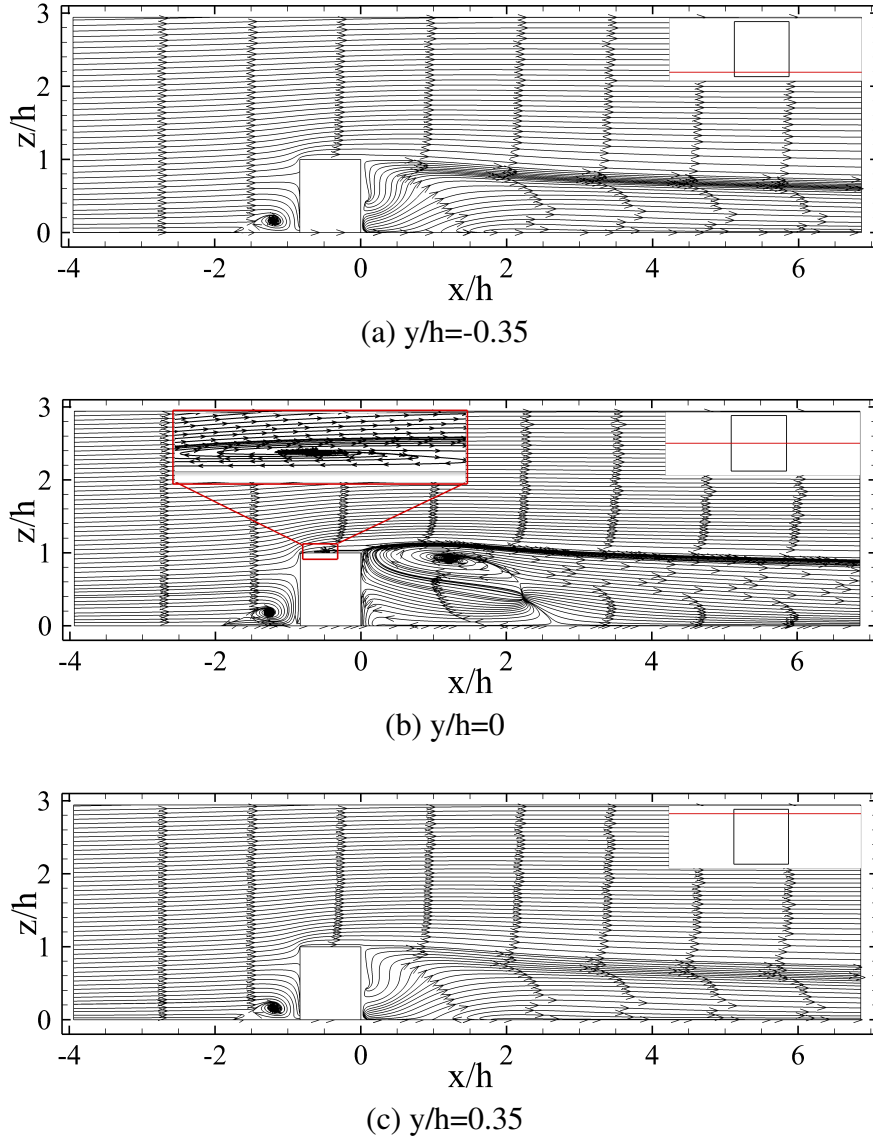
Figure 3.14: The side ($xz-$plane) view of the wake structure of the square cylinder at $Re = 250$.

are greater than the long rectangular cylinder. Particularly, the vortices formed in the wake of the square cylinder extend up to $2h$ downstream in the wake, whereas the extension of these structure for the long-rectangular cylinder is reduced by a factor of 2 (see Figures 3.12b, 3.13b, 3.14b and 3.15b). This trend persists across the flow field in the spanwise ($y-$) and normal ($z-$) directions. The vortex structure in $z-$direction in the middle region of the square cylinder extends to the upper regions, whereas it was constrained to the mid-plane of the longer cylinder. This structure for the long-rectangular cylinder is completely different in the middle and upper regions. This

(a) z/h=0.05

(b) z/h=0

(c) z/h=0.95
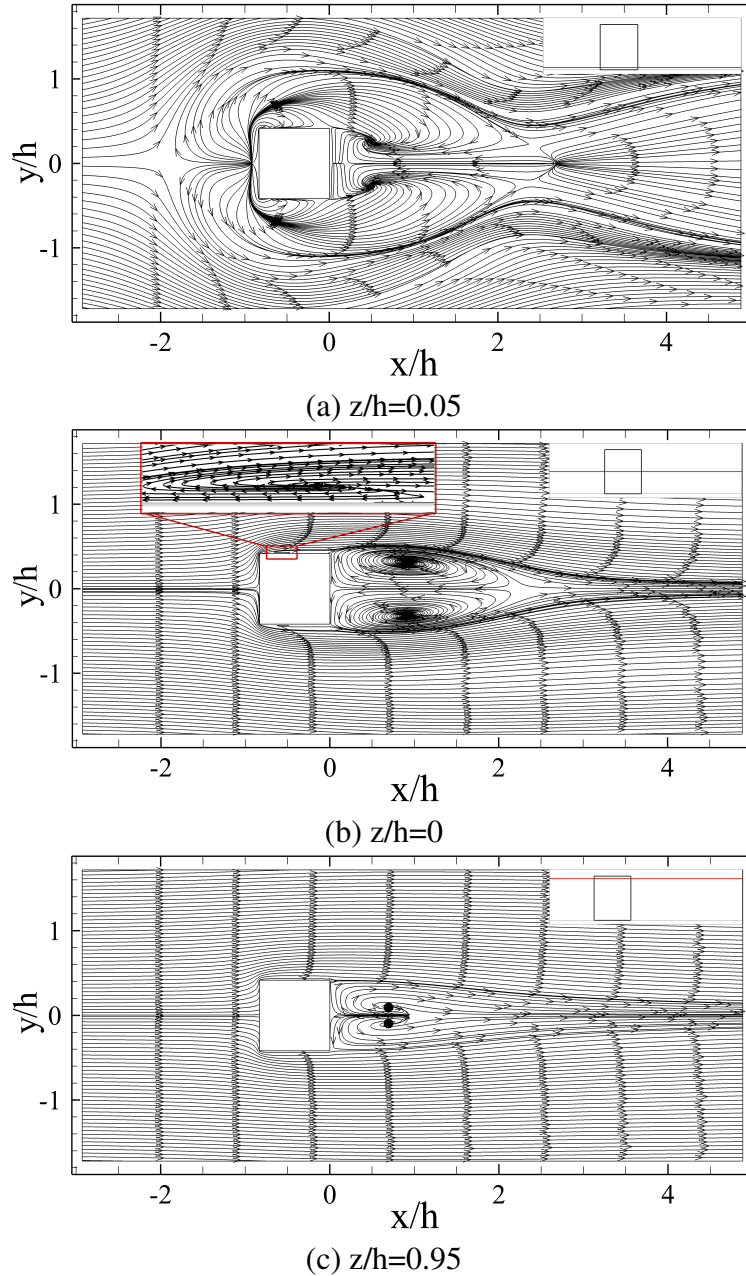
Figure 3.15: The top ($xy-$plane) view of the wake structure of the square cylinder at $Re = 250$.

indicates that the extension of the flow structures in the spanwise direction is inherently related to the strength of the upwash flow. The separation bubble close to the leading edge of the body is highlighted on the middle planes (see Figures 3.14b and 3.15b). This separation bubble does not extend to the outer regions. Furthermore, the length of this structure is not affected by changing the depth ratio. Despite this similarity, there exists a tip structure in the wake, which follows a

different dynamics for long cylinders compared to shorter cylinders at low *Re*. It appears that the wake structures in the case of the square cylinder are dominated by the downwash flow induced by larger (in apparent size) and stronger (in vorticity magnitude) trailing structures, which interact with the horseshoe vortex in the immediate wake. However, the long-rectangular cylinder involves a distinctly smaller (in apparent size) and weaker (in vorticity magnitude) structure formed at the trailing-edge of the cylinder that do not interact with the boundary layer. Thus, the simulated flow appears steady.

Figure 3.16 shows the vorticity contours in the near wake region of the cylinders. The larger magnitudes of spanwise and streamwise components of vorticity in the wake region of the square cylinder can lead to larger streamline curvatures. This provides further evidence of the stronger entrainment in the wake of the square cylinder compared to the long rectangular cylinder. The separated shear layer from the leading edge exhibits a large vorticity magnitude for both cylinders. In the case of the square cylinder, the leading edge separated flow impacts the wake structures through what can be described as flow entrainment. However for the long rectangular cylinder, the reattachment of the flow on the upper and side faces prevents any entrainment mechanism. The presence of counter-rotating vortices in two sides of the cylinder implies that Kàrmàn type vortices are suppressed by the upwash and downwash flow in both cases, due to the small aspect ratio of the cylinders.

For a better understanding of the vortex structures around the body, two-dimensional streamlines along different planes perpendicular to the streamwise direction (cross-sectional planes) are shown in Figure 3.17. Two counter-rotating vortical structures are observed immediately behind the long-rectangular cylinder, which expand as we move farther away from the body. To follow the existing definitions for base vortex structure, these vortices should have an opposite sense of rotation in comparison with tip vortices (Rastan et al., 2017). There is not any evidence of the formation of streamwise tip vortices behind the long-rectangular cylinder, which does not allow for a comparison to the rotational direction of these structures. Thus, it seems that the small aspect-ratio of the considered cylinders leads to the elimination of the streamwise tip vortices in the wake
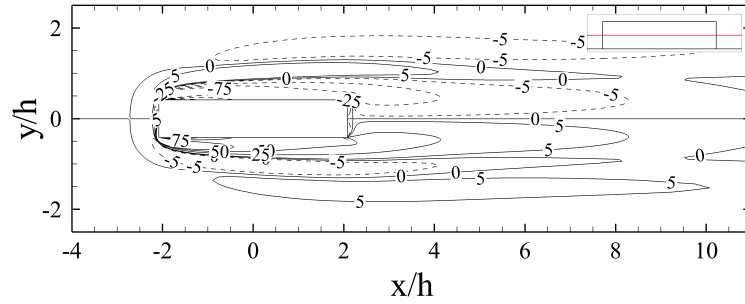
(a) Contour of ω_x
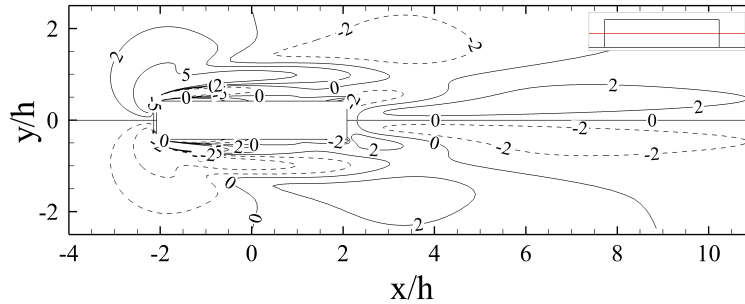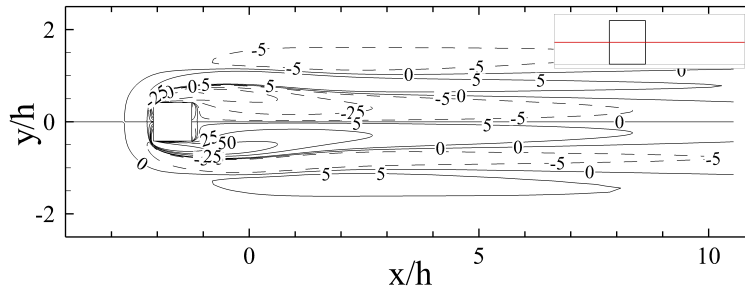
(b) Contour of ω_z
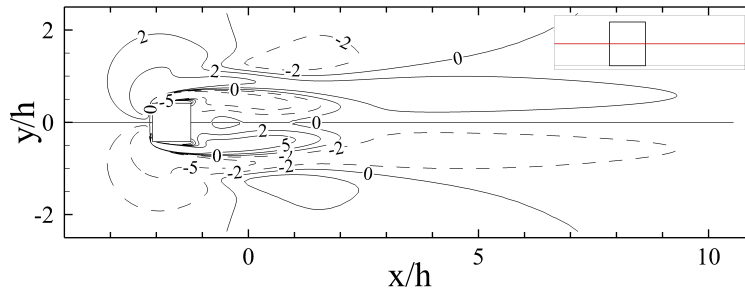
(c) Contour of ω_x

(d) Contour of ω_z

Figure 3.16: The contours of vorticity at the mid-height plane of the (a,b) long-rectangular cylinder and (c,d) square cylinder at $Re = 250$. The dotted lines indicate negative vorticity.

region. These rotational flow transforms into a pair of streamwise vortical structures within $3.85h$ from the cylinder (Figure 3.17b), which quickly grow to the same size as the cylinder height within

(a) x/h=6

(c) x/h=8

(b) x/h=14

(d) x/h=20
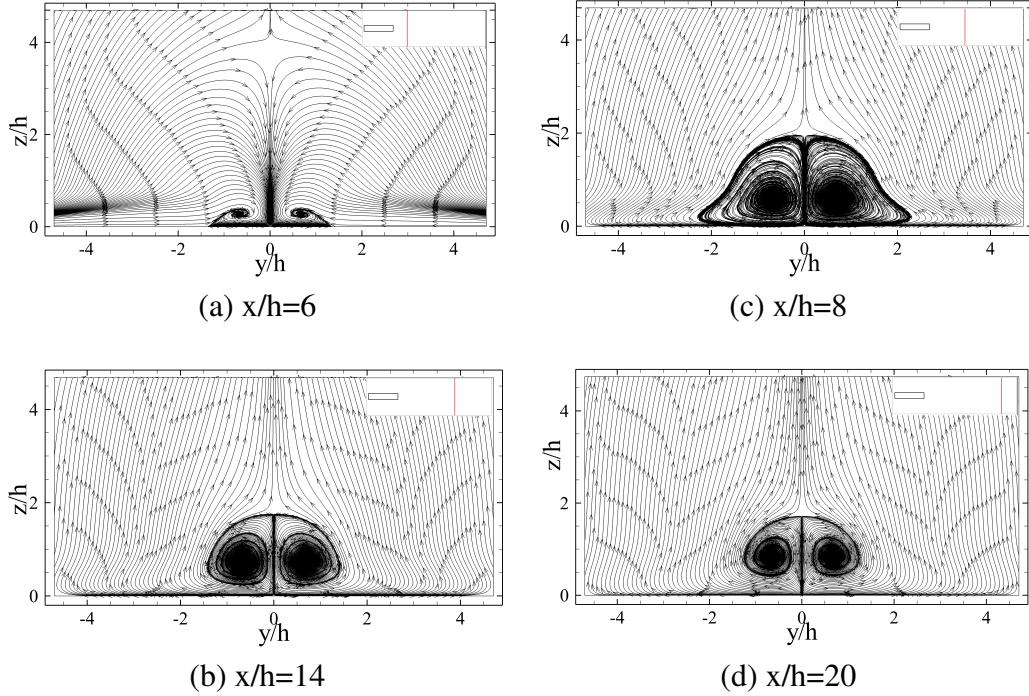
Figure 3.17: Mean streamlines on $zy-$planes at in the wake of the long cylinder at $Re = 250$.

$8h$ downstream (Figure 3.17c). These streamwise vortices appear steady and with minimal diffu-
sion far into the wake, $x/h \geq 20$ (Figure 3.17d).

Figure 3.18 shows the 2D streamlines on $yz-$planes at different streamwise locations in the
wake of the square (short-depth-ratio) cylinder. There is clearly a different streamwise vortex for-
mation mechanism at the rear face of the square cylinder compared to the long-rectangular cylinder
(Figure 3.17). This is mainly due to the large streamline curvatures on the xz-plane that entrain the
fluid into the wake and trailing structures. There are evidence of streamwise base vortical struc-
tures in the immediate wake of the square cylinder, which diffuse rather quickly within $1.2h$ into
the wake. The wake development past this point is very similar to the case of the long-rectangular
cylinder, whereas the structure size is relatively smaller for the square cylinder. However, the main
characteristics of the wake, such as symmetry and steadiness, remain similar. It is also notable
that the former structures in the far wake of the long-rectangular cylinder have the same rotational
direction as the vortical structures close to the leading edge of the body (see V_1 and V_2 in Figure
3.19a). Therefore, they do not follow the common definition of base vortices based on their rota-

51

(a) x/h=4   (c) x/h=8

(b) x/h=14   (d) x/h=20
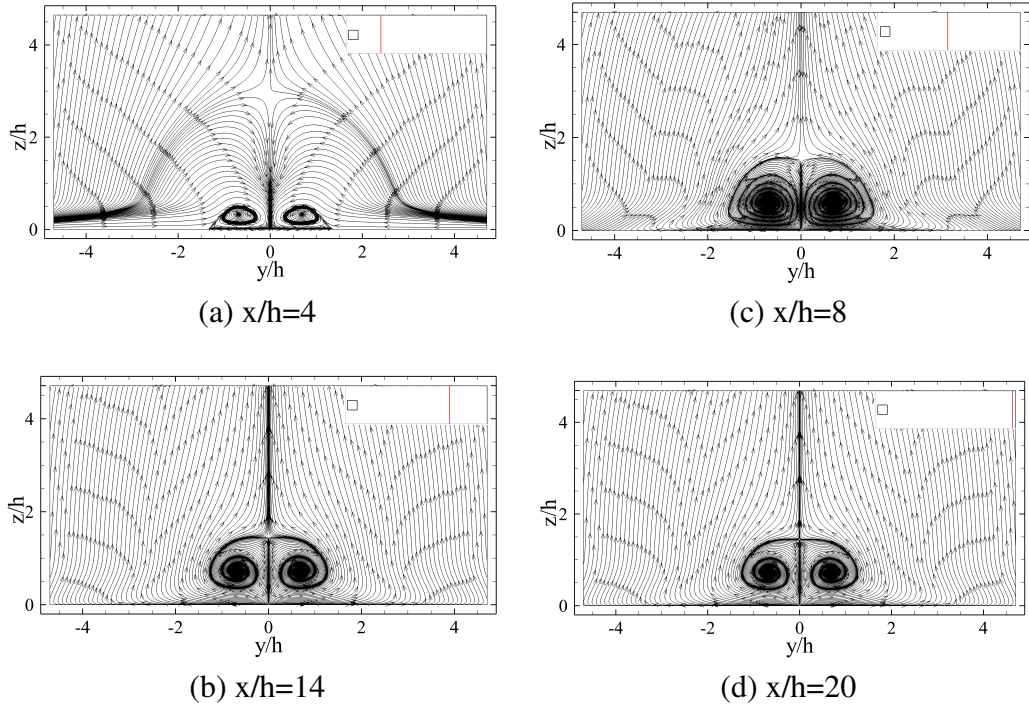
Figure 3.18: The mean streamline plot on cross-sectional ($yz-$) planes at different distances from the square cylinder at $Re = 250$.

tional direction compared to those of the counter rotating vortices close to the leading edge of the cylinder.

Figures 3.19a−b show 2D streamlines on $yz-$planes at different streamwise locations along the long cylinder prior to the wake. These results reveal the formation of a pair of vortex structures on the contact lines of the upper and side faces close to the leading edge of the long cylinder. This structure vanishes before reaching the rear of the cylinder. These structures are not formed on the side faces and close to the leading edge of the square cylinder (Figures 3.19c−d), which are mainly due to the large streamline curvatures that form behind the square cylinder. There exists a similar structure in a very small region close to the rear face of the square cylinder, highlighted as S_1 and S_2 in Figure 3.19d, which does not extend into the wake region.

The differences in the wake of square and long-rectangular cylinders are also apparent from the velocity profiles at different streamwise locations in the wake, as shown in Figure 3.20. In the immediate wake, the two cylinders exhibit differnet flow topologies with the square cylinder wake exhibiting a downwash flow that is reversed by mid-plane of the cylinder. There is also a second
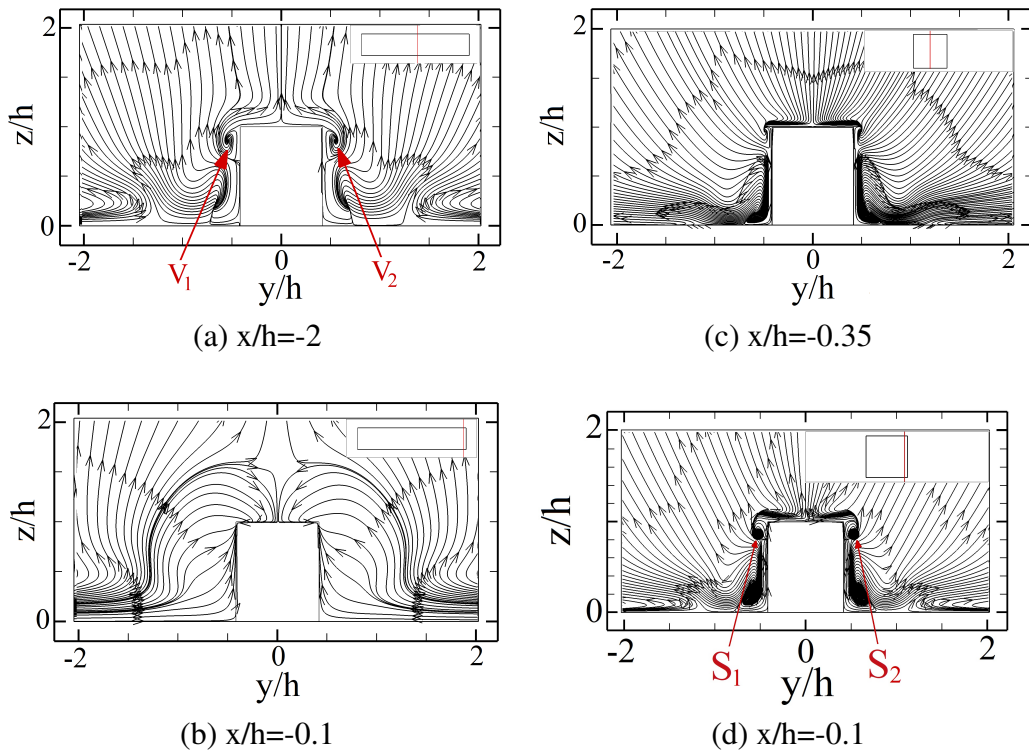
52

Figure 3.19: The mean streamline plots on cross-sectional ($yz-$) planes along the (a, b) long-rectangular and (c, d) square cylinder at $Re = 250$.
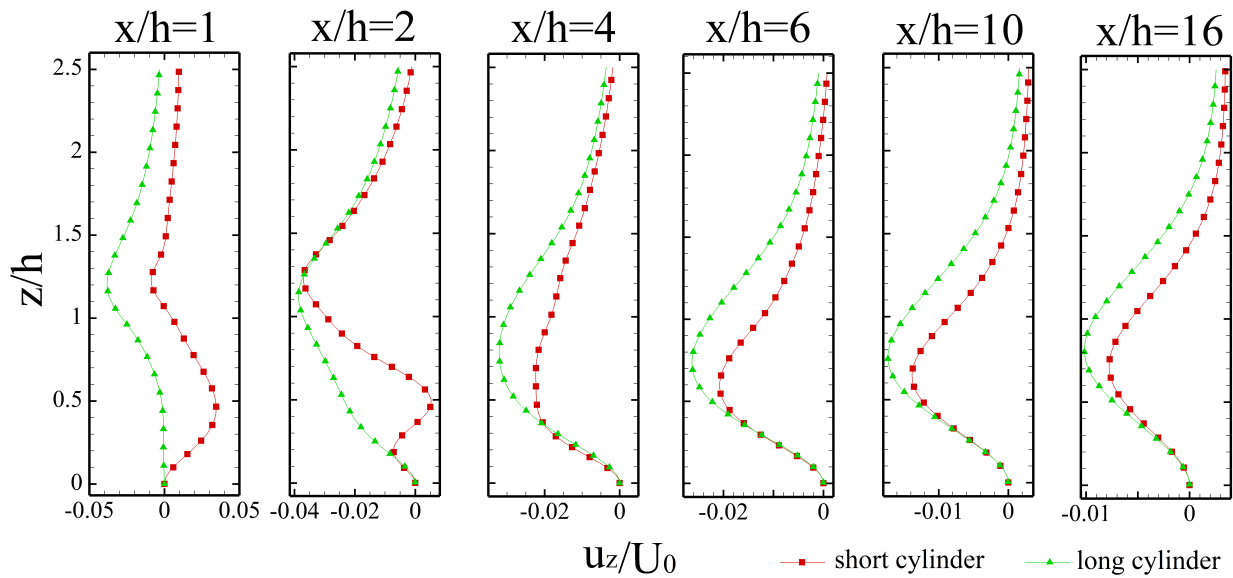

Figure 3.20: The profiles of spanwise velocity (u_z) in the symmetry plane of both cylinders at different distances (identified as 'd') from the rear face of the cylinder at $Re = 250$.

flow reversal at the tip of the cylinder. However, there is only one large upwash flow observed behind the long cylinder corresponding to the main structure that formed in the wake. Also it is important to note that the velocity in the wake of the long-rectangular cylinder tends towards zero after $\approx 1h$ from the top face of the cylinder, whereas the shorter cylinder wake retains the upwash flow past $2h$ above the top face of the cylinder. However, the velocity profile variations are similar in the far wake region of the two cylinders. It is also notable that because of the stronger upwash flow in the wake of the square cylinder, there is a large magnitude of normal velocity compared to the long-rectangular cylinder. Changing the velocity distribution alters the heat and mass transfer, which provides critical information that is useful in the engineering design of small heat sinks and cooling of electronic chips.

3.4.2 Unsteady Wake ($Re = 1000$)

The unsteady transition in the wake of the long-rectangular cylinder is explored at $Re = 1000$. We begin by looking at the iso-surface of $Q-$criterion in Figures 3.21 and 3.22, where the wake of the long-rectangular cylinder appears unsteady. This results in more complex flow structures, wake dynamics and vortex interactions compared to the steady wake of $Re = 250$. Since the unsteady wake of the square (short-depth) cylinder is already studied extensively with available wake models in literature, we here only focus on presenting the wake features of the long cylinder and compare them with those of existing short-cylinder models.

One of the first features identified in the unsteady wake of the large-depth-ratio rectangular cylinder is the presence of a two-part horseshoe structure in front of the cylinder compared to the case of $Re = 250$. The horseshoe structure grows and wraps around the cylinder, and it eventually transitions to an unsteady helical formation with what appears to be vortex-loops that interact with the structures formed on the cylinder sides. Hwang and Yang (2004) reported that changing the Reynolds number from 250 to 1000 for a square cube changes the horseshoe vortex, such that it contains 2 structures. However, they identified the horseshoe vortex around a wall-mounted cube to exhibit a laminar behavior. There also exist separation bubbles on the upper and side faces
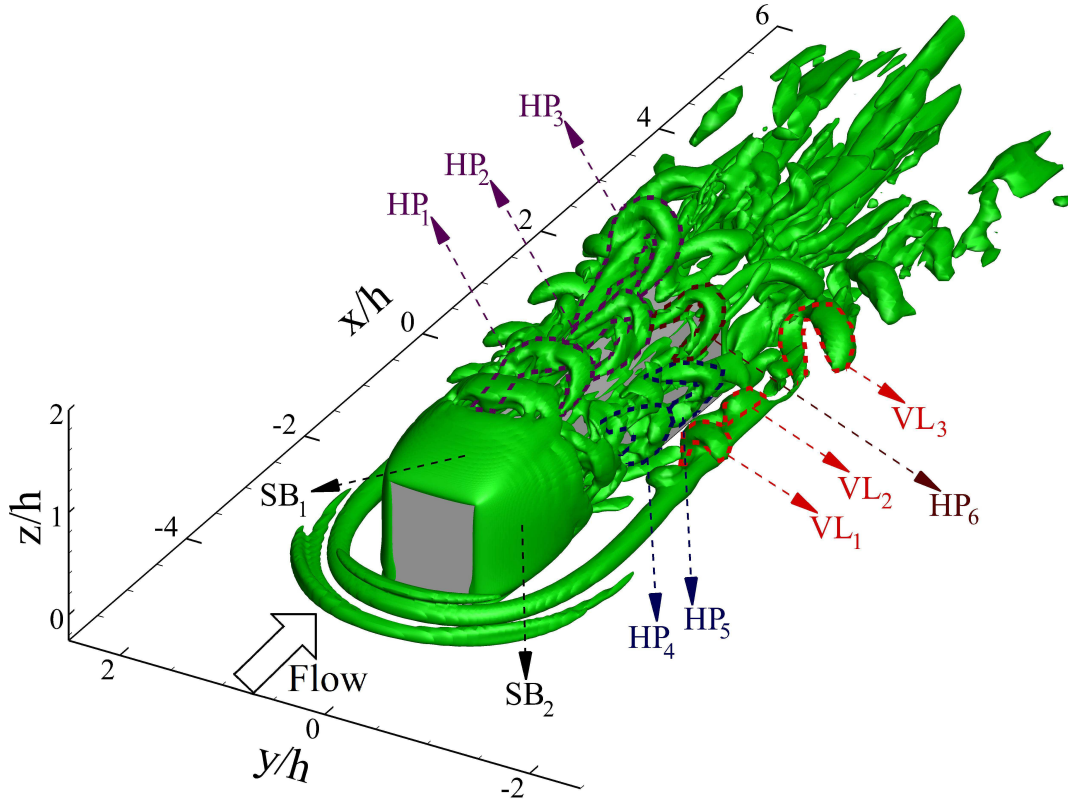
Figure 3.21: Iso-surface of $Q = 2000$ in the wake of a long rectangular cylinder at $Re = 1000$.

of the cylinder (SB_1, SB_2 and SB_3 in Figures 3.21 and 3.22). These transition to hairpin-like structures as they partially detach from the surface of the cylinder. They are carried downstream towards the cylinder trailing edge with their legs still connected to the body, see HP_1 and HP_2 in Figures 3.21 and 3.22. At the trailing edge, these structures distort in the streamwise direction as they detach from the body with no apparent normal movements or normal distortions, see HP_3 in Figures 3.21 and 3.22. There are also similar structures observed on the sides of the cylinder due to the separation of the shear layer on the sides, for example HP_4 and HP_5 in Figures 3.21 and 3.22. These structures have similar spacing at their initial formation to the ones on the top face of the cylinder, which indicates that their formation mechanism may be similar. However, their spacing is shortened along the cylinder length. There is a third type of hairpin-like structure in the wake that we name "oblique hairpins". One leg of these hairpins is connected to the side face, while another leg is connected to the upper face (see HP_6 in Figures 3.21 and 3.22). The origin of the oblique
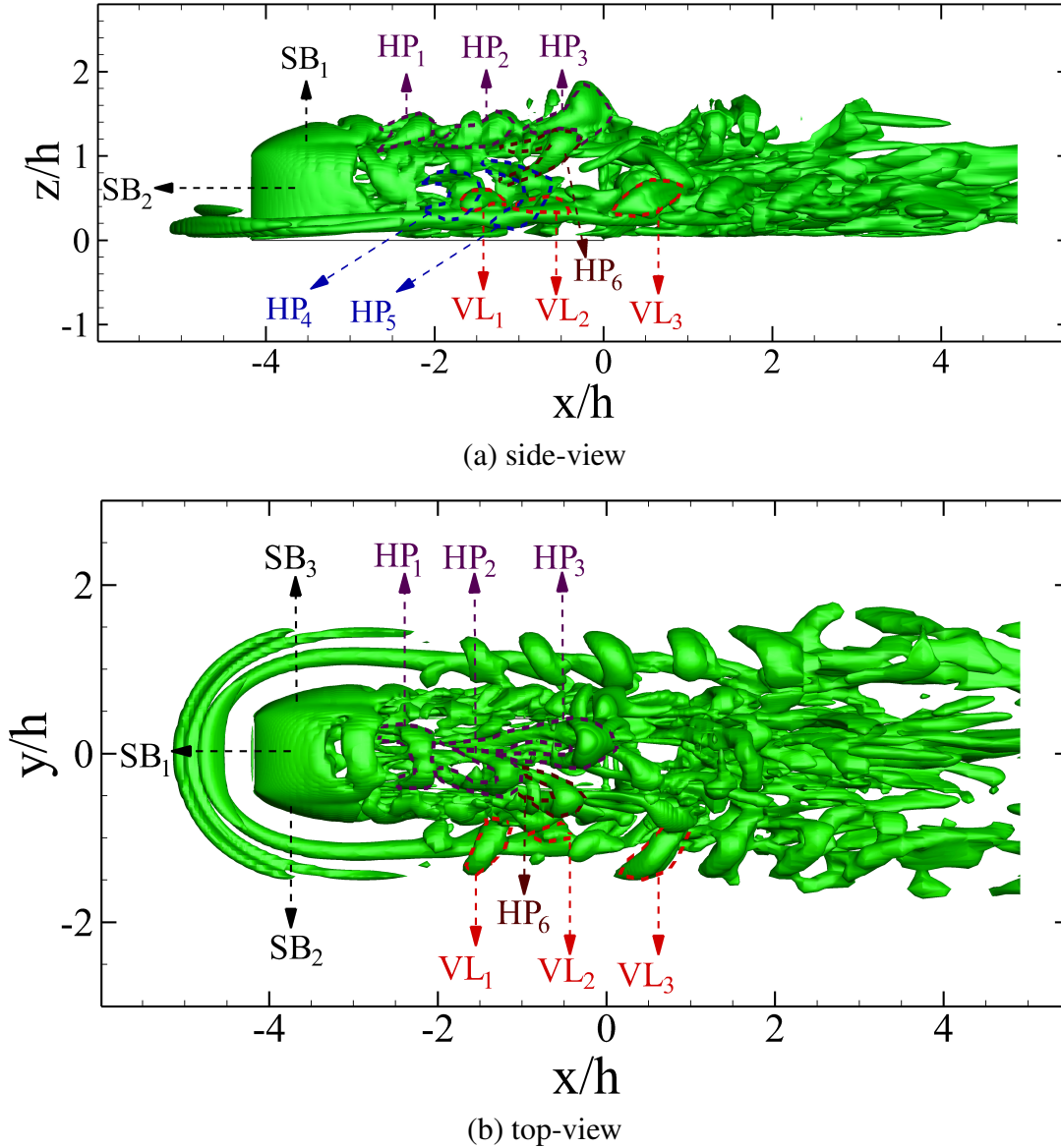
Figure 3.22: Iso-surface of $Q = 2000$ from a (a) top-view and (b) side-view in the wake of a long rectangular (large-depth-ratio) cylinder at $Re = 1000$.

hairpins can be attributed to the interaction between side and top shear layers formed on adjacent faces of the cylinder. The oblique hairpins did not exhibit a prominent frequency, and they did not appear, by inspection of the wake, to maintain a particular spacing. These types of structures are not observed for the square cylinder due to the bending of the shear layer starting at the cylinder leading-edge (Wang and Zhou, 2009). The spacing between and the frequency of hairpin-like structures on top of the cylinder is different (longer spacing by a factor of $\approx 4h$) than that of the

(a) $t = t_0$

(b) $t = t_0 + \tau$

(c) $t = t_0 + 2\tau$
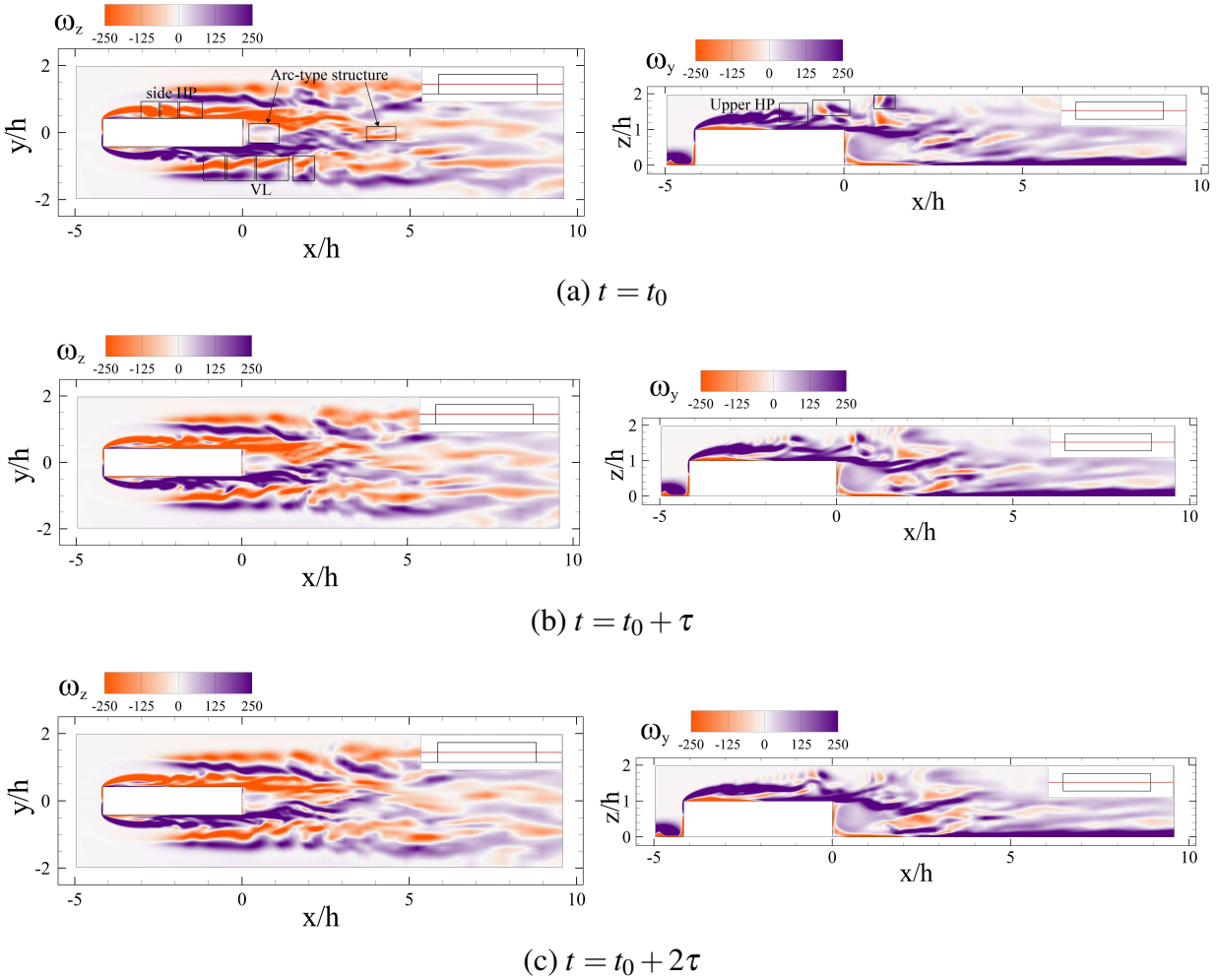
Figure 3.23: Contours of instantaneous vorticity in spanwise ($y-$) and normal ($z-$) directions at mid-planes ($z/h = 0.5$ and $y/h = 0$) of the long cylinder at $Re = 1000$ during three consecutive instances of the flow. Here, $\tau = 0.01U_\infty/h$.

vortex loops formed by the unsteadiness of horseshoe structures on the sides. This implies that the unsteady transitioning of the horseshoe vortex is not inherently related to the unsteadiness of top leading edge structures that form top-side hairpin-like vortices.

The side hairpin-like structures appear to begin interacting with horseshoe vortex loops fairly early on after their formation, for example VL_1 and HP_4 in Figures 3.21 and 3.22. This indicates that the onset of transition in horseshoe structures is related to the separation of shear layers on the side face. However, the latter structures maintain their coherence downstream the trailing edge of the cylinder, whereas the side hairpin-like structures lose their coherence relatively early on, prior

57

to reaching the trailing edge. This indicates that there is not a strong interaction between the two structures. Rather there exists an induced flow by the horseshoe vortex loops (helical structure) that dominates this part of the wake. This leads to elongation and distortion of the side hairpin-like structures. Moreover, visualizing the distribution of instantaneous vorticity in spanwise and normal directions in Figure 3.23 reveals the presence of a structure that has the characteristics of a typical arc-type structure in the wake. However, the wake complexity with the presence of hairpin like structures prevents an apparent identification of an arc-type structure using isosurfaces in the unsteady wake. Instead, we will rely on known effects of such structures to recognize their presence. Despite the ambiguity on the nature of the arc-type structure formed here, the mean flow characteristics obtained from the isosurfaces of the mean wake, not shown here for brevity, does not point at the near wake structures recently introduced by da Silva et al. (2020).

The hairpin-like structures on the side and top faces of the cylinder lose their coherence at approximately $x/h = -1$ and $x/h = 2$, respectively, while the horseshoe vortex-loops (helical formation) lose their coherence farther downstream at approximately $x/h = 7$. This complex wake behavior is also apparent from 2D streamlines of Figure 3.24, where the horseshoe structures dominate the side wake. Horseshoe structures grow substantially by mid-point of the cylinder depth, while there is no substantial effect observed from the hairpin-like structures. At the front face of the cylinder (Figure 3.24b), there are two small secondary vortices (identified as SV_1 and SV_2) that appear closer to the cylinder lower side face. These structures are quickly absorbed by the large horseshoe vortex loops farther downstream. This is the only obvious indicator of the base vortex in the wake. Farther downstream at the cylinder trailing edge, the horseshoe vortex loops (secondary component of the helical formation) have grown to half of the cylinder height in diameter.

To achieve a better understanding of the unsteady wake dynamics, we explore the power-spectral-density (PSD) of velocity and pressure using 115 different probes in the domain at $x/h = -3.7$, -2, -0.5, 0.5, 5 and 10, $y/h = -2.5$, -1.6, 0, 0.5, 1, 1.25, 1.6 and 2.5 and $z/h = 0.5$, 1 and 1.5 over time. To reduce the unwelcome effect of noise, each signal is divided into eight segments with 50% overlap, and PSD values are averaged using these segments. Looking at the frequency

(a) $x/h = -4$

(b) $x/h = -2$

(c) $x/h = -0.1$
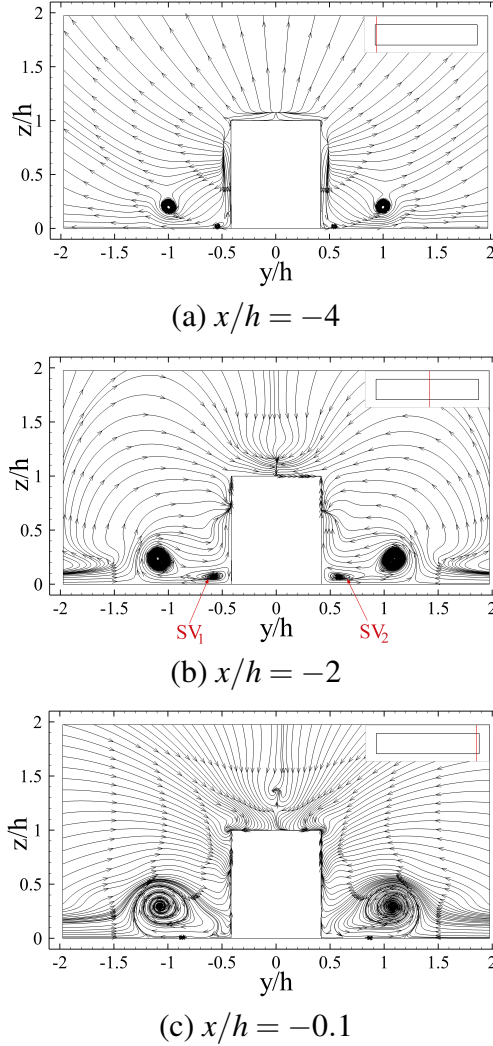
Figure 3.24: 2D streamlines on the three different streamwise planes along the cylinder depth at $Re = 1000$.

signatures in Figure 3.25, there are multiple frequencies identified in the velocity field. The velocity fluctuations are shown at four locations in the wake to capture the dominant frequencies associated with the horseshoe, side and top hairpin-like vortex structures, as well as typical arc-type structure behind the cylinder. There is a single dominant peak frequency identified in Figure 3.25a at Strouhal number $St_{hp1} = 0.64$, which is associated with the hairpin-like structures formed on the side faces of the cylinder. Here, Strouhal number is defined as $St = fh/U_\infty$ with f being the frequency. At the top of the cylinder (Figure 3.25b), the dominant frequency due to the separated hairpin-like structure is apparent at $St_{hp2} = 0.38$. The difference between the dominant frequency
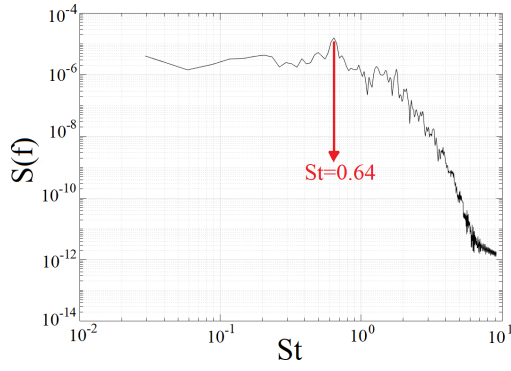
(a) Probe A (spanwise component of velocity)
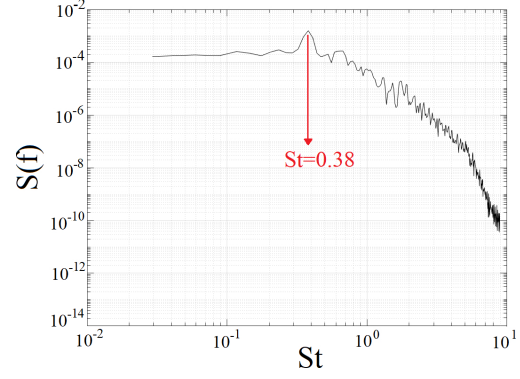
(b)Probe B (streamwise component of velocity)
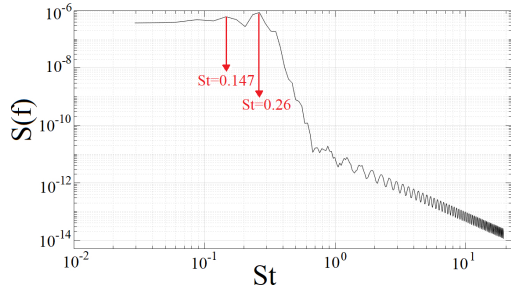
(c) Probe C (spanwise component of velocity)
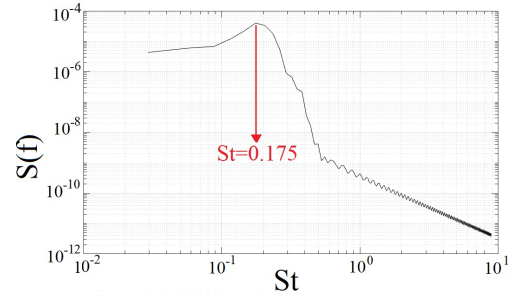
(d)Probe D (spanwise component of velocity)

Figure 3.25: The power density spectrum of velocity fluctuations at three locations in the wake of the long-rectangular cylinder at $Re = 1000$. The coordinate of the probes are: $A : w(-0.5, 1.0, 1.0)$, $B : u(0.5, 0, 1.5)$, $C : w(5.0, 2.5, 0.5)$ and $D : w(10, 0, 1.5)$.

of the side and top hairpin-like structures, considering their similar formation mechanisms from the detached shear layers formed on the leading edges of the cylinder, implies that the side-structures are effected almost immediately after their detachment by the horseshoe vortex. There are two different dominant peak frequencies identified in Figure 3.25c at $St_{H1} = 0.26$ and $St_{H2} = 0.147$, which are associated with the horseshoe vortex loops formed on the sides of the cylinder. Tracking structures using the instantaneous vorticity contours in Figure 3.23 reveals that the dominant frequency of $St_{H1} = 0.26$ is due to the velocity fluctuations created by the main component of the horseshoe vortex. We also associate the lower peak frequency ($St_{H1} = 0.147$) with the primary component of the helical structure (frequency of swirl) formed by the unsteadiness of the horseshoe vortex. A combination of the tracking of structures in the contour plots of Figure 3.23 and evaluating the PSD analysis at $x/h = 2.5, 5$ and 10 and $y/h = 1$ (not shown here for brevity) reveal that the $St_a = 0.175$ is associated with the arc-type structures in the wake. In fact, the frequency

60

associated with the arc-type structure is the only peak captured in far downstream, where no other peak frequencies are observed. Thus, it is apparent that at $x/h \geq 10$, the fluctuations due to the arc-type structure dominant the far wake. Closer to the ground, however (not shown here for brevity), we identify a second weaker peak in the PSD diagrams at $St = 0.26$, which is associated with the remaining effect of the helical structure that spawn out of the horseshoe vortex.

These results suggests that there are three distinct unsteady wake mechanisms due to the horseshoe, arc-type and hairpin-like structures. Conversely, Wang and Zhou (2009) identified a single Strohaul number of $St = 0.11$ for the case of a square (short-depth) cylinder, and concluded that there is only one structure in the wake region of the cylinder. Although similar structures are observed for the shorter-cylinder, as described by the model of Wang and Zhou (2009), the size of side structures for longer cylinders is significantly smaller than the horseshoe vortex loops, and the base vortex is also absorbed by the horseshoe structure. This results in a lack of strong downwash and upwash effects observed for the short cylinders. Instead, there appears to be a large streamwise distortion observed on hairpin-structures that are referred to as tip vortices by Wang and Zhou (2009).

The two-dimensional time-averaged streamline plots in Figure 3.26 show mean streamwise structures in the near and far wake at $Re = 1000$. Contrary to the wake at $Re = 250$, the horseshoe vortex extended to the near wake region (see Figures 3.26a and 3.26b). The formation of the tip vortices in the near wake region (TV_1 and TV_2 in Figure 3.26a) is another important difference in the wake of the long cylinder following its unsteady transition. Separated shear layer from the upper junction of the leading edge produces downwash flow in the near wake region, while the horseshoe vortex and reversed flow in the wake leads to the upwash induced flow. As shown in Figure 3.27, the strength of the mean downwash flow at $Re = 1000$ is greater than the flow at $Re = 250$ (see Figure 3.11). Indeed, by increasing the Reynolds number, the length of the separation bubble on the upper face increases. Hence, the separated shear layer from the leading edge creates a more substantial downwash effect. Thus, the tip vortex formation appears related to the strength of downwash flow, not the aspect ratio of the rectangular cylinder.

(a) $x/h = 0.5$

(b) $x/h = 2.0$

(c) $x/h = 4.0$

(d) $x/h = 10.0$
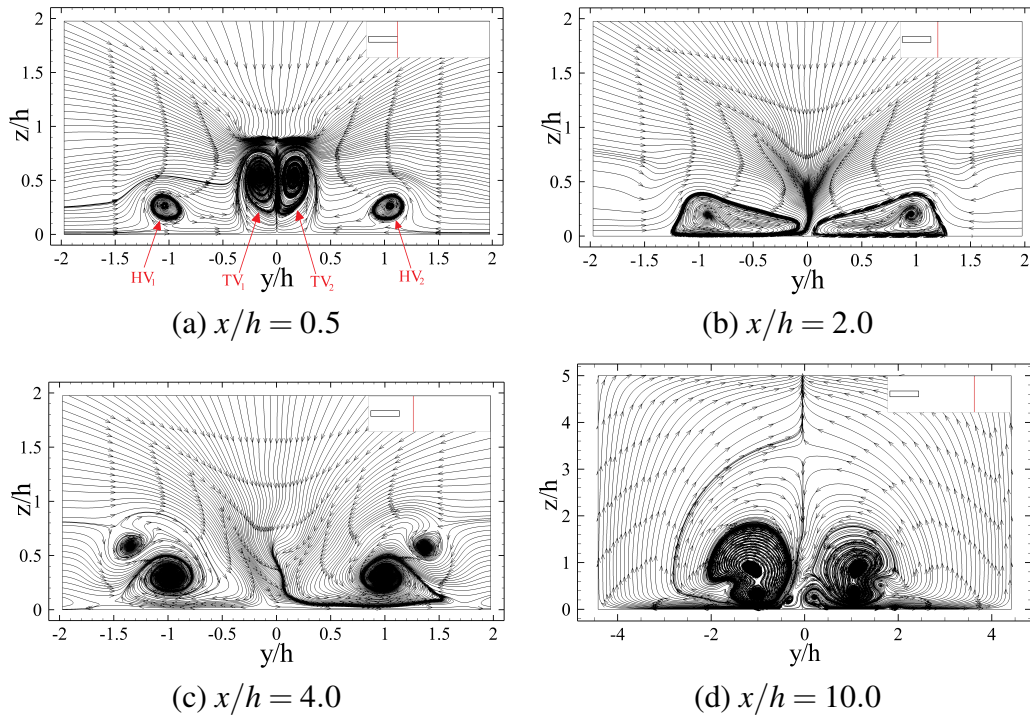
Figure 3.26: mean 2D streamlines on the different streamwise planes along the wake region of the long cylinder at $Re = 1000$.

(a) $y/h = -0.4$

(b) $y/h = 0$

(c) $y/h = 0.4$
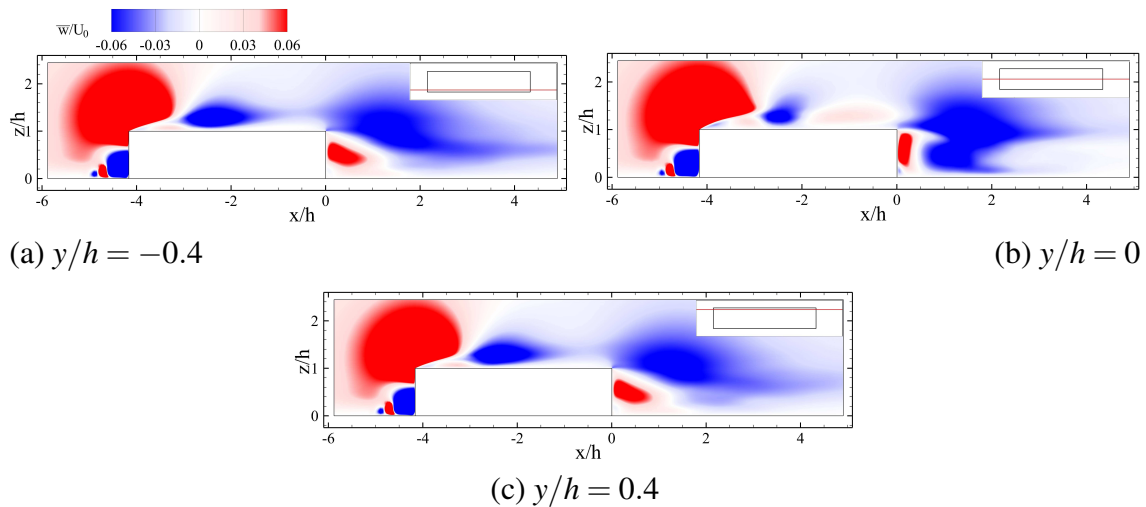
Figure 3.27: Contours of mean spanwise velocity at different planes along the long rectangular cylinder and an arbitrary time for $Re = 1000$.

(a) $z/h = 0.05$

(d) $y/h = -0.4$

(b) $z/h = 0.5$

(e) $y/h = 0$

(c) $z/h = 0.95$

(f) $y/h = 0.4$
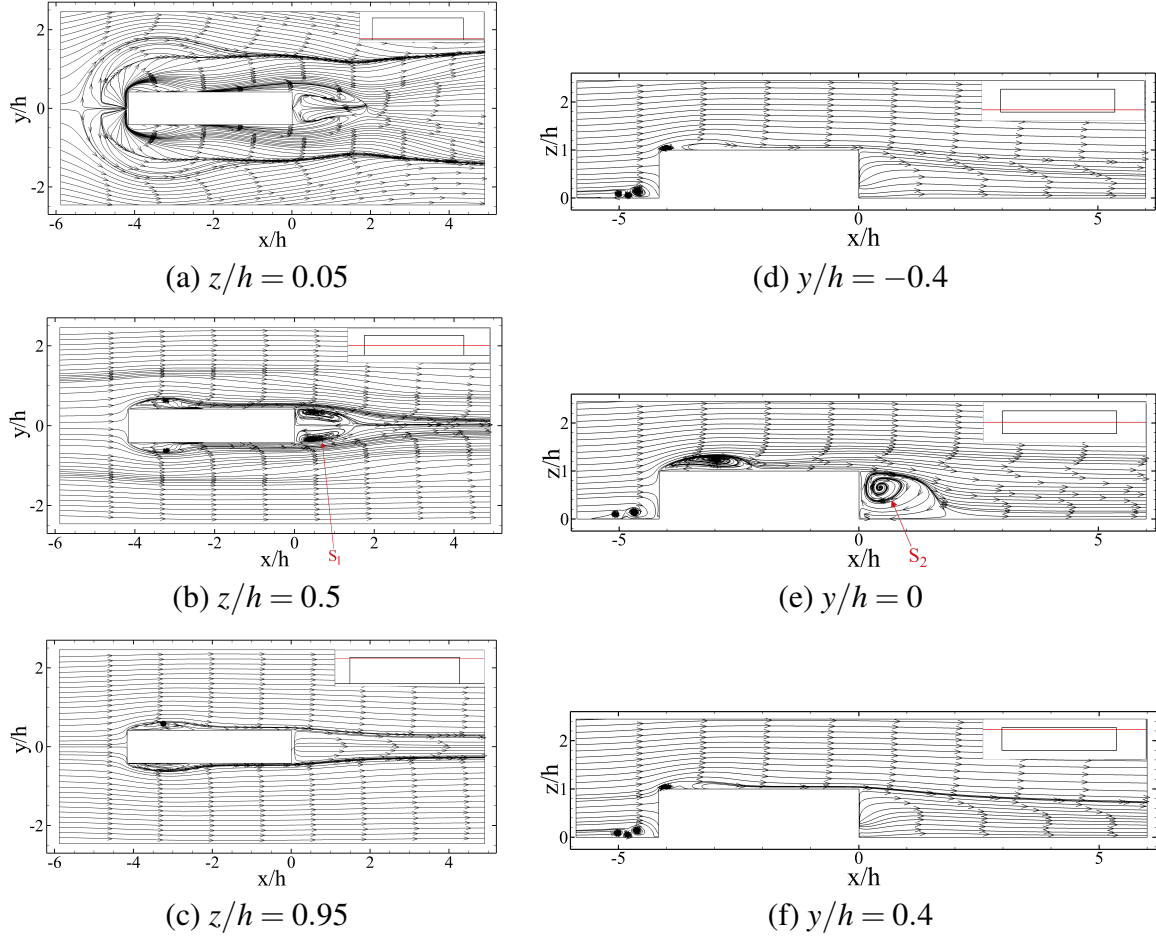
Figure 3.28: Contours time averaged stream lines in $xz-$ and $xy-$ planes for the long cylinder at $Re = 1000$.

To introduce a model for the flow structures around a long rectangular cylinder, the time averaged streamlines around the body are shown in Figure 3.28. There exists a counter-rotating structure in Figure 3.28b, identified as S_1. There is also a rotating structure in Figure 3.28e, identified as S_2, which coincides with the formation of a tip vortex, as discussed earlier. The combination of these observations imply that there is an arc-type structure in the near wake region, which was previously observed for tall (large aspect-ratio) square cylinders by Wang and Zhou (2009). Furthermore, only one dominant frequency corresponding to the wake structures can be found in Figure 3.25. Thus, there is an arc-type structure in the near wake region similar to the case of the short depth ratio cylinder. In the model of Wang and Zhou (2009), this structure is directly connected to the separated shear layer from the leading edge. Conversely, since the separated shear

63
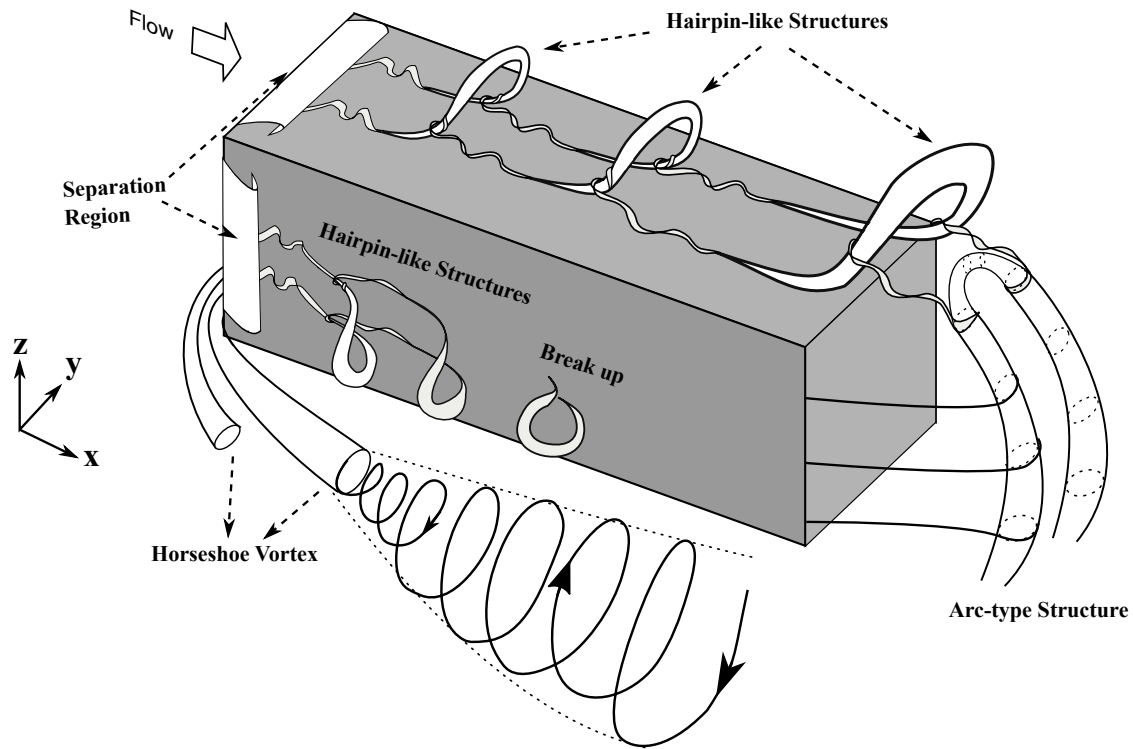
Figure 3.29: New model for the vortex structures of a long rectangular cylinder

layer reattaches to the cylinder faces, the arc-type structure is connected to the boundary layer on the upper and side faces of the long rectangular cylinder. This leads to the formation of a number of wake features unique to the long (large-depth-ratio) cylinder that were not observed in the shorter cylinder model of Wang and Zhou (2009). These include the horseshoe vortex loops that dominate the near wake, the separated shear layer folding behind the body, and the formation of top and side hairpin-like structures. Thus, we introduce a new model for the unsteady wake of a large-depth-ratio rectangular cylinder at low Reynolds numbers in Figure 3.29. This model embodies all the observations related to the wake analysis and vortex interactions discussed thus far. It outlines the presence of at least three major unsteady wake mechanisms around and behind the cylinder.

3.5 Conclusion

A Large Eddy Simulation is carried out for the flow around two wall-mounted rectangular cylinders with the depth-ratios of 0.83 and 4.17 at Reynolds number of 250 and 1000. The wake

dynamics are analyzed extensively for both shapes and Reynolds numbers to identify the effect of large-depth-ratio on steady and unsteady wakes of the cylinder. The wake descriptions identify significant variations in the wake topology between the two cylinders, which is attributed to the large-depth-ratio effects. At a lower Reynolds number, the simulated flow appears steady for both cylinders due to the small aspect-ratio, which is consistent with existing observations.

The wake structures formed behind the long-rectangular cylinder are not connected to the leading edge separated shear layer, which is contrary to the case of square cylinders. Therefore, the distribution of the critical points around the two cylinders are different. The strength of the upwash flow in the wake region of the square cylinder is higher than the long-rectangular cylinder. This leads to different sizes of the recirculation region due to the large differences in their depth-ratios. Furthermore, the distribution of downwash flow from the tip region is different for the two cases.

As a result of flow entrainment from the leading edge separated shear layer, the streamwise structures of the near wake region change with the large-depth-ratio. Moreover, there exists some streamwise structures close to the leading edge of the long rectangular cylinder that do not appear in the wake of the square cylinder. This difference is mainly attributed to the large streamline curvatures in front of the cylinder with a large-depth-ratio. However, a similar structure close to the trailing edge of the short cylinder is observed, where there is evidence of a large streamline curvature, larger vorticity magnitudes, and thus, more significant entrainment effects. This is mainly attributed to the smaller depth-ratio of the square cylinder, which facilitates the merge of structures in the rear and their interaction with the horseshoe structure. The latter is apparent from the two peaks observed in the profiles of normal velocity above the square cylinder compared to the single peak that is identified in the wake region of the long-rectangular cylinder. These are further evidence that point at a more significant interaction between the horseshoe and wake structures for the square cylinder, which appears to diffuse for the larger depth-ratio case of the long rectangular cylinder.

Increasing the Reynolds number from 250 to 1000 transforms the flow into an unsteady wake. The length of the separation bubble on the upper and side faces of the long rectangular cylinder in-

creases by increasing the Reynolds number. Hairpin-like vortices are formed due to the detachment of the shear layer at the leading edges of the cylinder. The horseshoe vortex grows substantially as it transitions to a helical formation, most likely due to the induced instability associated with the formation of hair-pin structures at the side face of the cylinder. The interaction of the unsteady horseshoe vortex (helical formation) with the side-hairpins suppresses the latter prior to the trailing edge of the cylinder. This enables uninterrupted growth of the helical formation, the effects of which remain visible in the far downstream regions of the wake. There also exists an arc-type structure in the wake that dominates the flow even at far downstream locations, at which only the frequency corresponding to this structure remains apparent. A wake model is presented that extends the existing models for wall-mounted cylinders by incorporating distinct mechanisms that are observed due to the large-depth-ratio of the long cylinder. The model incorporates three distinct unsteady wake mechanisms that dominate the near wake region: horseshoe vortex loops (helical formation), arc-type structure, and hairpin-like structures. Given the strength and size of the helical formations, it is expected that they play a critical role in unsteady transition of the wake at lower Reynolds numbers and different yaw angles.

Chapter 4

EFFECT OF INCIDENCE (YAW) ANGLE

4.1   Introduction

The unsteady wake of a wall-mounted rectangular cylinder at large incidence (yaw) angles is inves-tigated using Large Eddy Simulations at Reynolds numbers of 250. The incident angles considered ranged between $0°$ to $45°$ at $5°$ increments. The results in this chapter provides insight into how the the wake topology, and temporal evolution changes at larger incident angles. Due to the severity of asymmetry introduced to the wake by the large depth-ratio of the cylinder at a large yaw angle, the wake topology is expected to be altered substantially from that of square cylinders and cubes. Furthermore, the characteristic length scales are not expected to remain the same as short (small depth-ratio) bodies. This chapter addresses the second objective of the thesis on characterizing the effect of incident angle on the wake topology. The results are also a major aspect of the novelty of this work. This chapter is structured such that a thorough review of relevant literature is presented in Section 4.2 followed by a detailed description of the methodology and numerical setup in Sec-tion 4.3. The main results and discussions are included in Section 4.4, which is followed by the summary of conclusions in Section 4.5.

4.2 Background

Coherent wake structures have been the focus of researchers since the pioneering work of von Kàr-
màn (1910). This is partly due to their extensive industrial applications, for example to improve
the design of vehicles, reduce the noise of turbines and increase energy efficiency of buildings.
In particular at low Reynolds numbers, understanding the flow around wall mounted cylinders fa-
cilitates the optimization of micro-heat exchangers, cooling systems for electronic devices(Rastan
et al., 2017), and three-dimensional implications of roughness elements in pipes. Recent develop-
ments have revealed that existing experimental and numerical studies do not provide a thorough
description of the flow in the detached flow region of two-dimensional (2D) cylinders (Cimarelli
et al., 2018). Furthermore, interaction between the boundary layer and tip downwash flow behind
a wall-mounted cylinder generates a more complex wake compared to that of 2D cylinders. How-
ever, there are no comprehensive studies that characterize the wake behind long (large depth-ratio)
cylinders, especially at a range of large incident angles.

Identifying coherent structures in the wake of wall-mounted cylinders constitute a classic prob-
lem in fluid mechanics, which started with the work of Taneda (1952). Using a previously devel-
oped model for a wall-mounted circular cylinder, Wang et al. (2004) proposed their first wake
model for a wall-mounted square cylinder. Later on, Wang and Zhou (2009) modified the model
to develop a more extensive vortex model based on their detailed experimental studies. The latter
model identified the existence of a single arch-like structure in the near wake that inherently con-
nect spanwise, tip and base vortices regardless of the aspect ratio of the prism. They also reported
that both asymmetric and symmetric vortex shedding happens simultaneously, but the probability
of asymmetrically arranged structures is higher at the middle height of the body. Most recently,
da Silva et al. (2020) suggested that there are various mean structures with different origins in the
wake of a wall-mounted square (small-depth-ratio) cylinder of aspect ratio $AR = 3$ at Reynolds
number of 500, which is contrary to the model of Wang and Zhou (2009). More specifically,
da Silva et al. (2020) showed that structures on the upper face of the cylinder and tip vortices are
formed because of three-dimensional deflection of the separated flow from the side leading edges
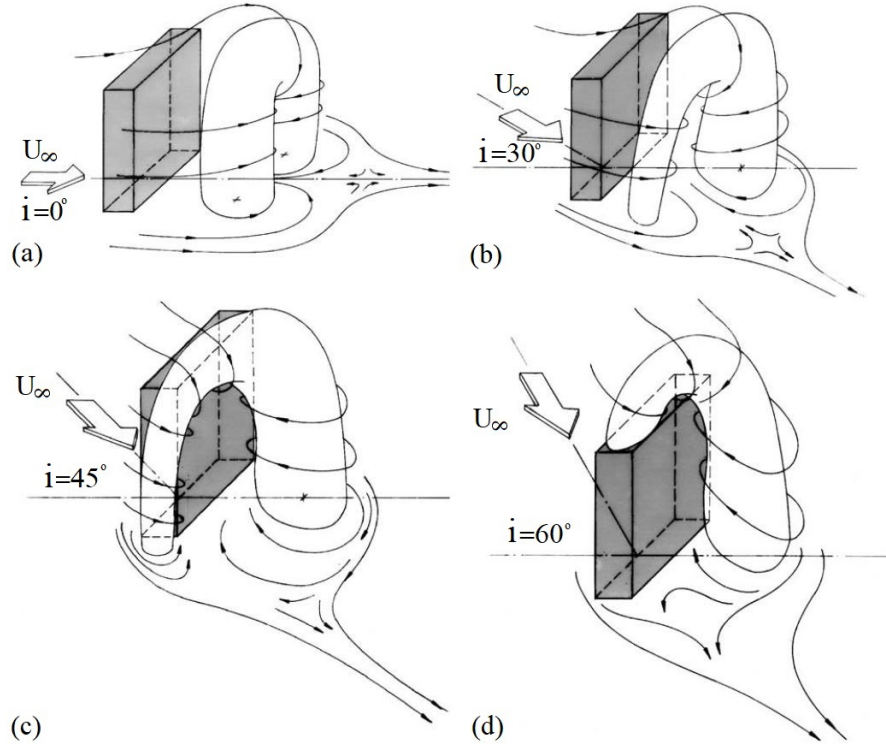
Figure 4.1: The Becker et al. (2002) wake model for a wall-mounted rectangular cylinders at different incident angles.

of the cylinder. Moreover, they identified a new spanwise vortex structure that is formed by folding of the separated shear layer from the free end leading edge of the cylinder. This structure was determined to have a different origin from the so-called legs of the arc-type structure formed by the separated flow from the side face leading edges.

Castro and Robins (1977) carried out an early study of the wake of a cube placed in a uniform atmospheric boundary layer at an incident angle of $i = 45°$. Their results indicated that the effect of downwash flow on the near-wake region is strengthened at $i = 45°$, compared to a horizontally oriented cube ($i = 90°$). Later on, Sakamoto (1985) determined that the force coefficients and Strouhal number corresponding to fluctuations in the wake are highly dependent on the incident angle of surface mounted rectangular prisms at a range of Reynolds numbers ($Re = 4.4 \times 10^3 - 1.17 \times 10^4$). This observation was attributed to the steady reattachment of separated flow to one side of the prism. Furthermore, a critical incident angle was identified, at which the drag coefficient was minimum, and the Strouhal number of lift fluctuations was maximum. By performing Oil Flow

69

Visualization and smoke visualization techniques at $Re = 2 \times 10^6$, Becker et al. (2002) extended the wake structure model of a rectangular cylinder proposed by Martinuzzi (1982) at larger incident angles. By capturing the position of the focal points in the wake of the wall-mounted cylinder, Becker et al. (2002) identified that the location of legs of the arc-type structure changes at different incident angles. As shown in Figure 4.1, the leg of the arc-type structure forms either behind the cylinder, close to the side face of the cylinder, or on the top face of the cylinder depending on the incident angle of the body relative to the free stream. More recently, experimental studies of Schewe (2013) identified major differences in how Reynolds number impacts force and moment variations at different incident angles for a two-dimensional rectangular cylinder with an aspect ratio of 5. It was reported that for an incident angle of zero (i.e., long side of the body is parallel to the streamwise direction), the base pressure and moment coefficients as well as the lift and drag forces are highly dependent on Reynolds number. On the other hand, there were no apparent effect due to Reynolds number at an incident angle of $90°$. The main difference between these two cases was the presence of separation bubbles on side surfaces of the cylinder at the smaller incident angle. Schewe (2013) also determined that shape of the separation bubble may be responsible for such variations since the characteristics of the separation bubble greatly depends on Reynolds number. The latter study, however, focused on two-dimensional bodies, whereas the wake dynamics differ significantly in case of finite and semi-finite (wall-mounted) cylinders.

McClean and Sumner (2014) investigated the effect of incident angle on the coefficients of lift and drag, as well as the Strouhal number in the wake of finite square prisms with different aspect ratios at $Re = 7.3 \times 10^4$. They considered the critical incident angle as an angle that the drag coefficient reaches the minimum value, the lift coefficient reaches the most negative value, and the Strouhal number reaches its peak value. It was reported that the critical incident angle, drag coefficient, and Strouhal number decreases for the finite prism in comparison with an infinite prism, but the magnitude of the lift coefficient is approximately equal for both bodies. Unnikrishnan et al. (2017) experimentally studied the effect of incident angle on the mean wake behind surface mounted square prisms with different aspect ratios at $Re = 3.7 \times 10^4$ with a boundary layer

thickness of $\delta/D = 1.5$. They reported a critical incident angle in which the mean drag coeffi-
cient is minimum, while the mean lift coefficient and Strouhal number are both maximum. This
coincided with the smallest reported size of the wake, which was also highly asymmetric. These
studies, however, all focused on short-depth-ratio cylinders, in which the wake dynamics are very
different than those of a long (large depth-ratio) cylinder (Chapter3).

Sakamoto and Arie (1983) experimentally studied the effect of aspect ratio and turbulent
boundary layer thickness on the wake of circular and square cylinders at a range of Reynolds
numbers (based on the boundary layer thickness): $4128 \leq Re_\delta \leq 7332$. Their results indicated
that there exists a critical aspect ratio for cylinders, below which the wake structure changes from
Kármán-type to arc-type. It was also determined that the Strouhal number, corresponding to wake
fluctuations, is a function of the turbulent boundary layer thickness. However, decreasing the
boundary layer thickness below $\delta/h \leq 0.3$ significantly reduced its effect on the flow. Wang et al.
(2006) examined the effect of boundary layer thickness on wake characteristics of a wall-mounted
square (short-depth) cylinder with an aspect ratio of $AR = 4$ at Reynolds number of $11,500$. From
their experimental results, it was determined that increasing the thickness of the boundary layer
strengthens the upwash flow. Hence, this increases the probability of symmetric wake develop-
ments close to the ground. On the other hand, close to the free end face of the cylinder, there is a
higher probability for anti-symmetric arrangement of vortices. Hosseini et al. (2013) experimen-
tally measured different wake parameters for a rectangular cylinder of aspect ratio $AR = 8$ that
was partially immersed in a regular and tripped boundary layer with relatively low thickness at
$Re = 1.2 \times 10^4$. Based on their results, it was apparent that there are no variations in the shedding
frequency over the entire wake in either boundary layers, and the structures at opposite sides of the
cylinder are out of phase. It was also revealed that the connection between structures near the tip of
the cylinder is significantly different from an arch-type structure, since tip vortex is bent toward the
body and remains connected to the surface. Their results showed that the thickness of the boundary
layer has a profound effect on wake structures, with the ability to change them from quadrupole
to dipole type even for a large aspect ratio prism. In their experimental study on a wall-mounted

square cylinder of aspect ratio $AR = 4$ at $Re = 12000$, el2015boundary showed that the thickness of the incoming boundary layer can change the influence of horseshoe vortices in the wake behind a square (small-depth-ratio) cylinder. Using the time-space cross-correlation map, they confirmed that the horseshoe vortex in the flow with a larger boundary layer thickness affects the entire wake region behind the cylinder. However, this effect is weaker for the flow, in which the boundary layer thickness is smaller.

Kindree et al. (2018) investigated the effect of boundary layer on the wake of circular and square cylinders, and particularly the horseshoe vortex structures. The cylinder aspect ratio was $AR = 4$ and the Reynolds number varied in the range of $5000 \leq Re \leq 19700$. They identified low-frequency local fluctuations in the near wake of the cylinders when they are placed in front of a laminar boundary layer. This was attributed to the symmetric mode of shedding, contrary to the Kármán-type vortex shedding that exhibits a phase difference of $180°$. Kindree et al. (2018) further determined that low frequency fluctuations were weakened in the transitional boundary layer, whereas they were fully suppressed in a turbulent boundary layer. These observations hinted at the fact that low frequency fluctuations in the wake strongly depend on the boundary layer dynamics. Using Proper Orthogonal Decomposition (POD), Kawai et al. (2012) identified three different modes in the wake of a wall-mounted square (small-depth-ratio) cylinder with aspect ratio 2.7 and a thin boundary layer ($\delta/h = 0.3$) at $Re = 9400$ and 15600. These modes were associated with the arc-type pattern with opposite sense of rotation on each side of the body, close to the ground (mode 1), with the same sense of rotation on each side close to the free end face of the cylinder (mode 2), and Kármán-type structures in the middle region of the wake (mode 3). Power Spectral Density analysis of mode 1 and mode 3 showed a peak value of "9 Hz" associated with Kármán-type vortex shedding, whereas mode 2 revealed a peak value of "1.5 Hz" that was associated with the arc-type pattern close to the free end face of the cylinder. More recently, Porteous et al. (2017) performed a detailed acoustic and hot-wire measurement in the wake of wall-mounted square (small-depth-ratio) cylinders with aspect ratios ranging at $0.29 \leq AR \leq 22.9$, the boundary layer thickness of $\delta/w = 1.3$ and $Re = 1.4 \times 10^4$. They divided the wake structures

into four shedding regimes based on the number of peak frequencies observed in the wake. There were no peaks observed for regime 0 ($AR < 2$), one dominant peak was identified for regime 1 ($2 < AR < 10$), two distinct peaks were apparent for regime 2 ($10 < AR < 18$) and three peaks were determined to exist for regime 3 ($AR > 18$). The visualization of the vertical vortex filaments in the near wake revealed that they appear connected near the free end for regime 1 ($2 < AR < 10$), whereas the horizontal connection is not captured for the other regimes. These studies capture unique and critical information on the wake unsteadiness for small-depth-ratio cylinders, whereas such effects may be manifested differently, if at all, for the case of a large-depth-ratio cylinder.

A number of studies focused on different cross-sectional shapes for wall-mounted cylinders identified a similar variation in unsteady wake evolution compared to rectangular cylinders. For example, Buresti and Iungo (2010) reported three different shedding processes in the wake of a wall-mounted triangular cylinder with the parameter space that included $AR = 3$, $\delta/h \approx 0.056$ and $Re = 1.5 \times 10^5$. These peak frequencies ascribed by the alternative vortex shedding from lateral vertical edges ($St_1 \approx 0.16$), flag-like movement of the recirculation boundary near the mid-plane region ($St_2 \approx 0.09$) and oscillation of vortical structures on the free end face of the cylinder ($St_3 \approx 0.05$). Contrary to the latter peak frequency, the first and second peak frequencies could be manipulated by implementing add-on parts to the original shape. Thus, these peak frequencies appeared to be a function of the wake characteristics with the exception of low frequency dynamics. Buresti and Iungo (2010) reported that their efforts to change the characteristics of the low-frequency fluctuations through modification to the upper face of the cylinder were not successful. This phenomenon was attributed to the strength of wake structures responsible for the low-frequency fluctuations, which must have remained intact even after implementing such modifications to the body. In another experimental study, Iungo et al. (2012) examined the wake of a wall-mounted circular cylinder with the parameter space of $AR = 3$, $\delta/h = 0.09$ and $6 \times 10^4 \le Re \le 11 \times 10^4$. They reported a Strouhal number of $St = 0.15$, which ascribed to an alternate vortex shedding, below the half-height of the cylinder and a low-frequency fluctuation above the free end region.

The results reported in Chapter3 is the only comprehensive study of the wake of wall-mounted long (large-depth-ratio) rectangular cylinders. They focused on determining how the large depth-ratio alters the wake dynamics at $Re = 250$ and 1000. Two cylinders were studied, a square cylinder with aspect ratio of 0.83 and depth-ratio of 0.83, and a long rectangular cylinder with the same aspect ratio but a depth-ratio of 4.15. The simulated flow in lower Re exhibited an steady behavior for both cylinders, while the wake became unsteady at $Re = 1000$ with very different wake structures forming behind the long versus short cylinder. A new skeleton model was introduced that identified harpin-like structures formed on top of the long cylinder and shed into the wake. However, similar structures were suppressed on the side faces of the cylinder by the horseshoe structures that start transforming into a helical formation within half-way along the cylinder length. Four distinct Strouhal numbers were also identified that correspond to particular coherent structures in the wake: $St_{hp} = 0.64$ due to the hairpin structure on top of the cylinder, $St_{hp} = 0.38$ due to the hairpin structure on sides of the cylinder, $St_{hs} = 0.26$ due to the helical formation span out of the horseshoe structures on either sides, and $St_a = 0.175$ due to the arc-type structure formed in the wake behind the cylinder. The latter St was long-lasting in the wake, whereas the others diminished farther downstream.

Despite extensive research on the flow around wall-mounted cylinders over the past several decades, the effect of incident angle on the wake characteristics of a large-depth-ratio (long) cylinder remains unknown. Here, we aim to address this gap in literature by examining the flow around a large-depth-ratio (long) rectangular cylinder at a range of incident angle from $0°$ to $45°$. This knowledge is crucial in fundamental study of the wake symmetry and the onset of wake unsteadiness at a fixed Reynolds number with a wide range of practical engineering applications that spans from HVAC design in buildings to thermal analysis of electronic micro-chips. This chapter is structured such that a detailed description of the methodology and numerical setup is presented in Section 3.3. The main results and discussions are included in Section 3.4, which is followed by the summary of conclusions in Section 3.5.
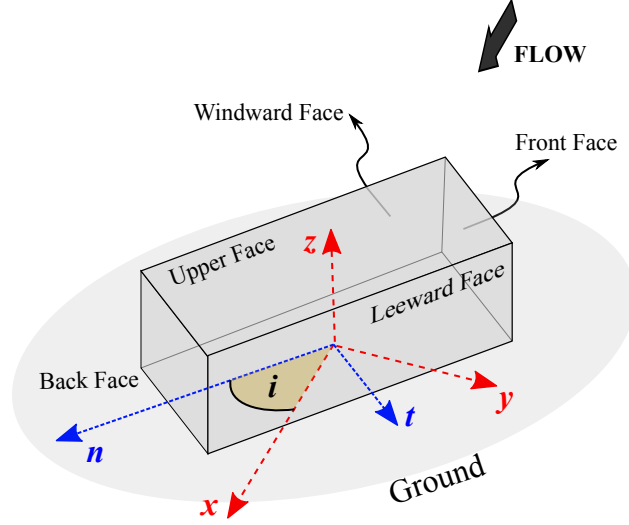
Figure 4.2: Schematic of the cylinder at 45° incident angle. (Not to scale)

4.3 Methodology

The flow around a large-depth-ratio (long) wall-mounted rectangular cylinder is numerically studied for a range of incident angles between 0° to 45° with the increments of 5°. The incident (yaw) angle is defined as the angle between the freestream flow ($x-$axis) and the long side of the cylinder, as shown in Figure 4.2. The cylinder dominant height (h) is used to normalize all dimensions and length-scales. The width and length of the cylinder are $w = 0.83h$ and $l = 4.15h$, respectively, which translate to a depth-ratio of $DR = l/h = 4.15$. The dimensions of the cylinder are selected to ensure that the separated shear layer from the cylinder leading edges will reattach to their corresponding face based on the observations of Okajima et al. (1992) that identified the critical aspect ratio (streamwise length to height ratio) for an infinitely span(2D) cylinder to be $3-4$. The uniform inlet velocity corresponds to a Reynolds number of 250, defined as:

$$Re = \frac{hU_0}{\nu},$$

where U_0 is the uniform freestream velocity, and ν is air kinematic viscosity. The boundary layer formed on the ground has a thickness of $\approx 0.5h$ at the cylinder frontal face. The schematics of the cylinder at 45° incident angle is shown in Figure 4.2. Here, the cylinder cross-sectional area is in
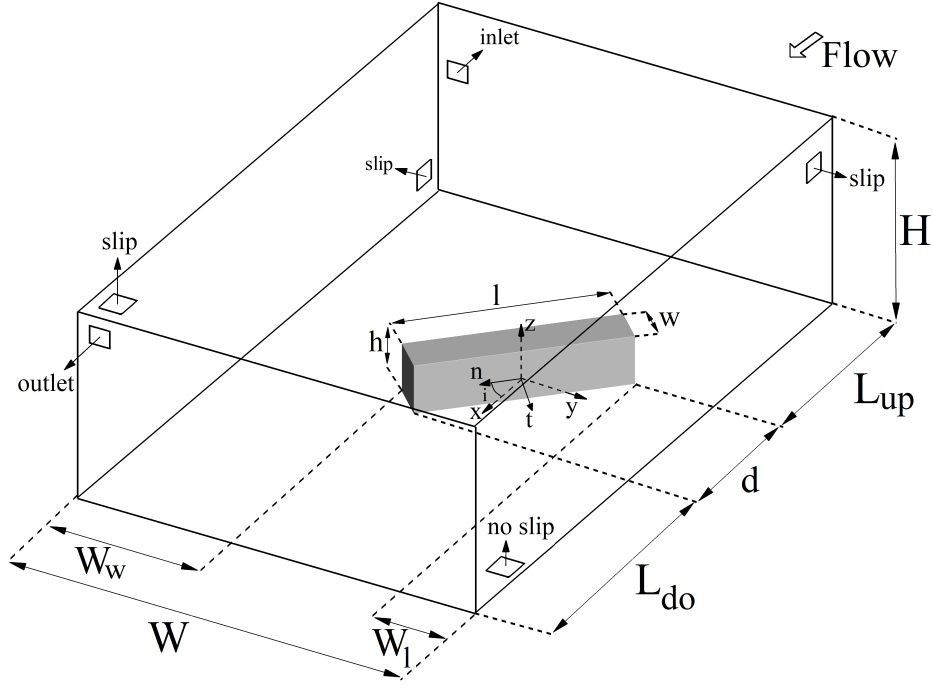
Figure 4.3: Schematic of the computational domain at $45°$ incident angle. (Not to scale)

the $yz-$plane and it extends in the streamwise ($x-$) direction. To better present and compare the results at different incident angles, we define a secondary local coordinate system in Figure 4.2, such that '$n-$axis' is aligned with the cylinder long face (or l), '$t-$axis' is aligned with the cylinder width (or w), and '$z-$axis' remains the normal direction. These local coordinates are normalized by the cylinder height (h).

4.3.1   Numerical Setup

The LES is utilized to solve continuity (Eq. 4.1) and momentum (Eq. 4.2) flow equations to examine the wake at 10 different incident (yaw) angles.

$$\frac{\partial u_i}{\partial x_i} = 0, \tag{4.1}$$

$$\frac{\partial u_i}{\partial t} + \frac{\partial u_i u_j}{\partial x_j} = -\frac{1}{\rho}\frac{\partial p}{\partial x_i} + \nu \frac{\partial^2 u_j}{\partial x_i x_j}, \tag{4.2}$$
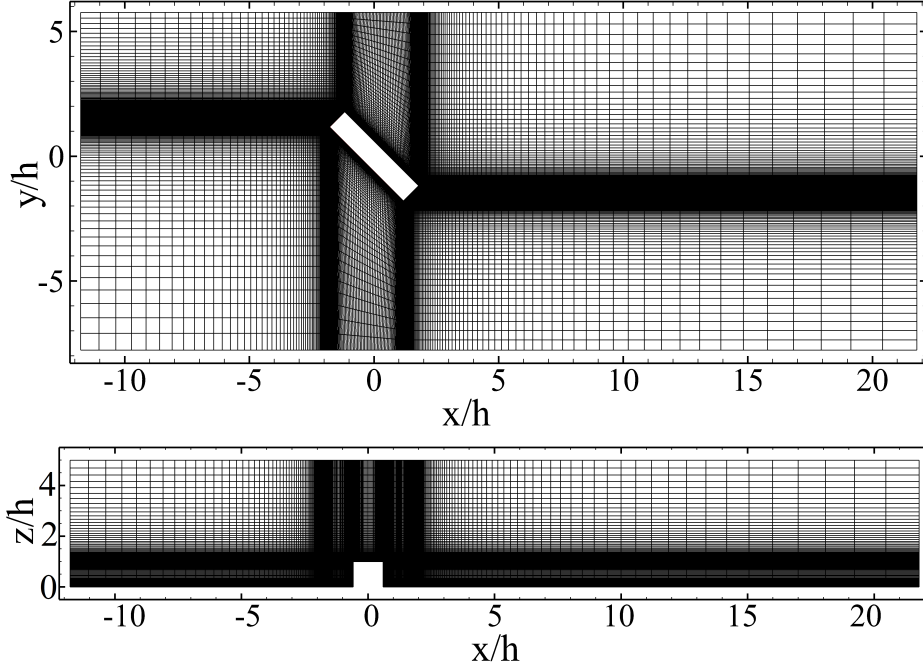
Figure 4.4: The spatial grid distribution for the long-rectangular cylinder at $Re = 250$ and incident angle of $i = 45°$. Top view at $z/h = 0.5$ (top) and side view at $y/h = 0$ (bottom).

where, u_i and p are the filtered resolved velocity and pressure, respectively(Durbin and Reif, 2011).

In the current study, different computational domains were generated such that the distance between faces of the wall-mounted cylinder and the closest domain boundary is at least $4.5h$. The streamwise $(x-)$, spanwise $(y-)$, and normal $(z-)$ dimensions of the computational domain, shown in Figure 4.3, are $L \approx 35h$, $H = 5h$, and $12h \leq W \leq 15h$. The front face of the body is located $L_{up} \approx 10h$ from the inlet and $L_{do} \approx 20h$ from the outlet. Due to the wake pressure distribution at $i = 5°$ to $i = 45°$, the flow was hypothesized, which was later confirmed, to lose its symmetry in the $y-$direction and to deviate towards the windward face of the cylinder. Thus, the separation distance between the domain side-boundary and the windward face of the cylinder (W_w in Figure 4.3) was set such that it is approximately 1.5 times longer than the distance of the other side-boundary from the leeward face of the cylinder (W_l in Figure 4.3).

A non-homogeneous grid with $3.9 \times 10^6 - 5.2 \times 10^6$ hexahedral elements are utilized to simulate the flow around the cylinder at different incident angles. The spatial grid distribution for the long rectangular cylinder at $Re = 250$ and $i = 45°$ is shown in Figure 4.4. The grids are designed such that the maximum value of y^+ is below 0.55 at the walls and the ground surface, which enables capturing flow fluctuations associated with the separated flow. The timesteps are set for each case such that the maximum Courant number remained below 0.8 throughout the simulation.

The constant uniform velocity is applied as the inlet boundary condition. Side and upper walls of the domain are set to slip boundary condition. The outlet boundary is set as the Neumann boundary condition, based on which $\partial \phi / \partial n = 0$, where ϕ is any flow variable. The surfaces of the cylinder and the ground are assigned the no-slip wall boundary condition. The spatial and temporal discretization of the governing equations are second-order accurate. The residual momentum root-mean-square of 10^{-6} was set as the criteria of convergence for each timestep. The PIMPLE algorithm, which is a combination of Pressure Implicit with Splitting of Operator (PISO) and Semi-Implicit Method for Pressure-Linked Equations (SIMPLE) methods, is used for coupling the pressure and velocity fields. The computational domain for each case is divided into 16 separate regions for parallel computations. The simulations are completed using Intel Platinum 8160F Skylake 2.1GHz cores at 15000 core hours on average.

4.3.2 Verification and Validation

The impact of domain size and spatial grid quality are investigated in Chapter3. The simulations at incidence angles of $i = 0°$ and $45°$ at $Re = 250$ are repeated using Direct Numerical Simulations (DNS). Due to the very high quality of the generated mesh for $Re = 250$, the results of LES and DNS collapse well (see Figure4.5). Thus, our results are similarly accurate to DNS as per the LES formulations, which suggests that SGS modeling is now spatially limited to scales similar to those of Kolmogorov scales.
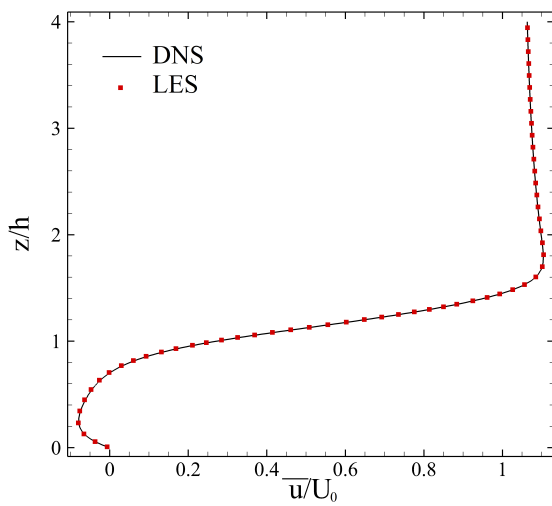
(a) streamwise velocity
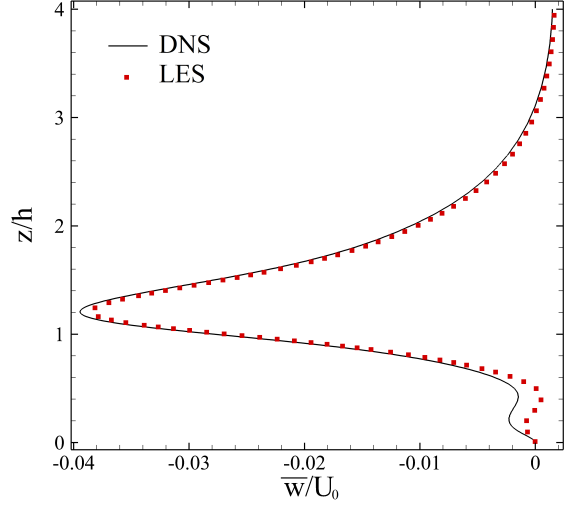
(b) normal velocity
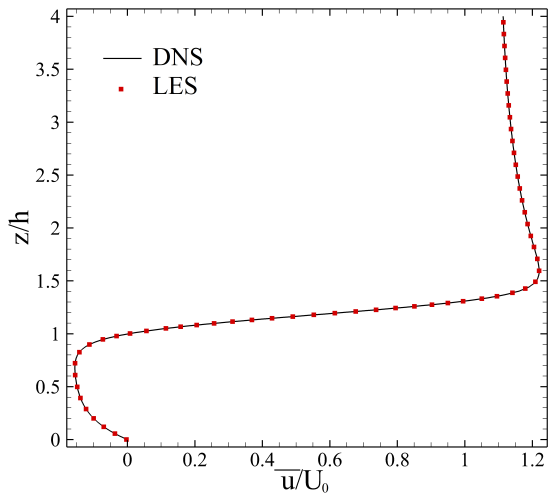
(c) streamwise velocity
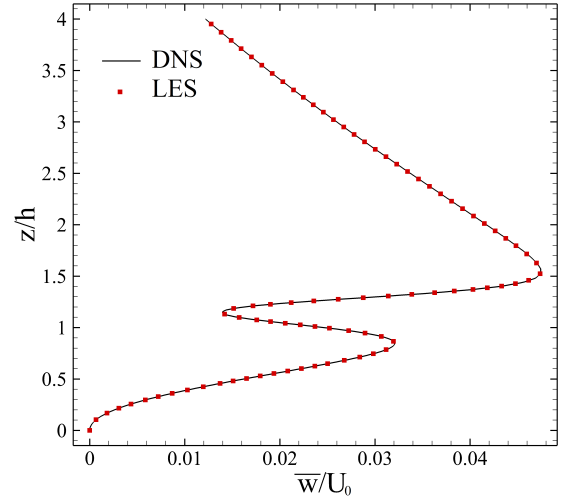
(d) normal velocity

Figure 4.5: Comparison of the DNS and LES results at $Re = 250$, $x/h = 1$ and $y/h = 0$ (a and b)$i = 0°$ (c and d)$i = 45°$

4.4   Results

The mean and transient characteristics of the large-depth-ratio (long) wall-mounted rectangular cylinder is evaluated at different incident angles by first looking at the iso-surface of $Q-$criterion in Figure 4.6. It is apparent that the wake topology transforms as the incident angle deviates from 0°, such that a single vortex tube is formed from behind the leeward faces of the cylinder. Both the size of the vortex tube, and that of the wake itself, increases at larger incident angles.

79

However, the simulated flow remains steady until $i = 40°$ (Figure 4.6e), at which point there appear characteristics of weak wake unsteadiness. At $45°$, the wake appears to become unsteady, in which helical structures dominate the flow (see Figure 4.6f).

The helical structures formed in the unsteady wake at $i = 45°$ significantly impact the differential and integral characteristics of the wake, such as surface pressure distributions and force coefficients. To examine the unsteady characteristics of the wake, velocity and pressure are captured and analyzed at 44 different probe locations in the wake, including $x/h = 2.5, 5$ and 10, $y/h = -2.5, -0.5, 0, 0.5$ and 2.5 and $z/h = 0, 0.45$ and 0.9 over time. The power spectral density (PSD) of velocity (not shown here for brevity) revealed that simulated flow remains steady at the incident angle of $35°$. However, the wake appears unsteady at $i = 40°$ and $45°$, although the unsteady behavior is weaker at the former incident angle. Thus, there is a critical range of incident angle between $35°$ and $40°$, at which the wake transitions to an unsteady wake at $Re = 250$. This hints at a potentially new wake transition mechanism at larger incident angles, since a horizontally oriented (zero incident angle) long cylinder did not experience such a transition. Similarly, short (small depth-ratio) cylinders and cubes transition to unsteady wakes at different Reynolds numbers with a range of $Re \approx 80 - 300$ (Saha, 2004; Rastan et al., 2017; Klotz et al., 2017). For example, Saha (2013) reported that decreasing the aspect ratio of a square cylinder from 5 to 2 alters the strongly unsteady flow at the former to a weakly unsteady flow for the latter at $Re = 250$. In case of long (large depth-ratio) cylinders, the effect of upwash and downwash flow are more substantial than short cylinders (Chapter3). Moreover, the interaction of a stronger upwash flow with the downwash shear layer weakens the probability of anti-symmetric vortex shedding in the near wake (Wang et al., 2006). This could delay the transitioning of the wake to unsteady flow. Thus, it is reasonable to hypothesize that the critical (transitional) Reynolds number for long cylinders occurs at $300 \le Re_{tr} < 1000$. The upper limit is selected here based on the results of Chapter3, which showed that the wake of a horizontally oriented long cylinder is unsteady at $Re = 1000$. Hence, a discussion on characteristic length scale, and its corresponding definition of Reynolds number, at larger incident angles deserve attention. This discussion follows later in this section.
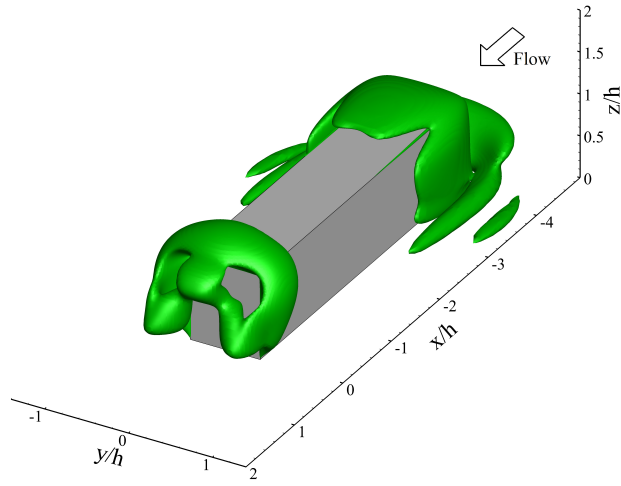
(a) $i = 0°$
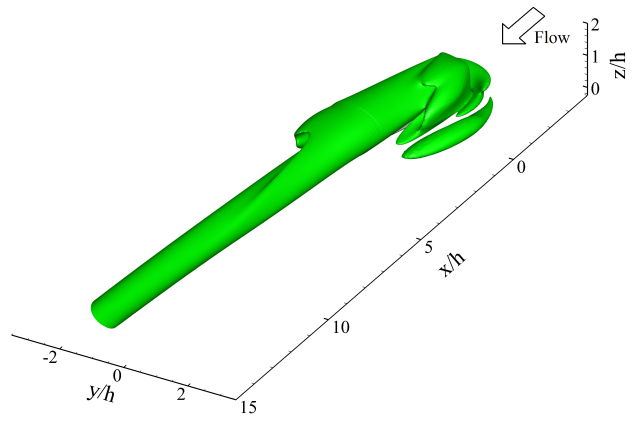
(b) $i = 15°$
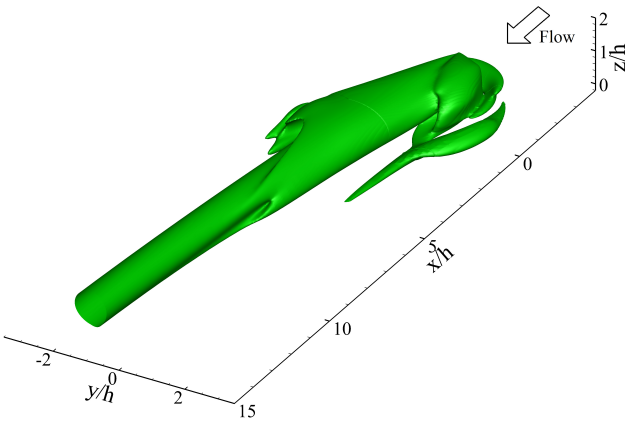
(c) $i = 25°$
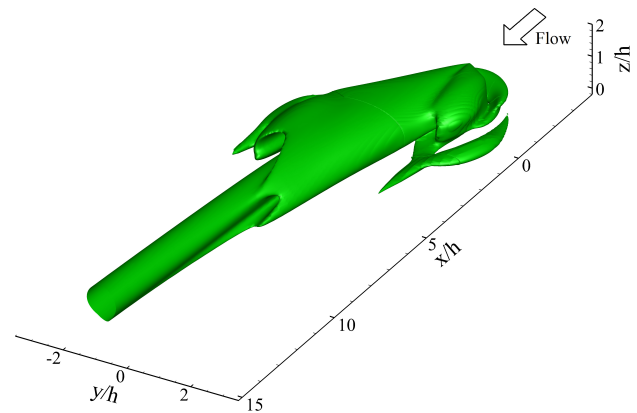
(d) $i = 35°$
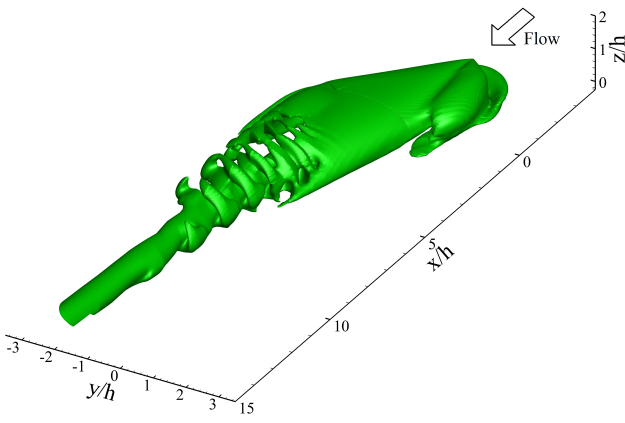
(e) $i = 40°$
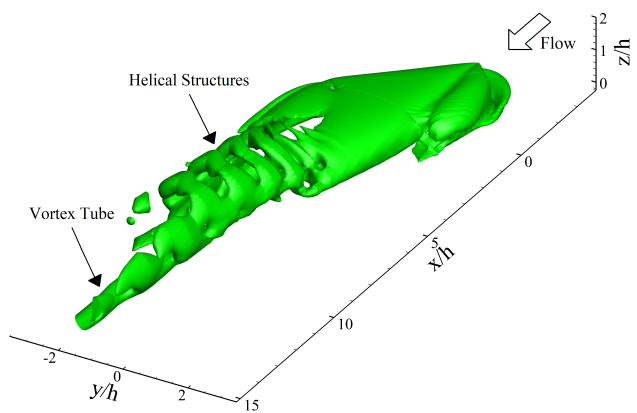
(f) $i = 45°$

Figure 4.6: Isosurface of $Q = 30$ at different incident (yaw) angles, $0° \leq i \leq 45°$, at $Re = 250$.

(a) normal ($z-$) component of velocity

(b) spanwise ($y-$) component of velocity
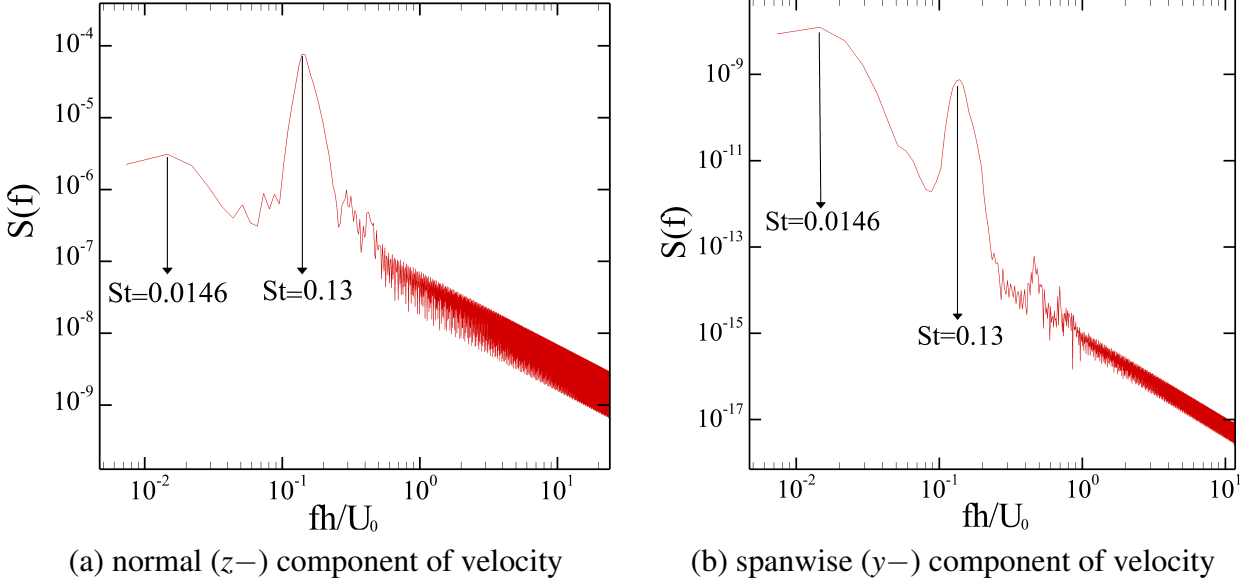
Figure 4.7: The PSD of velocity fluctuations at two probes located at (a) $x/h = 5$, $y/h = -2.5$ and $z/h = 0.9$, and (b) $x/h = 5$, $y/h = 2.5$, and $z/h = 0.9$ for the incident angle of $i = 45°$ at $Re = 250$.

(a) $t^* = t_0^*$

(b) $t^* = t_0^* + \frac{1}{3St}$

(a) $t^* = t_0^* + \frac{2}{3St}$

(b) $t^* = t_0^* + \frac{1}{St}$
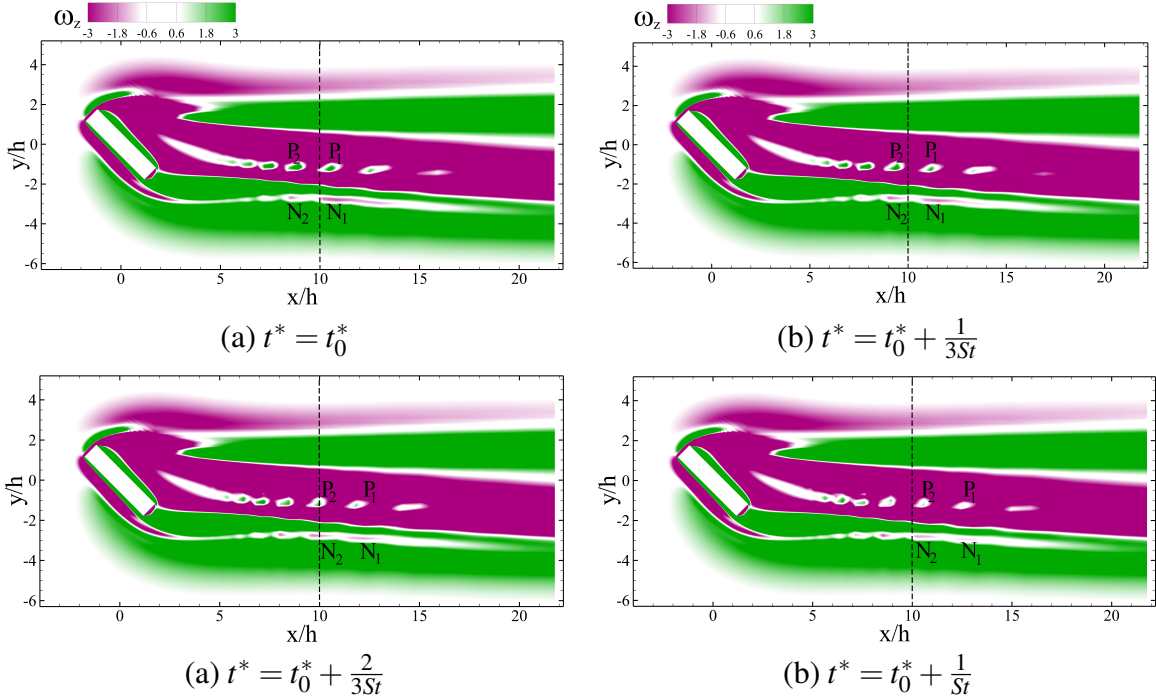
Figure 4.8: Contours of instantaneous vorticity in normal ($z-$) direction on the mid-plane ($z/h = 0.5$) of the cylinder at $Re = 250$ and $i = 45°$. Here, t^* is the convective time step and St is the Strouhal number of vortex shedding process.

The power density spectrum of velocity fluctuations in Figure 4.7 show a peak frequency (f_p) at the Strouhal number of $St = f_p h/U_0 = 0.13$ for $i = 45°$. This is exactly half of the St associated with

helical formations in the wake of a long cylinder at zero incident angle and $Re = 1000$(Chapter3). Furthermore, Wang and Zhou (2009) identified a single peak frequency at $St = 0.11$ over the entire wake region of a wall-mounted square (small-depth-ratio) cylinder with aspect ratio 4. There is also a weak low-frequency observed at Strouhal number of 0.0146 in Figure 4.7, which correspond to a unique low-frequency feature of the flow. Figure 4.8 shows the contours of instantaneous vorticity in the normal ($z-$) direction at mid-plane ($z/h = 0.5$) of the cylinder at $Re = 250$ and $i = 45°$ during four consecutive instants in the flow. Comparing arrangements of the center of vortices in Figure 4.8 confirms that velocity fluctuations corresponding to $St = 0.13$ relate to the vortex shedding in the wake region.

4.4.1   Low$-$Frequency Wake Features

The unsteady variations of the fluctuating normal velocity are shown in Figure 4.9 for the case of $i = 45°$. From the unsteady results, specially the shape of unsteady velocity variations, it is apparent that there exists a low-frequency signature in the wake that corresponds to $St = 0.0146$. This variation is depicted using black dashed lines in Figure 4.9a. It also corresponds to the large variations of lift in Figure 4.9b, in which the range of t_1^* to t_6^* is one period of low-frequency variations. A similar observation was also reported by Ayoub and Karamcheti (1982) in the wake of a wall-mounted cylinder, which they attributed to three-dimensional variations in the wake. Kindree et al. (2018) also reported observing low-frequency fluctuations corresponding to a Strouhal number of $St = 0.009 \pm 0.001$ in the wake of a wall-mounted cylinder exposed to a laminar boundary layer. Thus by inspection, the low frequency observed in the current wake is related to the three-dimensional effects(Ayoub and Karamcheti, 1982; Zeiger et al., 2004; Jiang et al., 2015).

The unsteady wake topology, and particularly the low-frequency features, are examined using isosurface of $Q-$criterion at the incident angle of $45°$ in Figure 4.10. These results depict the transient behavior of the wake over 6 consecutive instants that approximately correspond to one period of low-frequency fluctuation. Particularly, the timing of visualizations in Figure 4.10 correspond to $t_1^* = 530$ until $t_6^* = 620$, as depicted in Figure 4.9b. Evaluating the wake in this timeline
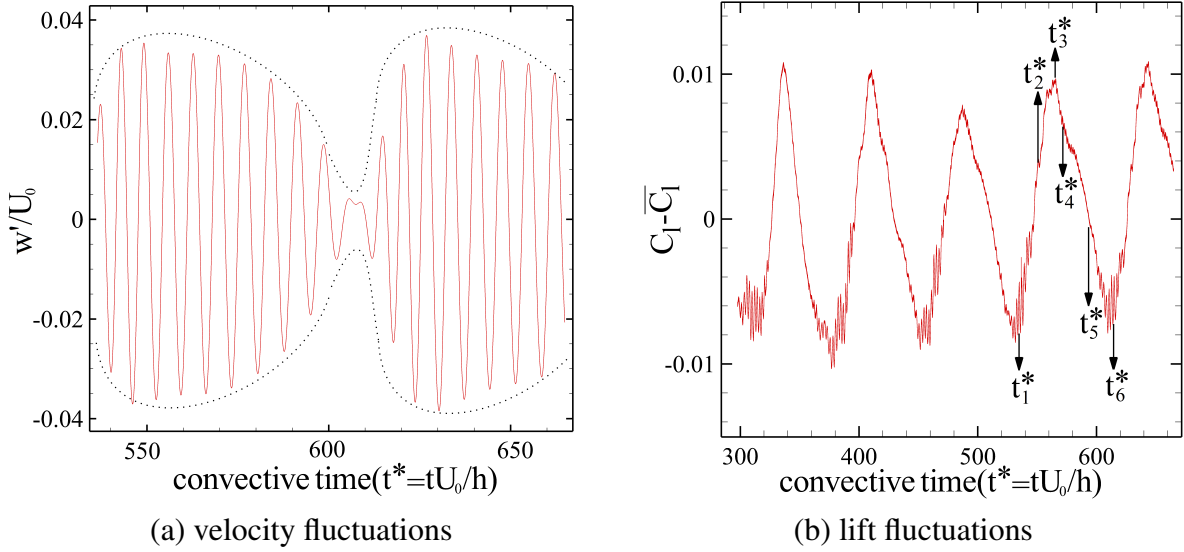
(a) velocity fluctuations

(b) lift fluctuations

Figure 4.9: The variation of (a) the normal component of velocity fluctuations at $(x/h = 5, y/h = -2.5, z/h = 0.9)$, and (b) coefficient of lift fluctuations.

enables exploring the implications of low-frequency fluctuations in the wake, in terms of alteration to structures or their interactions. In fact, the results in Figure 4.10 indicate that there exist alterations in the shape and size of unsteadily evolving helical structures and vortex tubes in the wake. The helical structures, which dominated the wake at $t_1^* = 530$, diminished in time and they were almost fully suppressed at $t_5^* = 595$. By $t_6^* = 620$, thereafter, the helical structures were restored similar to $t_1^* = 530$ with the period between $t_1^* - t_6^*$ approximately corresponding to one period of low-frequency fluctuation. This trend continued repeating over time. It appeared as if the mechanism at onset of unsteady flow is not yet fully stable, or strong enough, to remain intact throughout the wake. The results, and the supplementary video provided online, identified that suppression of the wake unsteadiness propagates from the wake towards the body at $t_3^* - t_5^*$ due to what we refer to here as low-frequency dynamics. As this low-frequency suppression was weakened, the initial mechanism that transitioned the wake to unsteadiness dominated again (at t_6^*), which led to the formation of helical structures again. It is the variation in the size and number of the helical structures that influence the velocity fluctuations in the wake (Figure 4.7 and Figure 4.9). It is also important to note that the unsharpened peak of low-frequency variations in Figure 4.7 is mainly due to the limited size of the statistical data. There also exists a high-frequency variations that

84
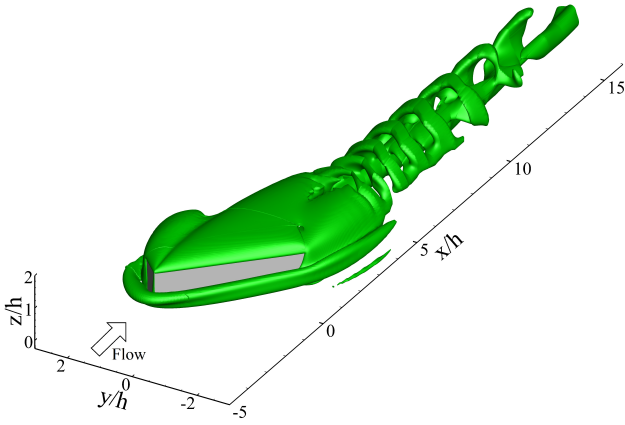
(a) $t_1^* = 530$
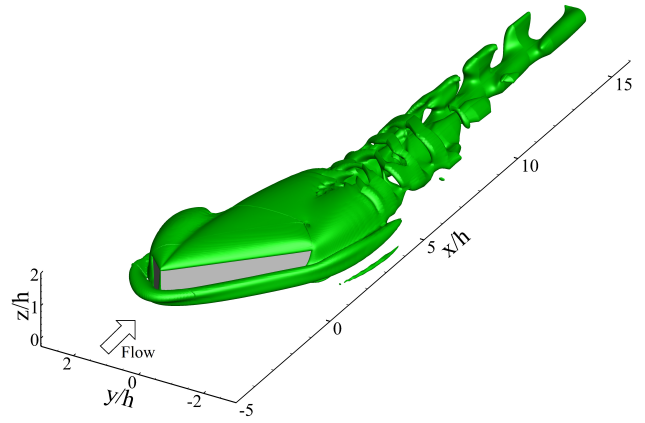
(b) $t_2^* = 550$
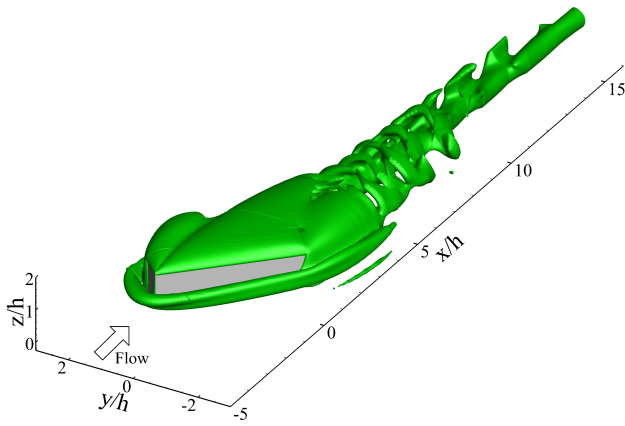
(c) $t_3^* = 570$
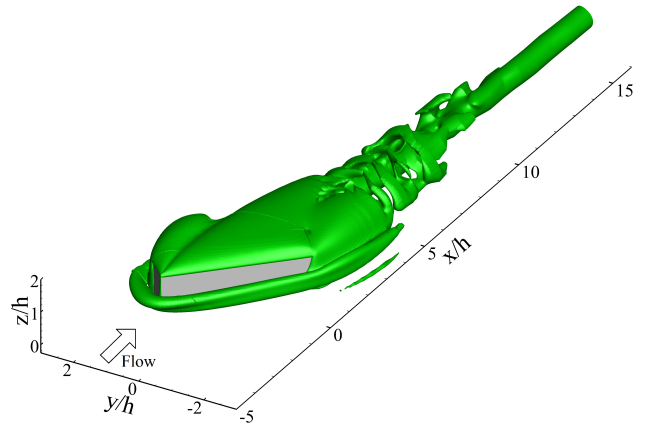
(d) $t_4^* = 580$
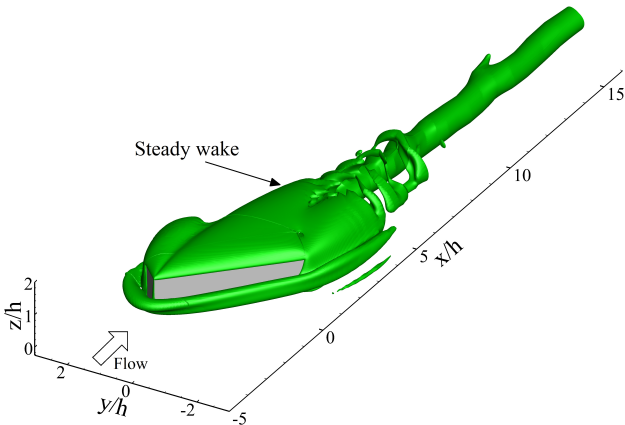
(e) $t_5^* = 595$
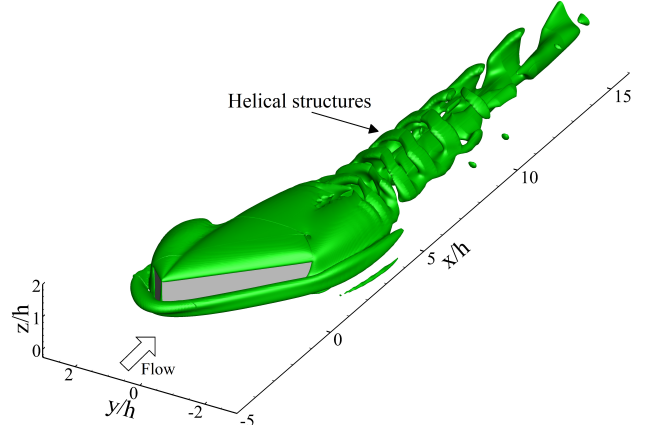
(f) $t_6^* = 620$

Figure 4.10: Variations of Q=30 isosurfaces for the case of $i = 45°$ at different convective times, t^*.
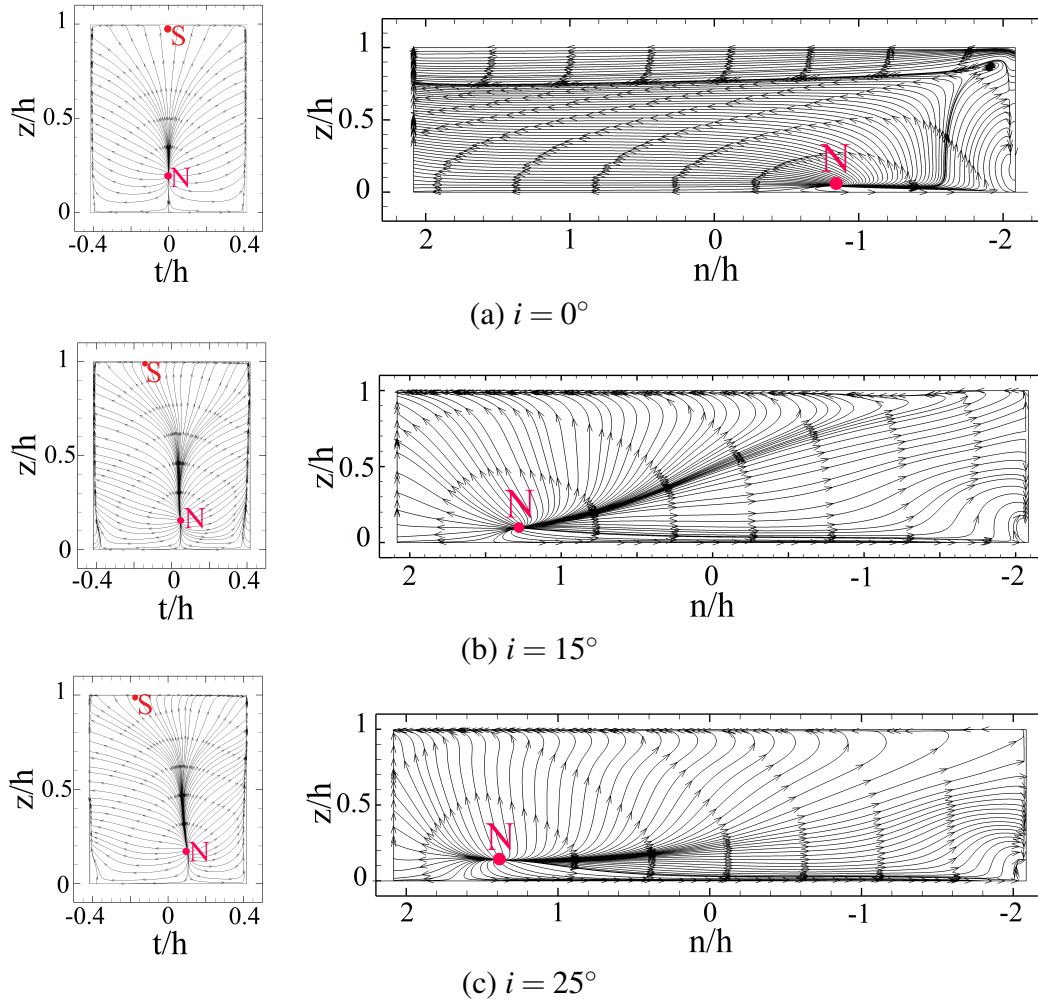
Figure 4.11: Nodal points associated with the attachment locations on windward and back faces of the cylinder at $i = 0°$, $15°$ and $25°$. The left-hand side plots show the streamlines on the back face of the cylinder, and the right-hand side plots show streamlines on the leeward face of the cylinder.

is more apparent in force fluctuations. Determining details on the source and nature of the these variations require further wake stability analysis that falls outside the scope of the current study.

The nodal point on the leeward and back faces of the cylinder indicate the reattachment of the separated flow from the leading edges. Figure 4.11 shows the time-averaged streamlines on the leeward and back faces of the cylinder at different incident angles. The misalignment of the saddle and nodal points on the back face of the cylinder for non-zero incident angles implies an asymmetry in the spanwise ($y-$) direction of the flow. Comparing the results in Figures 4.11 and 4.12 indicate that the distance between the reattachment points and the leading edges increases at

(d) $i = 35°$

(e) $i = 40°$

(f) $i = 45°$
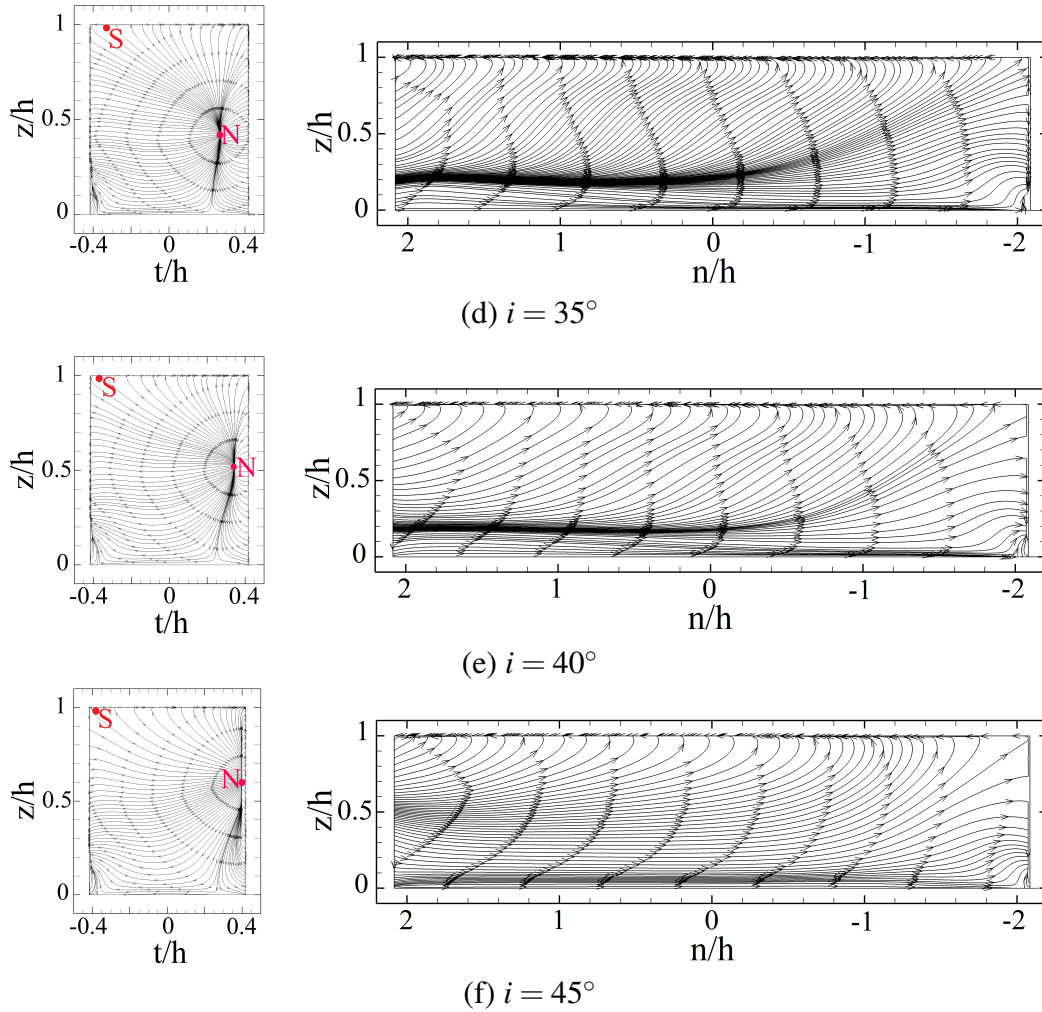
Figure 4.12: Continuation of Figure 4.11 for the cases of $i = 35°$, $40°$ and $45°$.

(a) $i = 35°$

(b) $i = 45°$
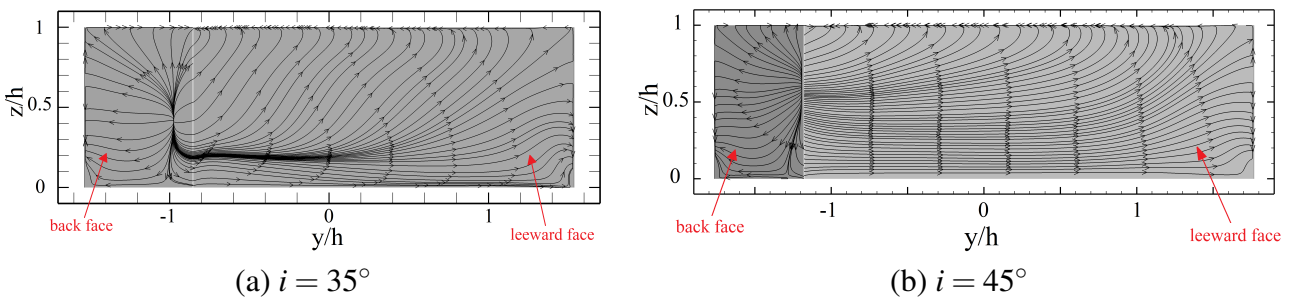
Figure 4.13: 2D time-averaged streamlines on the leeward and back faces of the cylinder at incident angles of $i = 35°$ and $45°$.

larger incident angles. However, there is a major alternation to this process starting at $i = 35°$, which remain thereafter ($i = 40°$ and $45°$), where the separated flow from the leeward leading edge of the cylinder did not reattach to the surface of the cylinder (see Figure 4.12). The streamlines

87

(a) $i = 25°$

(b) $i = 35°$

(c) $i = 40°$

(d) $i = 45°$
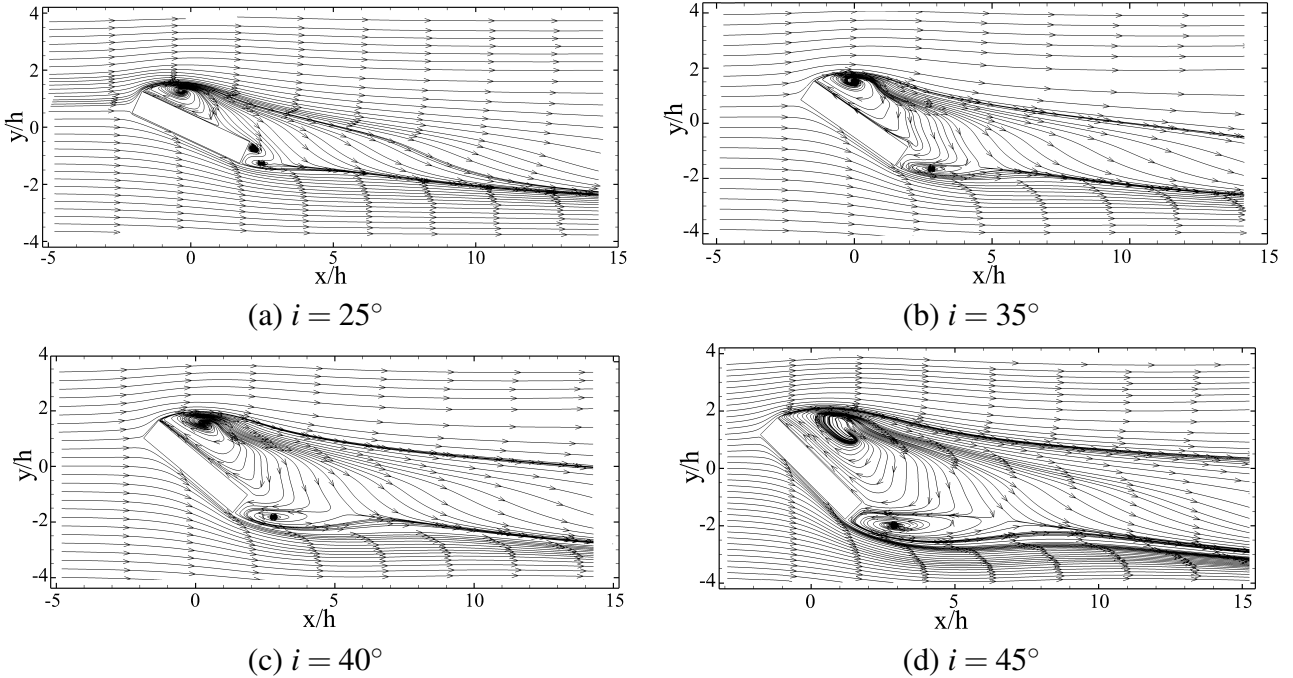
Figure 4.14: 2D time averaged streamlines in xy−plane at $z = 0.5$ plane at different incident angles

in Figure 4.13a further illustrate that the two points on the leeward and back faces of the cylinder merge starting at $i = 35°$, and thereafter. Thus, the separated flow from both leading edges of the cylinder reattach to its back face. Contrarily, there were no connection identified between the streamlines on the leeward and back faces of the cylinder at $i = 45°$ in Figure 4.13b. This implies that the separated flow from the leeward leading edge did not reattach to the surface of the cylinder, and thus there were no separation zones formed on the leeward face of the cylinder. This coincides with the fact that the wake appears very unsteady with low- and high-frequency fluctuations.

The formation of separation bubbles on the sides and upper faces of the long rectangular cylinder at the incidence angle of $0°$ is reported in Chapter3. However, Figure 4.14 shows that increasing the incident angle led to the suppression of the separation zone on the windward face of the cylinder. Contrarily, the size of the separation bubble on the leeward face, hence the size of the wake, increases at larger incident angles. As shown in Figure 4.14b, the separation zone on the leeward face merges with one of the focal points close to the back face of the cylinder at $i = 35°$, which forms a single recirculating region. It is also interesting to note that the missing reattachment for the separated flow from the leeward leading edge, reduces the strength of downward flow in the

spanwise ($y-$) direction (see Figure 4.14d). Hence, the focal point close to the leeward face of the cylinder loses its coherence at $i = 45°$.

4.4.2 Transition to Unsteady Flow

The mechanism of transition to unsteady wake at large incident angles involve an interaction between different tip vortices formed around the cylinder. Particularly, the tip vortex formed at the upper edge of the front face interacts with the vortex tube formed by the folding of the tip vortex from the upper edge of the windward face (long edge) of the cylinder. Figure 4.15 depicts the planer mean streamlines on the $yz-$planes overlaid by the isosurface of $Q-$criterion at four streamwise locations at $i = 35°$ and $45°$.

As shown in Figure 4.15, there exists a reversed flow region on the top face of the cylinder, which creates the vortical structure highlighted as "UTV" for both incident angles. This structure, however, diffuses before reaching the back face of the cylinder, and thus the near wake region. Evidently at $i = 45°$ and close to the mid-length of the cylinder ($x/h = 0$), there is a tip vortex formation (FTV in Figure 4.15a) that has an opposite vorticity-sign compared to the horseshoe vortex (HV) and the vortical structure on the top surface of the cylinder (UTV). This tip vortex is formed by roll-up of the separated flow from the cylinder vertex between its upper, windward, and front faces. This is referred to hereon as the "Frontal Tip Vortex" or FTV. This structure has the opposite vorticity-sign compared to the large tip vortex generated by folding of the shear layer formed along the upper edge of the windward face of the cylinder, which is referred to here as the "Windward Tip Vortex" (WTV). The FTV structure appears to be suppressed by the horseshoe structures (see Figures 4.15b and 4.15c for $i = 45°$). A similar observation is also valid for $i = 40°$. At $i = 35°$, however, only the UTV and WTV exist. Since the sense of rotation of the FTV is opposite of WTV and UTV, it suggests that the FTV may create excess disturbances, which translates into an unsteady helical formation spinning out of the vortex tube. Since FTV did not exist at $i = 35°$, the vortex tube was undisturbed. It is our hypothesis that the disturbances due to the existence of the FTV at $i = 45°$ and $40°$, is sufficient to initiate perturbations that translate to

$i = 45°$ $i = 35°$

(a) $x/h = 0$

(b) $x/h = 0.6$

(c) $x/h = 1.1$

(d) $x/h = 1.5$
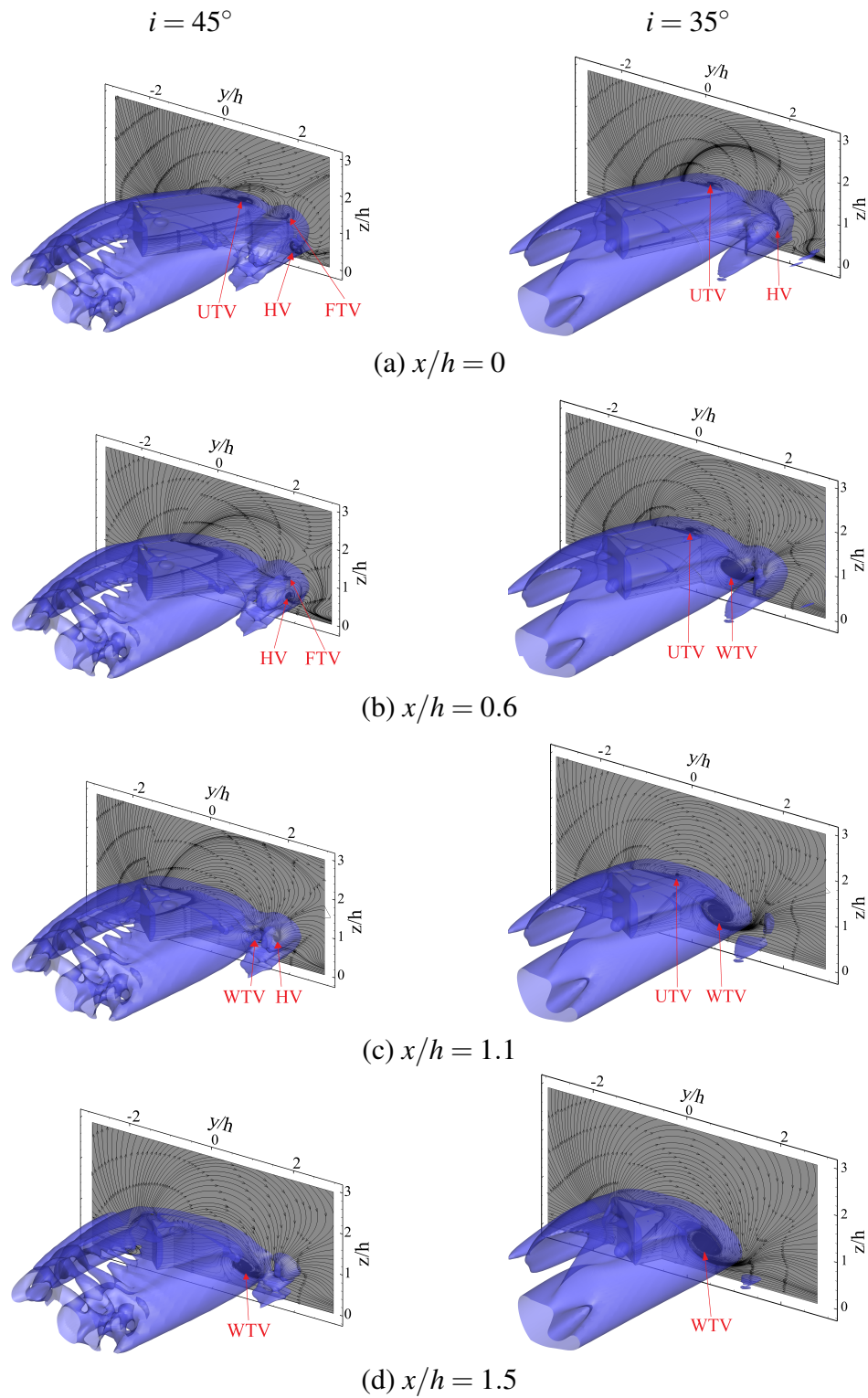
Figure 4.15: 2D streamlines on $yz-$plane at different streawise locations at two incident angles.
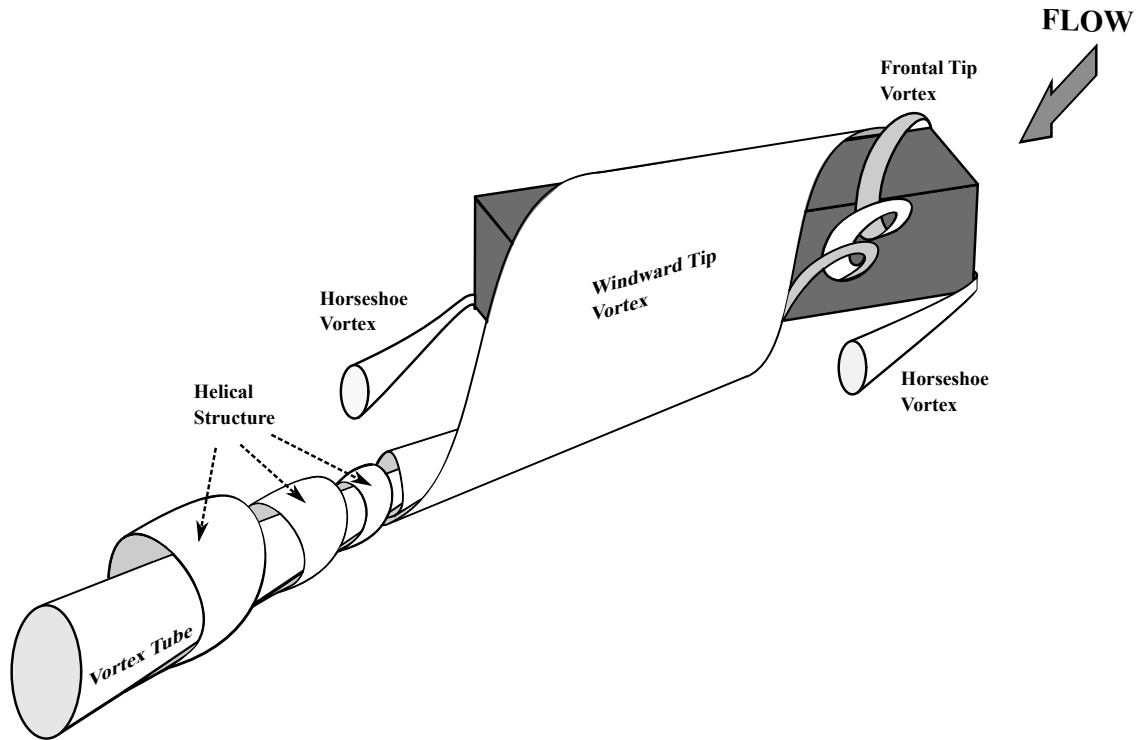
Figure 4.16: Skeleton model of the unsteady wake of a long rectangular cylinder at large incident angles.

unsteady flow. When such a combined rotatory motion is missing, FTV is not formed at $i = 35°$ for example, the vortical structure lacks the disturbances to sustain unsteady transition in the vortex tube. In both incident angles, however, the horseshoe vortex (HV) was suppressed by the formation vortex tube from the WTV (for clarification see Figure 4.15b for $i = 35°$ and Figure 4.15d for $i = 45°$).

A skeleton model of the unsteady wake at large incident angles is introduced that depict the main wake characteristics in Figure 4.16. Here, it is illustrated that the horseshoe structures are suppressed and diffuse quickly, whereas a vortex tube is formed by the WTV. Over time, helical structures are formed and shed out of the vortex tube due to added disturbances by the FTV. There is also a low-frequency mechanism connected with the helical structure, based on the interaction of FTV and WTV, which suppresses unsteady formation of this structure. This introduces a very complex wake system for intermediate incident angles (e.g., 45°), which is transformed to a different mechanism at 90° (not shown here for brevity).

4.4.3 Length Scale Correction

There is evidently a large alteration of the wake topology starting at $35° < i \leq 40°$, which implies variations in the wake characteristics, including the length scale and Reynolds number. Krajnovic and Davidson (2003) showed that the height of the bluff-body can be used as a characteristic length for calculating the Reynolds number when simulating flow around a bus-shaped bluff body, which is similar to a large-depth-ratio rectangular cylinder. Furthermore, most researchers working on characterization of the wake of a wall-mounted square (small-depth-ratio) cylinder used the width of the cylinder as the characteristic length. This is due to the fact that the majority of studies in this area are focused on relatively large aspect ratio cylinders ($AR > 3$), and thus height of the body cannot be a proper characteristic length. In the present research, the calculated Reynolds number based on the height of the body remains constant for different incident angles, which does not provide a proper metric for the onset of the unsteadiness at $i > 35°$. Furthermore, the variation of coefficients of lift and drag with respect to the incident angle in Figure 4.17 is non uniform, whereas their variations should be small. These observations hinted at the need to find a correct characteristic length at large incident angles that scales well with the variations of lift and drag.

At large incident angles, the characteristic length that remains aerodynamically relevant and changes with incident angle is the projected width of the cylinder on the plane of incoming flow. In Figure 4.17, the coefficients of lift and drag are defined based on the projected width (w_p) of the cylinder on the plane perpendicular to the upstream flow: $w_p = w\cos(i) + l\sin(i)$. Value of the Reynolds number based on the projected width (w_p) is also shown in Figure 4.17 as Re_{w_p}, which now increases at larger incident angles. Hence, the newly defined Re_{w_p} provides a better guideline for the state of the wake, and its transition to unsteadiness, at a range of incident angles. Particularly, the transition to unsteadiness in the range of $35° < i \leq 40°$ coincides with the range of $760 < Re_{w_p} \leq 830$. Evidently, the variations of lift and drag with respect to incident angle becomes uniform at large angles. This implies that the results scale better with w_p than the cylinder height at large incident angles.
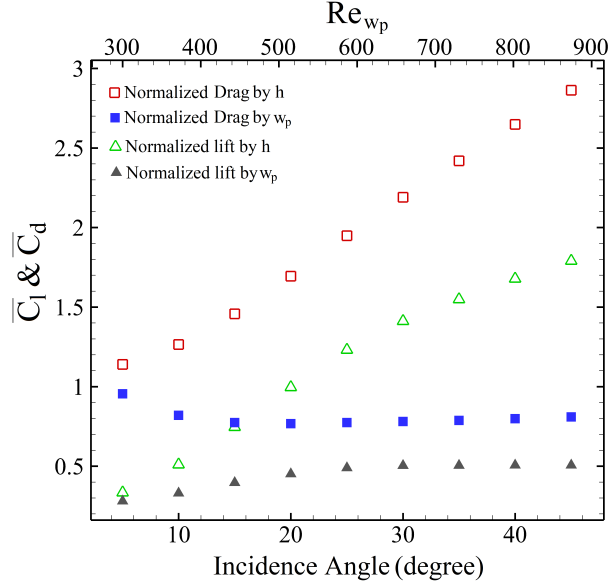
Figure 4.17: The variation of lift and drag coefficient with incident angle and Reynolds number based on the project length (Re_{w_p}).

4.5 Conclusion

The wake of a large-depth-ratio (long) wall-mounted rectangular cylinder is studied numerically at Reynolds number of 250, based on the cylinder height, in a range of incident (yaw) angles between 0° and 45° at 5° increments. The Reynolds number defined based on the projected width of the cylinder on the plane of the incoming flow is in the range of $Re_{w_p} = 208$ and 885 for the minimum and maximum incident angles, respectively. A significant variation in the wake topology is also observed at larger incident angles, which aligns with the changes to Reynolds number. The simulated flow is steady at small incident angles ($i \leq 35°$) and dominated by a vortex tube, whereas it becomes weakly unsteady at $35° < i \leq 40°$, and unsteady thereafter.

The results illustrated that increasing the incident angle leads to the suppression of the separation bubble on the windward face, and its expansion on the leeward faces, of the cylinder. The distribution of critical points on these surfaces of the cylinder showed that for $i \leq 30°$, the separated flow from the rear and leeward leading edges reattach to the cylinder at distinct points. However, these points merge to form a single one at $i = 35°$ and 40°. This coincided with the onset of unsteadiness at the transition range of incident angles between $i = 35°$ and 40°. Moreover, the

separated flow from the leeward leading edge did not reattach to the cylinder's faces at $i = 45°$, which coincides with a complex unsteady wake.

The unsteady wake of the long cylinder at $i \geq 40°$ is dominated by helical structures that are generated by the interaction of tip vortices formed on the upper (frontal and windward) edges of the cylinder. This interaction did not occur at incident angles below $40°$. The large windward tip vortex transformed into a vortex tube, the downwash effect of which suppressed both horseshoe vortices. The proposed skeleton model of the wake depicts two other tip vortices that are crucial in the wake topology. The interaction of these tip vortices, namely Frontal Tip Vortex (FTV), Upper Tip Vortex (UTV) and Windward Tip Vortex (WTV), led to a complex mechanism for formation and supression of unsteady wake features. Thus, there existed different dominant frequencies in the wake of the cylinder at $i = 45°$. The fluctuations corresponding to Strouhal number of $St = 0.13$ was related to the regular vortex shedding in the wake of wall-mounted cylinders, resulting from interaction of WTV and UTV. The variations corresponding to $St = 0.0146$ belonged to a low-frequency feature in the wake that relate to the interaction of WTV and FTV. The periodic suppression of helical structures and the unsteady wake followed a low-frequency variation. There were evidence that the regular vortex shedding and low-frequency processes are distinct. This hint that there are multiple distinct, but coupled, mechanisms in the wake at a larger incident angle. Further characterization of the low- and high-frequency fluctuations require instability analysis of the wake.

Chapter 5

CONCLUSION

This dissertation examined in detail the wake topology of a large depth-ratio cylinder at different incident angles ranging from $i = 0°$ to $45°$ at Reynolds number of 250 and 1000. The first of two objectives in this research involve understanding the implications of large depth-ratio on wake characterization and model at zero incident angle for a rectangular wall-mounted cylinder. The second focuses on characterizing the implications of incident angle of the cylinder on the wake topology and evolution. This systematic study of the wake enables an insight into how the wake topology changes with the introduction of severe asymmetry by the large depth-ratio (length) of the cylinder at large incident angles.

The effect of depth-ratio variation was investigated numerically by simulating the flow around a square (small depth-ratio of 0.83) and a long rectangular (large depth-ratio of 4.15) cylinder at $Re =$ 250 and 1000 using Large Eddy Simulations. The results showed that the simulated flow remains steady for both cylinders at $Re = 250$. However, the distribution of critical points, wake vorticity, and the strength of upwash and downwash flow alters dramatically by the large depth-ratio. At $Re = 1000$, the flow behavior transforms to an unsteady wake, which was dominated by hairpin-like vortices and horseshoe vortex loops formed in the flow. These structure were unique to large depth-ratio cylinders, which were be observed in the flow around small depth-ratio (short) cylinders, e.g., square cylinders. The majority of previous studies reported a single peak frequency in the wake

95

of a small depth-ratio (short) cylinder. However in the present study, different distinct frequencies are captured in the wake of the large depth-ratio cylinder. The Strouhal number of $St_{hp} = 0.38$ and 0.64 were attributed to the hairpin-like vortices on the cylinder upper and side faces, whereas only the upper hairpin structures remained intact in the wake. The frequency associated with $St_H = 0.26$ was due to the horseshoe vortex loops formed by the transition of the horseshoe vortex tubes along the sides of the cylinder, which suppressed the side hairpin structures prior to the start of the wake. The peak frequency corresponding to $St_H = 0.175$ was ascribed by the arc-type structures in the wake, the effect of which remained distinct in downstream region of the wake. A new skeleton model was introduced for large depth-ratio cylinders that depicted these main wake structures that are unique for this body.

The effect of incident (yaw) angle variation was studied by simulating the flow around large depth-ratio cylinders positioned at 10 different incident (yaw) angles between $i = 0°$ and $i = 45°$ with increments of $5°$. Simulations were carried out using LES at Reynolds number of 250. The results showed that increasing the incident angle changes the wake flow from symmetric to asymmetric. Furthermore, it led to the suppression and enlargement of the separation bubbles on the cylinder windward and leeward faces, respectively. For incident angles of $i \leq 35°$, the separated flow from the rear and leeward leading edges reattached to the cylinder at distinct points. However, these points merged to form a single one at $i = 35°$ and $40°$. The onset of wake unsteadiness occurred in the same manner. The weakly unsteady flow characteristics were captured in the wake of the cylinder at $i = 40°$. The separated flow from the cylinder leeward leading edge did not reattach to the cylinder faces at $i = 45°$. This coincided with a stronger set of wake unsteady characteristics, such as large amplitude of fluctuations and more energetic frequency signatures. The main alteration to the wake topology due to the changing incident angle was the formation of helical structures that dominated the near wake region at $i = 40°$ and $45°$. Three distinct dominant frequencies were observed in the wake at $i = 45°$. The Strouhal number of $St = 0.13$ was attributed to the vortex shedding process in the wake region. The low-frequency fluctuations corresponding to $St_H = 0.0146$ was associated with the alterations in the shape and size of unsteadily evolving heli-

96

cal structures and vortex tubes in the wake. Moreover, a high-frequency fluctuation corresponding to $St_H = 0.46$ combined with a low-frequency fluctuation at $St_H = 0.0146$ related to the formation and suppression of helical structure that dominated the unsteady wake. A new skeleton model is introduced for the wake at large incident angles, which highlights important flow features that dominate the wake. Particularly, the model describes how the interaction two tip vortices, namely Frontal Tip Vortex and Windward Tip Vortex, dictate the low- and high-frequency features of the wake. The transition of the wake to unsteady flow even at $Re = 250$ for large incident angles hinted at a change of the dominant characteristic length, based on which a new Reynolds number can be defined. Thus, it was shown that the projected width of the cylinder dominated the flow, which scaled better with the integral flow parameters, such as lift and drag, compared to the width or height of the cylinder. The calculated Reynolds number by the projected width varies by changing the incidence angle, which explains the unsteady nature of the flow field for $i > 35°$.

5.1 Future Work

The results of the present study showed that wake structures formed around a large depth-ratio wall-mounted cylinder are sharply different from those in the wake of small depth-ratio (short) cylinders. Thus, a comprehensive series of simulations are required to identify the critical value of the depth-ratio at which wake topology changes. Furthermore, determining the critical Reynolds number for the wake unsteady transition for the case of different depth-ratios of wall-mounted cylinders can be highly beneficial in optimizing the design of industrial equipment and applications, such as heat-exchangers.

One of the most critical changes in the flow around a large depth-ratio cylinder is the formation of separation bubbles on side and upper surfaces of the cylinder. These separation zones are a function of the Reynolds number. Therefore, studying the characteristics of these structures at very high Reynolds number can enrich our knowledge about the fluid dynamic of ground vehicles such as trailer-trucks. Moreover, finding optimal passive or active flow control methods for modifying

97

the characteristics of the coherent structure in the wake of wall-mounted cylinders can lead to drag reduction and noise control.

The incident angle plays a critical role in characterizing the flow around a large depth-ratio wall-mounted cylinder. The upstream cross-sectional shape of the cylinder can strongly alter the horseshoe vortex characteristics. Thus, studying the simultaneous effect of incident angle, Reynolds number, and upstream cross-sectional shape can lead to a better understanding of the stability in ground vehicles or the optimization of heat-exchangers.

Bibliography

Anderson, J. (1991). *Modern Compressible Flow: with historical perspective—Second edition*, pages 4–6. Cambridge University Press.

Arslan, T., Malavasi, S., Pettersen, B., and Andersson, H. I. (2013). Turbulent flow around a semi-submerged rectangular cylinder. *Journal of Offshore Mechanics and Arctic Engineering*, 135(4).

Ayoub, A. and Karamcheti, K. (1982). An experiment on the flow past a finite circular cylinder at high subcritical and supercritical reynolds numbers. *Journal of Fluid Mechanics*, 118.

Babu, V. (2015). *Fundamentals of gas dynamics*, page 1. John Wiley & Sons.

Batchelor, G. K. (2000). *An introduction to fluid dynamics*, pages 1–149. Cambridge university press.

Becker, S., Lienhart, H., and Durst, F. (2002). Flow around three-dimensional obstacles in boundary layers. *Journal of Wind Engineering and Industrial Aerodynamics*, 90(4-5):265–279.

Behera, S. and Saha, A. K. (2019). Characteristics of the flow past a wall-mounted finite-length square cylinder at low reynolds number with varying boundary layer thickness. *Journal of Fluids Engineering*, 141(6).

Bruno, L., Coste, N., and Fransos, D. (2012). Simulated flow around a rectangular 5: 1 cylinder: Spanwise discretisation effects and emerging flow features. *Journal of Wind Engineering and Industrial Aerodynamics*, 104:203–215.

Bruno, L., Fransos, D., Coste, N., and Bosco, A. (2010). 3d flow around a rectangular cylinder: a computational study. *Journal of Wind Engineering and Industrial Aerodynamics*, 98(6-7):263–276.

Bruno, L., Salvetti, M. V., and Ricciardelli, F. (2014). Benchmark on the aerodynamics of a rectangular 5: 1 cylinder: an overview after the first four years of activity. *Journal of Wind Engineering and Industrial Aerodynamics*, 126:87–106.

Buresti, G. and Iungo, G. V. (2010). Experimental investigation on the connection between flow fluctuations and vorticity dynamics in the near wake of a triangular prism placed vertically on a plane. *Journal of wind engineering and industrial aerodynamics*, 98(6-7):253–262.

Cantwell, B. and Coles, D. (1983). An experimental study of entrainment and transport in the turbulent near wake of a circular cylinder. *Journal of Fluid Mechanics*, 136:321–374.

Castro, I. and Robins, A. (1977). The flow around a surface-mounted cube in uniform and turbulent streams. *Journal of fluid Mechanics*, 79(2):307–335.

Chapman, G. T. and Yates, L. A. (1991). Topology of flow separation on three-dimensional bodies. *Applied Mechanics Reviews*, 44(7):329–345.

Cimarelli, A., Leonforte, A., and Angeli, D. (2018). Direct numerical simulation of the flow around a rectangular cylinder at a moderately high reynolds number. *Journal of Wind Engineering and Industrial Aerodynamics*, 174:39–49.

da Silva, B. L., Chakravarty, R., Sumner, D., and Bergstrom, D. J. (2020). Aerodynamic forces and three-dimensional flow structures in the mean wake of a surface-mounted finite-height square prism. *International Journal of Heat and Fluid Flow*, 83.

Davidson, L. (2020). *Fluid mechanics, turbulent flow and turbulence modeling*, pages 26–192. Chalmers University of Technology.

Davidson, P. (2004). *Turbulence: an introduction for scientists and engineers*, page 4. Oxford University Press.

Délery, J. (2013). *Three-dimensional separated flow topology: critical points, separation lines and vortical structures*. John Wiley & Sons.

Dousset, V. and Pothérat, A. (2010). Formation mechanism of hairpin vortices in the wake of a truncated square cylinder in a duct. *Journal of Fluid Mechanics*.

Durbin, P. A. and Reif, B. P. (2011). *Statistical theory and modeling for turbulent flows*. John Wiley & Sons.

El Hassan, M., Bourgeois, J., and Martinuzzi, R. (2015). Boundary layer effect on the vortex shedding of wall-mounted rectangular cylinder. *Experiments in Fluids*, 56(2).

Guissart, A., Andrianne, T., Dimitriadis, G., and Terrapon, V. E. (2019). Numerical and experimental study of the flow around a 4: 1 rectangular cylinder at moderate reynolds number. *Journal of Wind Engineering and Industrial Aerodynamics*, 189:289–303.

Hemmati, A., Wood, D. H., and Martinuzzi, R. J. (2016a). Characteristics of distinct flow regimes in the wake of an infinite span normal thin flat plate. *International Journal of Heat and Fluid Flow*, 62:423–436.

Hemmati, A., Wood, D. H., and Martinuzzi, R. J. (2016b). Effect of side-edge vortices and secondary induced flow on the wake of normal thin flat plates. *International Journal of Heat and Fluid Flow*, 61A:197 – 212.

Hemmati, A., Wood, D. H., and Martinuzzi, R. J. (2018). On simulating the flow past a normal thin flat plate. *Journal of Wind Engineering and Industrial Aerodynamics*, 174:170 – 187.

Hosseini, Z., Bourgeois, J., and Martinuzzi, R. (2013). Large-scale structures in dipole and quadrupole wakes of a wall-mounted finite rectangular cylinder. *Experiments in fluids*, 54(9).

Hussain, A. F. (1986). Coherent structures and turbulence. *Journal of Fluid Mechanics*, 173:303–356.

Hwang, J.-Y. and Yang, K.-S. (2004). Numerical study of vortical structures around a wall-mounted cubic obstacle in channel flow. *Physics of Fluids*, 16(7):2382–2394.

Iungo, G. V., Pii, L. M., and Buresti, G. (2012). Experimental investigation on the aerodynamic loads and wake flow features of a low aspect-ratio circular cylinder. *Journal of Fluids and Structures*, 28:279–291.

Jiang, F., Gallardo, J. P., Andersson, H. I., and Zhang, Z. (2015). The transitional wake behind an inclined prolate spheroid. *Physics of Fluids*, 27(9).

Kawai, H., Okuda, Y., and Ohashi, M. (2012). Near wake structure behind a 3d square prism with the aspect ratio of 2.7 in a shallow boundary layer flow. *Journal of wind engineering and industrial aerodynamics*, 104:196–202.

Kindree, M. G., Shahroodi, M., and Martinuzzi, R. J. (2018). Low-frequency dynamics in the turbulent wake of cantilevered square and circular cylinders protruding a thin laminar boundary layer. *Experiments in Fluids*, 59(12).

Kline (1967). S. j., reynolds, w. c., schraub, f. a. & runstadler, pw. *J. Fluid Mech.*, 1967:30–741.

Klotz, L., Goujon-Durand, S., Rokicki, J., and Wesfreid, J. (2017). Experimental investigation of flow behind a cube for moderate reynolds numbers. *arXiv preprint arXiv*.

Krajnovic, S. and Davidson, L. (1999). Large-eddy simulation of the flow around a surface-mounted cube using a dynamic one-equation subgrid model. In *First Symposium on Turbulence and Shear Flow Phenomena*. Begel House Inc.

Krajnovic, S. and Davidson, L. (2003). Numerical study of the flow around a bus-shaped body. *J. Fluids Eng.*, 125(3):500–509.

Krajnovic, S. and Davidson, L. (2005a). Flow around a simplified car, part 1: large eddy simulation. *Journal of Fluids Engineering*, 127(5):907–918.

Krajnovic, S. and Davidson, L. (2005b). Flow around a simplified car, part 2: understanding the flow. *Journal of Fluids Engineering*, 127(5):919–928.

Kuethe, A., Chow, C., Vought, A., II, C., and Helicopters, B. M. (1998). *Foundations of Aerodynamics: Bases of Aerodynamic Design—Fifth edition*. John Wiley & Sons, Inc.

Liakos, A. and Malamataris, N. A. (2014). Direct numerical simulation of steady state, three dimensional, laminar flow around a wall mounted cube. *Physics of Fluids*, 26(5).

Lyn, D. A., Einav, S., Rodi, W., and Park, J.-H. (1995). A laser-doppler velocimetry study of ensemble-averaged characteristics of the turbulent near wake of a square cylinder. *Journal of Fluid Mechanics*, 304:285–319.

Martinuzzi, R. (1982). *Experimentelle Untersuchungen der Umstr.omung wandgebundener, rechteckiger, prismatischer Hindernisse, Dissertation Thesis*. PhD thesis, Universit.at Erlangen-N.urnberg.

McClean, J. and Sumner, D. (2014). An experimental investigation of aspect ratio and incidence angle effects for the flow around surface-mounted finite-height square prisms. *Journal of Fluids Engineering*, 136(8).

Moin, P. and Mahesh, K. (1998). Direct numerical simulation: a tool in turbulence research. *Annual review of fluid mechanics*, 30(1):539–578.

Nakamura, Y. (1993). Bluff-body aerodynamics and turbulence. *Journal of Wind Engineering and Industrial Aerodynamics*, 49(1-3):65–78.

Okajima, A. (1982). Strouhal numbers of rectangular cylinders. *Journal of Fluid Mechanics*, 123:379–398.

Okajima, A., Ueno, H., and Sakai, H. (1992). Numerical simulation of laminar and turbulent flows around rectangular cylinders. *International journal for numerical methods in fluids*, 15(9):999–1012.

Okuda, Y. and Taniike, Y. (1993). Conical vortices over side face of a three-dimensional square prism. *Journal of wind engineering and industrial aerodynamics*, 50:163–172.

OpenFOAM (2004). Openfoam descriptin and tutorial. `https://www.openfoam.com/`.

Park, D. and Yang, K.-S. (2016). Flow instabilities in the wake of a rounded square cylinder. *Journal of Fluid Mechanics*, 793:915–932.

Perry, A., Chong, M., and Lim, T. (1982). The vortex-shedding process behind two-dimensional bluff bodies. *Journal of Fluid Mechanics*, 116:77–90.

Porteous, R., Moreau, D. J., and Doolan, C. J. (2017). The aeroacoustics of finite wall-mounted square cylinders. *Journal of Fluid Mechanics*, 832:287–328.

Rastan, M., Sohankar, A., and Alam, M. M. (2017). Low-reynolds-number flow around a wall-mounted square cylinder: Flow structures and onset of vortex shedding. *Physics of Fluids*, 29(10).

Rostamy, N., Sumner, D., Bergstrom, D. J., and Bugg, J. D. (2013). Instantaneous flow field above the free end of finite-height cylinders and prisms. *International Journal of Heat and Fluid Flow*, 43:120–128.

Saeedi, M., LePoudre, P. P., and Wang, B.-C. (2014). Direct numerical simulation of turbulent wake behind a surface-mounted square cylinder. *Journal of Fluids and Structures*, 51:20–39.

Saeedi, M. and Wang, B.-C. (2016). Large-eddy simulation of turbulent flow around a finite-height wall-mounted square cylinder within a thin boundary layer. *Flow, Turbulence and Combustion*, 97(2):513–538.

Saha, A. K. (2004). Three-dimensional numerical simulations of the transition of flow past a cube. *Physics of Fluids*, 16(5):1630–1646.

Saha, A. K. (2013). Unsteady flow past a finite square cylinder mounted on a wall at low reynolds number. *Computers & Fluids*, 88:599–615.

Saha, A. K., Muralidhar, K., and Biswas, G. (2000). Vortex structures and kinetic energy budget in two-dimensional flow past a square cylinder. *Computers & fluids*, 29(6):669–694.

Sakamoto, H. (1985). Aerodynamic forces acting on a rectangular prism placed vertically in a turbulent boundary layer. *Journal of wind engineering and industrial aerodynamics*, 18(2):131–151.

Sakamoto, H. and Arie, M. (1983). Vortex shedding from a rectangular prism and a circular cylinder placed vertically in a turbulent boundary layer. *Journal of Fluid Mechanics*, 126:147–165.

Sarode, R., Gai, S., and Ramesh, C. (1981). Flow around circular-and square-section models of finite height in a turbulent shear flow. *Journal of Wind Engineering and Industrial Aerodynamics*, 8(3):223–230.

Sattari, P., Bourgeois, J., and Martinuzzi, R. (2012). On the vortex dynamics in the wake of a finite surface-mounted square cylinder. *Experiments in fluids*, 52(5):1149–1167.

Schewe, G. (2013). Reynolds-number-effects in flow around a rectangular cylinder with aspect ratio 1: 5. *Journal of Fluids and Structures*, 39:15–26.

Shah, K. B. and Ferziger, J. H. (1997). A fluid mechanicians view of wind engineering: Large eddy simulation of flow past a cubic obstacle. *Journal of wind engineering and industrial aerodynamics*, 67:211–224.

Sohankar, A. (2006). Flow over a bluff body from moderate to high reynolds numbers using large eddy simulation. *Computers & Fluids*, 35(10):1154–1168.

Sumner, D. (2013). Flow above the free end of a surface-mounted finite-height circular cylinder: a review. *Journal of Fluids and Structures*, 43:41–63.

Sumner, D., Heseltine, J., and Dansereau, O. (2004). Wake structure of a finite circular cylinder of small aspect ratio. *Experiments in Fluids*, 37(5):720–730.

Sumner, D., Rostamy, N., Bergstrom, D., and Bugg, J. (2017). Influence of aspect ratio on the mean flow field of a surface-mounted finite-height square prism. *International Journal of Heat and Fluid Flow*, 65:1–20.

Taneda, S. (1952). An experimental study on the structure of the vortex street behind a circular cylinder of finite length. In *Research Report of Institute of Applied Mechanics*, volume 1, pages 131–142. Kyu-Shu University.

Telgarsky, R. (2013). Dominant frequency extraction. *arXiv*.

Tobak, M. and Peake, D. J. (1982). Topology of three-dimensional separated flows. *Annual review of fluid mechanics*, 14(1):61–85.

Uffinger, T., Ali, I., and Becker, S. (2013). Experimental and numerical investigations of the flow around three different wall-mounted cylinder geometries of finite length. *Journal of wind engineering and industrial aerodynamics*, 119:13–27.

Unnikrishnan, S., Ogunremi, A., and Sumner, D. (2017). The effect of incidence angle on the mean wake of surface-mounted finite-height square prisms. *International Journal of Heat and Fluid Flow*, 66:137–156.

Versteeg, H. K. and Malalasekera, W. (2007). *An Introduction to Computational Fluid Dynamics: The Finite Volume Method*. Pearson Education Limited.

von Kàrmàn, T. (1910). Untersuchungen über knickfestigkeit, mitteilungen über forschungsarbeiten. *Ver. Deut. Ing. Forschungsh.*, 81.

Wang, H. and Zhou, Y. (2009). The finite-length square cylinder near wake. *Journal of Fluid Mechanics*, 638:453–490.

Wang, H., Zhou, Y., Chan, C., and Lam, K. (2006). Effect of initial conditions on interaction between a boundary layer and a wall-mounted finite-length-cylinder wake. *Physics of Fluids*, 18(6).

Wang, H., Zhou, Y., Chan, C., Wong, W., and Lam, K. (2004). Flow structure around a finite-length square prism. In *15 th Australasian Fluid Mechanics Conference*, pages 13–17.

Wei, Q.-D., Chen, G., and Du, X.-D. (2001). An experimental study on the structure of juncture flows. *Journal of visualization*, 3(4):341–348.

White, F. M. (1999). *Fluid mechanics*. McGraw-hill.

White, F. M. and Corfield, I. (1991). *Viscous fluid flow*, volume 2, pages 5–300. McGraw-Hill New York.

Yakhot, A., Liu, H., and Nikitin, N. (2006). Turbulent flow around a wall-mounted cube: A direct numerical simulation. *International journal of heat and fluid flow*, 27(6):994–1009.

Yu, D., Butler, K., Kareem, A., Glimm, J., and Sun, J. (2012). Simulation of the influence of aspect ratio on the aerodynamics of rectangular prisms. *Journal of Engineering Mechanics*, 139(4):429–438.

Zdravkovich, M. M. (1997). *Flow around circular cylinders: Volume 1: Fundamentals*, volume 1. Oxford university press.

Zeiger, M., Telionis, D., and Vlachos, P. (2004). Unsteady separated flows over three-dimensional slender bodies. *Progress in Aerospace Sciences*, 40(4-5):291–320.

Zhang, D., Cheng, L., An, H., and Zhao, M. (2017). Direct numerical simulation of flow around a surface-mounted finite square cylinder at low reynolds numbers. *Physics of Fluids*, 29(4).

Zhang, S., Cagney, N., Balabani, S., Naveira-Cotta, C. P., and Tiwari, M. K. (2019). Probing vortex-shedding at high frequencies in flows past confined microfluidic cylinders using high-speed microscale particle image velocimetry. *Physics of Fluids*, 31.